Development and Demonstration of Coal combustion Byproducts-Filled Composite Materials for Utility Pole Fabrication

Final Report

By

Yoginder P. Chugh, Jinrong Ma

Mining and Mineral Resources Engineering

Southern Illinois University

Carbondale, Illinois 62901

For

Combustion Byproducts Recycling Consortium

West Virginia University

Morgantown, WV

March 2006

ACKNOWLEDGEMENTS

The authors sincerely acknowledge the support of the following organizations and individuals for their support in completing this research and preparation of this report.

- Combustion Byproducts Recycling Consortium of the U.S. Department of Energy and Illinois Clean Coal Institute for their financial support.
- Ashland Chemicals, Inc of Columbus, Ohio and Trinity Industries, Inc of Paducah, KY for their technical support and untiring enthusiasm and efforts to commercialize the project.
- Utility companies in the Midwest that provided significant input into the development of the utility pole and into marketing strategies.
- Ms. Anagha Patwardhan, Ms. Safiya McNeese-Hill, and Mr. Samrat Mohanty for their assistance in report preparation.

Table of Contents

ACKNOWLEDGEMENTS…….ii

TABLE OF CONTENTS ……...iii

LIST OF FIGURES …….. vii

LIST OF TABLES ……..xi

CHAPTER 1: BACKGROUND AND PROBLEM STATEMENT 1

1.1 Background 1

1.2 Motivation for the study..... 2

1.3 Overall apporoach..... 3

1.4 Research Objectives…….5

1.5 Report organization..... 6

CHAPTER 2: REVIEW OF PERTINENT LTERATURE..... 8

2.1 Fly ash characteristics …….8

2.2 CCBs as filler in composite materials..... 9

2.3 Micro-mechanical analysis of FRC 10

2.4 Failure criteria for FRC materials 10

2.5 Summary..... 12

CHAPTER 3: DESIGN CONCEPTS FOR CCBS-FILLED FRC POLE..... 13

3.1 Introduction..... 13

3.2 Design requirments for CCBs-filled composite utility pole 13

3.3 Laborotary testing of class-4 wooden poles..... 13

3.4 Design considerations and proposed basic design..... 15

3.5 Theoretical analysis 16

3.6 Dimensional analysis 20

3.7 Utility pole design using finite element method 23

CHAPTER 4: DEVELOPMENT OF CCBS-FILLED POLYMERIC COMPOSITE MATERIAL ……..32

4.1 Introduction..... 32

4.2 Component material characterization 32

4.3 Preliminary outer-shell material development 35

4.4 Outer-shell material development using statistical experimental design..... 37

4.5 Effect of type of the fly ash..... 52

CHAPTER 5: DESIGN, MANUFACTURE, AND OPTIMIZATION OF THE COMPOSITE POLE……...59

5.1 Introduction..... 59

5.2 Structural analysis 59

5.3 Candidate designs when the pole is unfilled 59

5.4 Manufacturing of the CCBs-filled FRC model utility pole 63

5.5 Optimization of the composite pole design 64

CHAPTER 6: MICRO-MECHANICS ANALYSES 73

6.1. Introduction..... 73

6.2 Determination of fiber volume fraction through the ASTM burnout test..... 73

6.3 Micro-mechanics analysis of the lamina..... 75

6.4. Summary..... 83

CHAPTER 7: MACRO-MECHANICS ANALYSIS..... 84

7.1 Introduction..... 84

7.2 Lamina mechanics..... 84

7.3 Lamina stiffness matrix in global coordinate system..... 87

7.4 Macro-mechanics of a CCBs-filled FR laminate..... 89

7.5. Predicted engineering properties of the CCBs-filled laminate..... 97

7.6. Summary..... 98

CHAPTER 8: ENGINEERING PROPERTIES CHARACTERIZATION..... 99

8.1 Introduction..... 99

8.2 Tensile engineering properties..... 99

8.3. Axial and off-axis compressive stiffness and strength..... 109

8.4. Flexural bending test..... 116

8.5. Water absorption and UV resistance..... 118

CHAPTER 9: FAILURE ANALYSIS..... 120

9.1. Introduction..... 120

9.2. Failure criteria..... 120

9.3. Summary..... 131

CHAPTER 10: PERFORMANCE TESTING OF THE MODEL POLEs..... 132

10.1. Introduction..... 132

10.2. Cantilever bending test of the model composite pole..... 132

10.3. Uniaxial compression test on 12-inch long model pole..... 138

CHAPTER 11: INDUSTRIAL COOPERATION AND ECONOMIC EVALUATION……..140

11.1. Introduction…….……....140

11.2. Economic Evaluation……140

CHAPTER 12: SUMMARY AND CONCLUSIONS 141

12.1. Summary..... 141

12.2. Conclusion..... 142

12.3. Recommendations for future work 143

REFERENCES..... 144

List of Figures

FIGURE 1.1 A TYPICAL WOODEN CLASS-4 (35 FT) UTILITY POLE 1

FIGURE 1.2- A SCHEMATIC DIAGRAM OF A UTILITY POLE 3

FIGURE 1.3 - SCHEMATIC DIAGRAMS OF ENGINEERED COMPOSITE UTILITY POLE DESIGNS 4

FIGURE 1.4 - OVERALL FLOWCHART FOR THE DEVELOPMENT OF CCBS-FILLED UTILITY POLES 6

FIGURE 2.1 - F ASH AND FBC ASH SAMPLE MAGNIFIED BY FACTOR OF 500 8

FIGURE 2.2 - TYPICAL PARTICLE SIZE DISTRIBUTION CURVE, FOR SOME CCBS (CHUGH, 2002) 9

FIGURE 3.1- A 300,000 LB CAPACITY COMPRESSIVE STRENGTH TESTING FACILITY 14

FIGURE 3.2 - SCHEMATIC PLOT OF THE THREE-POINT BENDING TEST APPARATUS 14

FIGURE 3.4 - LOADING CONDITIONS FOR A CLASS-4 COMPOSITE POLE 16

FIGURE 3.5 - BENDING MOMENT AND SHEAR FORCE DIAGRAM FOR A UTILITY POLE 17

FIGURE 3.6 - FREE BODY DIAGRAM FOR A POLE SUBJECTED TO TWISTING MOMENT ONLY 20

FIGURE 3.7 - FEM MODELS OF CONICAL AND CYLINDRICAL POLE MODELS 24

FIGURE 3.8 - DEFLECTION OF AN ENGINEERED COMPOSITE UTILITY POLE 25

FIGURE 3.9 - STRESS DISTRIBUTION IN A POLE (PLAN VIEW AT BOTTOM) 26

FIGURE 3.10 - STRESS DISTRIBUTION AT THE BOTTOM PORTION OF THE POLE (AXIAL CUT VIEW) 26

FIGURE 3.11 - DETAILED VIEW OF AREA A IN FIGURE 3.10 27

FIGURE 3.12 - COMPARISON OF TOP DEFLECTION FOR COMPOSITE POLE AND WOODEN POLE 29

FIGURE 3.13 - TORSIONAL DEFORMATION OF THE HOLLOW AND FILLED COMPOSITE POLE (X 10) 29

FIGURE 3.14 - TORSIONAL DEFORMATION OF A WOODEN POLE (X10) 30

FIGURE 3.15 - COMPARISON OF THE TORSIONAL DEFORMATION FOR FILLED AND UNFILLED COMPOSITE POLE AND WOOD POLE 31

FIGURE 3.16 - STRESS DISTRIBUTION AND TORSIONAL DEFORMATION OF WOOD POLE (TOP VIEW) 32

FIGURE 4.3 - PARTICLE SIZE DISTRIBUTION CURVE FOR FBC FLY ASH 33

FIGURE 4.9 - COMPRESSIVE STRENGTH VS. FLY ASH % AT DIFFERENT CURING TEMPERATURES 37

FIGURE 4.10 - TANGENT ELASTIC MODULUS VS. FLY ASH % AT DIFFERENT CURING TEMPERATURES 37

FIGURE 4.11 - TANGENT ELASTIC MODULUS VS. FLY ASH PERCENTAGE AND POST-CURING TEMPERATURE 43

FIGURE 4.12 - ET VS. FLY ASH PERCENTAGE AND POST-CURING TEMPERATURE AFTER 16 HR POST-CURING 43

FIGURE 4.13 - ET VS. FLY ASH PERCENTAGE AND POST-CURING TEMPERATURE AFTER 24 HR POST-CURING..44
FIGURE 4.14 - PREPARED ASTM SAMPLES FOR COMPRESSION TEST.....45
FIGURE 4.15 - TANGENT ELASTIC MODULUS VS. FLY ASH LOADING LEVEL.....51
FIGURE 4.16 - GEL TIME OF THE FLY ASH-RESIN MIXTURE VS. FLY ASH LOADING LEVEL.....51
FIGURE 4.17 - VISCOSITY OF THE FLY ASH-RESIN MIXTURE VS. FLY ASH LOADING LEVEL.....52
FIGURE 4.18 - C FLY ASH SAMPLE (X 1,000).....52
FIGURE 4.19 - FBC FLY ASH SAMPLE (X 1,000).....53
FIGURE 4.20 - ELASTIC MODULUS VS. FLY ASH % FOR FBC-FLY-ASH-BASED COMPOSITE MATERIAL.....55
FIGURE 4.21 - FAILURE STRENGTH VS. FLY ASH % FOR FBC-FLY-ASH-BASED COMPOSITE MATERIAL.....56
FIGURE 4.22 - ELASTIC MODULUS VS. FLY ASH % FOR C-FLY-ASH-BASED COMPOSITE MATERIAL.....56
FIGURE 4.23 - FAILURE STRENGTH VS. FLY ASH % FOR C-FLY-ASH-BASED COMPOSITE MATERIAL.....57
FIGURE 5.1 - COMPARISON OF WOODEN POLE AND HOLLOW POLE WHEN EOUT =3.5 MILLION PSI.....60
FIGURE 5.2 - COMPARISON OF WOODEN POLE AND HOLLOW POLE WHEN EOUT =3 MILLION PSI.....60
FIGURE 5.3 - COMPARISON OF WOODEN POLE AND HOLLOW POLE WHEN EOUT = 2.5 MILLION PSI.....61
FIGURE 5.4 - PULTRUSION PROCESS.....61
FIGURE 5.5 - PULTRUSION OF THE MODEL COMPOSITE UTILITY POLE.....64
FIGURE 5.6 - PULTRUDED CCBS-FILLED FRC UTILITY MODEL POLES.....64
FIGURE 5.7 - CLOSE VIEW OF THE MODEL POLE AND MAGNIFIED CROSS-SECTION.....64
FIGURE 5.8 - ROVING AND CSM LAYERS IN A FAILED TENSION SPECIMEN.....65
FIGURE 5.9 - POLISHED CROSS-SECTION THROUGHOUT THE THICKNESS OF THE COMPOSITE MATERIAL.....65
FIGURE 5.10 - IDEALIZED LAY-UP SYSTEM FOR PULTRUDED COMPOSITE OUTER-SHELL.....66
FIGURE 6.1 - BURNOUT TEST SAMPLES.....74
FIGURE 6.2 - POLISHED CROSS-SECTION OF THE CCBS-FILLED COMPOSITE.....74
FIGURE 6.3 - MATERIAL ARCHITECTURE OF CCBS-BASED FRP COMPOSITE.....76
FIGURE 6.4 - SCHEMATIC ILLUSTRATION OF MATERIAL ARCHITECTURE OF ROVING LAYER.....77
FIGURE 6.5 - SCHEMATIC ILLUSTRATION OF MATERIAL ARCHITECTURE OF CSM LAYER.....81
FIGURE 7.1 - GLOBAL AND MATERIAL COORDINATE SYSTEM.....84
FIGURE 7.2 - A PLATE ELEMENT IN CCBS-FILLED CYLINDRICAL COMPOSITE UTILITY POLE.....89
FIGURE 7.3 - FORCES AND MOMENTS RESULTANTS ON A LAMINATED PLATE ELEMENT.....90

FIGURE 7.4 - GEOMETRY OF A DEFORMED LAMINATE 91
FIGURE 7.5 - LAMINA NUMBERING SYSTEM 92
FIGURE 8.1 - ALUMINUM CALIBRATION SPECIMENS 100
FIGURE 8.2 - DIMENSIONS OF THE ASTM TENSILE TEST SPECIMEN 100
FIGURE 8.3 - PREPARED TENSION TEST SPECIMENS OF CCBS-BASED COMPOSITE 100
FIGURE 8.4 - TYPICAL STRESS-STRAIN CURVE OF A CCBS-BASED TENSILE SAMPLE 103
FIGURE 8.5 - TENSILE STRESS-STRAIN CURVES FOR ALL OFF-AXIS ANGLES 104
FIGURE 8.6 - VARIATION OF AVERAGE ELASTIC MODULUS WITH OFF-AXIS ANGLE 107
FIGURE 8.7 - VARIATION OF AVERAGE YIELD STRESS AND ULTIMATE TENSILE STRESS VS. OFF-AXIS ANGLE 107
FIGURE 8.8 - VARIATION OF AVERAGE YIELD STRAIN AND ULTIMATE STRAIN OF TENSION TESTS WITH OFF-AXIS ANGLE 108
FIGURE 8.9 - COMPARISON OF MEASURED AND PREDICTED E VALUES FOR DIFFERENT ROVING FIBER ORIENTATION 109
FIGURE 8.13 - COMPRESSION TEST SPECIMEN 110
FIGURE 8.14 - PREPARED COMPRESSION TEST SPECIMEN OF CCBS-BASED COMPOSITE 110
FIGURE 8.15 - TEST SAMPLE SUPPORT JIG 110
FIGURE 8.17 - VARIATION OF ELASTIC MODULUS WITH ROVING FIBER ORIENTATION 111
FIGURE 8.18 - VARIATION OF FAILURE STRENGTH WITH ROVING FIBER ORIENTATION 115
FIGURE 8.19 - VARIATION OF FAILURE STRAIN WITH ROVING FIBER ORIENTATION 116
FIGURE 8.20 - FOUR-POINT FLEXURAL BENDING TEST OF COMPOSITE PANEL 116
FIGURE 9.1 - THE MAXIMUM STRESS CRITERION IN S_2 - S_6 STRESS SPACE 121
FIGURE 9.2 – FAILURE ENVELOPES IN STRAIN SPACE $?_1$-$?_2$ 122
FIGURE 9.3 - FPF AND FF LOAD IN PLY-BY-PLY FAILURE ANALYSIS (BARBERO, 1999) 127
FIGURE 10.1 - THE STEEL FRAME USED TO CLAMP THE MODEL POLE 133
FIGURE 10.2 - LOADING DEVICE AND DEFLECTION MEASURING SETUP 133
FIGURE 10.3 - CANTILEVER BENDING TEST OF 20-FT LONG MODEL COMPOSITE UTILITY POLE 134
FIGURE 10.4 - CANTILEVER BENDING TEST AFTER MATERIAL FAILURE 134
FIGURE 10.5 - LOAD VS. DEFLECTION AT THE TOP OF THE MODEL POLE 136
FIGURE 10.6 - ESTIMATION OF EQUIVALENT E OF COMPOSITE MODEL POLE 136

FIGURE 10.7 - VARIATION OF EQUIVALENT ELASTIC MODULUS WITH TOP DEFLECTION OF THE MODEL POLE **136**

FIGURE 10.8 - COMPARISON OF THEORETICAL AND EXPERIMENTAL BENDING CURVATURE **137**

FIGURE 10.9 - STRESS-STRAIN CURVE FOR 12-INCH LONG MODEL POLE IN UNIAXIAL COMPRESSION..... **138**

FIGURE 10.9 - MODEL COMPOSITE POLES INSTALLED OUTDOOR AT ILLINOIS COAL DEVELOPMENT PARK (FALL 2002) **139**

Figure 10.10 : Poles on March 10, 2006 (after weathering fro 42 months) **139**

List of Tables

TABLE 2.1 - OXIDES COMPOSITION OF FLY ASH 8

TABLE 3.1 - THREE-POINT BENDING TEST DATA FOR A CYLINDRICAL WOOD POLE 15

TABLE 3.2 - SUMMARY OF THREE-POINT BENDING TEST RESULTS 15

TABLE 3.3 - COMPARISON OF DEFLECTION RESULTS FROM FEM AND ANALYTICAL APPROACHES 19

TABLE 3.4 - RESULTS OF DIMENSIONAL ANALYSIS FOR A HOLLOW CYLINDRICAL COMPOSITE POLE 23

TABLE 3.5 - DIMENSIONS OF THE COMPOSITE UTILITY POLE MODEL 24

TABLE 3.6 - MATERIAL PROPERTIES FOR UTILITY POLE DESIGN 24

TABLE 3.7 - FEM MODELS AND RESULTS FOR COMPOSITE UTILITY POLE 25

TABLE 3.8 - ADDITIONAL FEM RESULTS FOR A COMPOSITE UTILITY POLE 28

TABLE 4.1 - OXIDES COMPOSITION OF THE SIU FBC FLY ASH 32

TABLE 4.2 - SIZE ANALYSIS RELATED PARAMETERS FOR FBC FLY ASH 33

TABLE 4.3 - COMPRESSIVE TEST RESULTS FOR INNER-CORE MATERIAL (FULL DENSITY) 36

TABLE 4.4 - FACTORS AND RESPONSES CONSIDERED IN THE DESIGN 38

TABLE 4.5 - DESIGN MATRIX 39

TABLE 4.6 - ENGINEERING PROPERTIES OF VARIOUS MIXES 40

TABLE 4.7 - ANOVA TABLE OF COMPRESSIVE STRENGTH OF OUTER-SHELL MATERIAL 41

TABLE 4.8 - ANOVA TABLE FOR ELASTIC MODULUS OF THE OUTER-SHELL MATERIAL 42

TABLE 4.9 - COMPRESSION TEST RESULTS FOR -75 MICRONS CCBS-BASED COMPOSITE MATERIAL 46

TABLE 4.10 - COMPRESSION TEST RESULTS FOR -53 MICRONS CCBS-BASED COMPOSITE MATERIAL 47

TABLE 4.11 - COMPRESSION TEST RESULTS FOR -38 MICRONS CCBS-BASED COMPOSITE MATERIAL 48

TABLE 4.12 - COMPRESSION TEST RESULTS FOR AS-RECEIVED CCBS-BASED COMPOSITE MATERIAL 49

TABLE 4.13 - EFFECT OF FLY ASH PARTICLE SIZE AND LOADING LEVEL ON OUTER-SHELL PROPERTIES 50

TABLE 4.14 - UNCONFINED COMPRESSION TEST RESULTS FBC-BASED COMPOSITE MATERIAL 50

TABLE 4.15 - UNCONFINED COMPRESSION TEST RESULTS OF C FLY ASH COMPOSITE MATERIAL 54

TABLE 5.2 - CANDIDATE DESIGN OF THE HOLLOW CLASS-4 COMPOSITE UTILITY POLE 55

TABLE 5.3 - VARIATION OF OBJECTIVE FUNCTION VALUES WITH THE OUTER DIAMETER 61

TABLE 5.4 - PROMISING DESIGNS FOR THE HOLLOW COMPOSITE UTILITY POLE 71

TABLE 6.1 - FVF OF CCBS-BASED COMPOSITE VIA BURNOUT TEST RESULTS 75

TABLE 6.2 - PROPERTIES OF FIBER AND MATRIX 76

TABLE 6.3 - PREDICTED ENGINEERING PROPERTIES OF ROVING LAMINA 81

TABLE 6.4 - PREDICTED ENGINEERING PROPERTIES OF CSM LAMINA 83

TABLE 7.1 - DEFINITION OF CONTRACTED NOTATION 85

TABLE 7.2 - STACKING SEQUENCE AND THICKNESS OF EACH LAYER 97

TABLE 7.3 - APPARENT ENGINEERING PROPERTIES OF THE LAMINATE 98

TABLE 8.1(A) - TENSILE TEST RESULTS FOR LENGTHWISE SAMPLES 101

TABLE 8.1(B) - TENSILE TEST RESULTS FOR CROSSWISE SAMPLES 102

TABLE 8.2 - OFF-AXIS TENSILE TEST RESULTS 105

TABLE 8.3 - MEAN VALUE AND STANDARD DEVIATION OF OFF-AXIS TENSILE TESTS 106

TABLE 8.4 - COMPARISON OF MEASURED E AND PREDICTED E VALUES. 109

TABLE 8.5 - OFF-AXIS COMPRESSION TEST RESULTS FOR 5%-FLY-ASH SAMPLES 112

TABLE 8.6 - OFF-AXIS COMPRESSION TEST RESULTS FOR 10% FLY ASH SAMPLES 113

TABLE 8.7 - MEAN AND STANDARD DEVIATION VALUES FOR THE OFF-AXIS COMPRESSION TEST RESULTS .. 115

TABLE 8.8 - FOUR-POINT BENDING TEST RESULTS OF PULTRUDED COMPOSITE PANEL 117

TABLE 8.9 - WATER ABSORPTION TEST RESULTS 118

TABLE 8.10 - IRRADIANCE RANGES OF UV RESISTANCE TEST 119

TABLE 9.1 - MEASURED STRENGTH RESULTS FOR CCBS-FILLED FRC LAMINATE 131

TABLE 10.1 - TEST RESULT OF CANTILEVER BENDING TEST ON COMPOSITE MODEL POLE 135

CHAPTER 1: BACKGROUND AND PROBLEM STATEMENT

1.1 Background

The utility industries currently utilize wooden poles (Figure 1.1) for installation of cables, lights, telephone, and transmission lines. It is estimated that over one million poles are utilized annually in the Midwestern region in the US varying in height from 15 feet to 40 feet. A wooden pole is relatively lightweight, easily trimmed to desired length, and easy to work with. However, as a naturally occurring material, its engineering characteristics are anisotropic and subject to wide variation. Wood is much stronger when loaded axially (along the grain) than when loaded transversely (perpendicular to the grain). Soft spots, knots, and voids within the wood cause the wooden structure to be weaker than anticipated. Yu (1987) indicated that the strength of a wood typically drops about 50% due to a two-inch knot. A section of wood may appear to be free of defects to the naked eye, but may include one, or all, of the aforementioned defects.

Wood generally absorbs moisture, which decreases its engineering properties and causes decay over time. As the moisture content of the wood increases, the strength of the wood generally decreases. Biron and Arioglu (1983) identified that the moisture content of wood is a major limiting factor in the strength of wood products. For pine, crushing strength decreases by 82% as the moisture content increases to 50%.

Figure 1.1 - A typical wooden class-4 (35 ft) utility pole

To alleviate the wood decay problems, chemical pre-treatment of a wooden pole is a common practice. In addition to expense (usually $35 per pole every 5-years), effects of the chemical and preservatives on environment is also of concern. The chemicals usually do not remain within poles and ooze to the surface, evaporate and may move into the soil and/or water under and around poles, which may create localized environmental issues. Therefore, the disposal of wooden poles is also a major environmental concern.

The above disadvantages of wooden poles concerns have prompted the investigation for alternative engineered poles, which should be of higher strength, lightweight, chemically inert, safe to environment, and should require less costly post-

installation maintenance. Metal (such as steel, aluminum, or alloy) utility poles first came into the picture due to their known engineering properties. However, they are expensive and also suffer from corrosion problems, again reducing service life and increasing life cycle cost with required maintenance. Concrete utility poles have also been used. But neither metal nor concrete utility poles have gained popularity because they are usually heavy and their installation in remote areas requires large capacity equipment and special access roads to be constructed, that are expensive. In the last decade, polymer-based reinforced poles have been developed that are entering the market. This project was undertaken to design and develop coal combustion byproducts CCBs-filled fiberglass reinforced polymeric composite materials (green material) for utility poles including transmission poles as the replacement for current wooden poles.

1.2 Motivation for the study

During recent decades, FRC utility poles have received interest and have been made possible by development of composites technology. Advances in polymer chemistry have led to development of specific resins that are not susceptible to ultraviolet radiation degradation. More importantly, production cost has been reduced with the development of high-speed manufacturing processes and the stabilization of raw material prices. These developments have opened the possibilities of developing engineered FRC utility poles that are competitive with other poles in the market place. Compared with a conventional wooden, concrete, or metal poles, a FRC utility pole should possesses the following major advantages.

1. Meet specific engineering applications, including color.
2. Should have no negative environmental impacts.
3. Should be light-weight. Typically, a 40 ft class-4 wooden pole weighs about 1,100 lb, whereas a similar FRC utility pole would weigh only about 200 – 400 lbs.
4. Lower installation cost. This is especially advantageous for pole installation in remote locations, where transporting the poles with helicopter may be the only practical choice.
5. Should not decay over time due to very low moisture absorption.
6. Should resist pests, woodpeckers, and chemical corrosion and therefore its service life should be longer than a wooden pole.

Adding mineral fillers into a polymer based composite is a common practice in the composite materials industries due to the benefits that filler brings such as reduced cost and improved properties of the manufactured parts. CCBs are the inorganic residues that remain after pulverized coal is burned at a power plant. CCBs can be classified as a mineral based on their chemistry and physical properties (Wypych, 1999). The characteristics of CCBs are very close to a number of commercial fillers, such as small particle size, vast and widely distributed supplies, low cost, etc. Previous studies (Plowman, 1984; Jablonshi, 1987; Huang, 1995) have indicted that the use of fly ash as a polymer filler has promise with the following three major benefits.

1. Lower material cost. The matrix material, resin or polymer, is generally expensive ($1- $3/lb) and constitutes the major part of the cost of final composite products. In comparison with common mineral fillers such as calcium carbonate, CCBs is

a very cheap filler mineral source because it is a low value byproduct with small particle size and uniform particle size distribution ranging from 10 to 40 microns.

2. Improved processing behavior and physical and engineering properties of the products. Addition of fly ash into a polymer composite typically increases the strength and stiffness, and impact resistance of the finished products (Plowman, 1984; Jablonshi, 1987; Huang, 1995). Their studies show that it also increases surface hardness and reduces shrinkage of the products.

3. Utilization of CCBs as a mineral filler can be an ideal way to use the low value byproduct material in an economically beneficial and environmentally sound manner.

This research was focused on the development and demonstration of the CCBs-filled FRC material for utility poles. Successful development and commercialization of the CCBs-filled FRC utility poles should increase current utilization of CCBs in the US by about 10% with additional benefits described above.

1.3 Overall apporoach

The class-4 wooden utility pole specified by ANSI O5.1 – 1992 (Specifications and Dimensions for Wood Poles) was utilized as the design baseline for the composite utility pole. The standard specified (Figure 1.2) the length, minimum circumferences at the top of the pole, 6 ft above the butt, and the distance from the butt to the ground line, as shown in Figure 1.2. The pole must sustain 2,400 lb lateral load applied 2 ft from the top without failure.

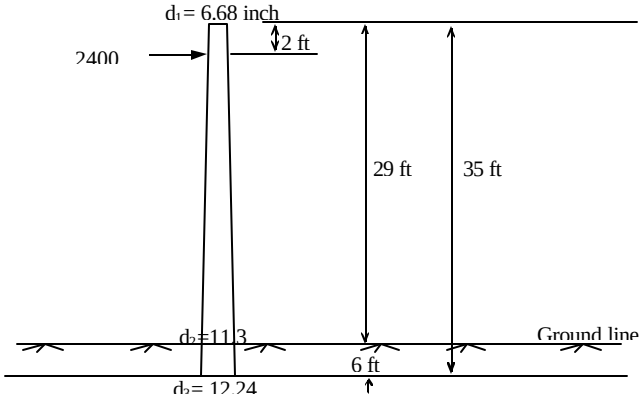

Figure 1.2- A schematic diagram of a utility pole

The proposed composite pole (Figure 1.3) may be either of conical or cylindrical shape, and consist of a very stiff outer-shell with or without ultra-lightweight inner-core material. Initially, filling the pole with an ultra-lightweight CCBs- based material was considered but the cost and weight considerations eliminated that approach. Material characterization was developed for the outer-shell material (using 5% ~ 25% CCBs and polymer material (using 40% to 60% CCBs and polymer) for the inner-core materials. Studies revealed that adding 5% to 20% fly ash into the un-reinforced outer-shell composite had positive effects on the material stiffness. This research had two main

tasks: 1) Development and characterization of the CCBs-filled FRC material, and 2) Structural design and analysis of the class-4 utility pole with the developed CCBs-filled composite material.

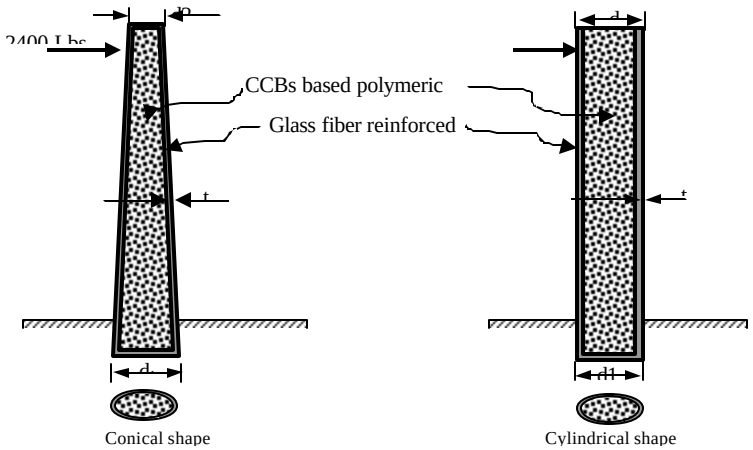

Figure 1.3 - Schematic diagrams of engineered composite utility pole designs

Material development and characterization:

Development and structural design of a utility pole with the CCBs-filled FRC materials are more complex than with conventional materials such as wood and steel. This is mainly because the FRC materials are complex, non-homogeneous, and anisotropic. They do not exhibit the same material structure throughout the bulk and are anisotropic. Their variability results from a wide variation of constituent materials added and from the uncontrollable factors involved in the fabrication process such as fiber misalignment, poor mixture of filler and resin, temperature change, etc. All these problems require that careful material characterization, in-depth calculations, and analysis be conducted to account for the varying material properties and the direction of loading. Scientific understanding of FRC materials is still sketchy and lack general applicability.

In this study, efforts were made to characterize the engineering properties of the developed composite material using experimental as well as micro/macro-mechanics approaches. Based on the laboratory test results and theoretical analyses, the failure modes of the composite were analyzed and an applicable failure criterion was identified.

Structural design of the CCBs-filled FRC utility pole:

There are four major problems that need to be considered when designing a composite utility pole.

Top deflection: A utility pole is basically a cantilever beam and its primary function is to maintain structural stability by resisting bending and torsional moments caused by unbalanced horizontal load, wind load, etc. Other scenarios, such as wind load and build up of snow on electricity lines, can also significantly amplify forces acting on the structure and must be accounted for at the design stage.

Compression and tension: In addition to its weight, a FRC utility pole is also subjected to compressive loads caused by structural attachments such as cross-arm, ladders, transformers and support guys. Due to the bending effect caused by the pulling force of transmission lines, wind load, etc, one side of the outer-shell at the pole bottom is subjected to high compressive stress whereas the opposite side is subjected to high tensile stress. The localized buckling failure near the pole bottom due to the compression effect needs to be evaluated in the pole design.

Torsion: Horizontal pulling force exerted at both ends of a cross-arm by transmission lines may be unbalanced, and consequently a torque may be generated at the top and the bottom of the utility pole. Investigating the effect of the twisting moment on pole failure and stability also needs to be considered in pole design.

Fatigue and UV damage: Wind poses a significant fatigue load with varying frequency to poles and masts which should be considered. Fortunately, fatigue performance is an area where composites have been shown to far outperform steel components. Manufacturers like Shakespeare (Shakespeare, 2003) claim that they have not been able to induce any type of fatigue failure in a fiberglass laminate. Due to this fact, material fatigue was not considered in this study.

UV damage, whereby a structure surface is eroded, exposing the reinforcement fibers ("bloom"), is a common concern for FRC products. This phenomenon is dependent on the ultraviolet energy levels in the atmosphere and can be apparent after as little as three year service in the field.

1.4 Research objectives

Based on the problems discussed above, the specific objectives of this research were established as below:

- Develop the concepts of a CCBs-filled FRC utility pole.
- Characterize component materials (CCBs, resin, fiberglass).
- Develop and characterize un-reinforced CCBs-filled polymeric materials.
- Evaluate the effect of loading level and particle size of CCBs on engineering properties of un-reinforced composite material.
- Fabricate the CCBs-filled FRC utility pole.
- Characterize engineering properties (tension, compression, and shear) of the pultruded FRC materials.
- Perform micro/macro-mechanical analysis on the developed composite material.

- Design, analyze, and optimize a composite pole design following ANSI O.1 specifications.
- Identify and develop suitable failure criteria for CCBs-filled FRC material.
- Analyze and evaluate the deformation and stress distribution within the composite pole under appropriate loading conditions using finite element method.
- Test and demonstrate performance of developed composite model poles in the laboratory and in the field.

The overall research flow chart for the development and demonstration of CCBs-filled FRC utility pole is shown in Figure 1.4.

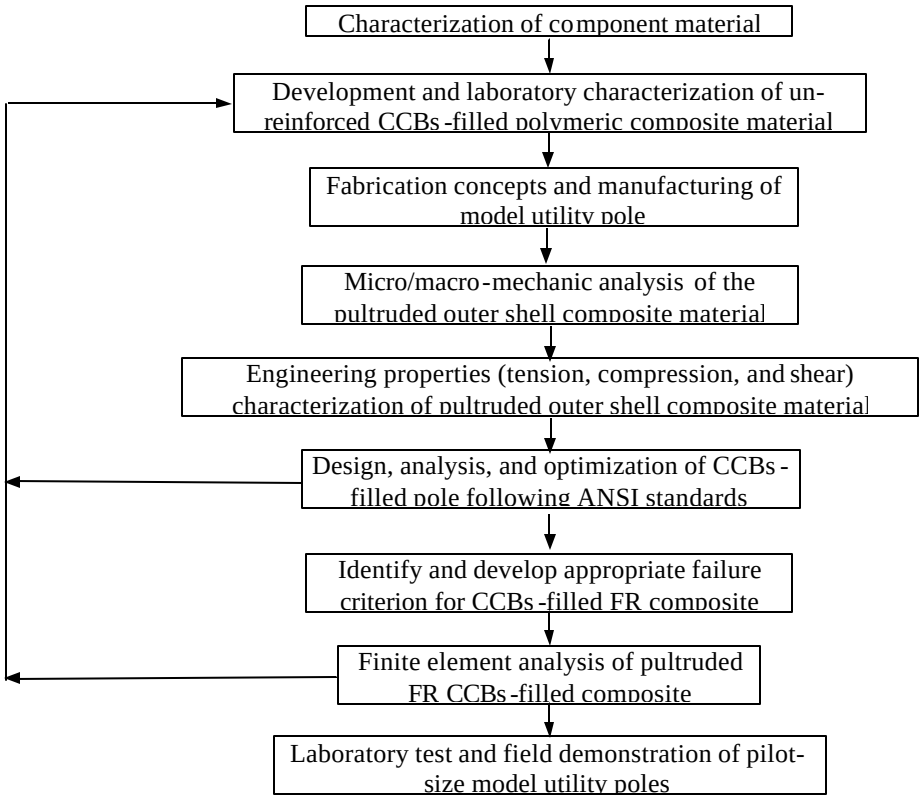

Figure 1.4 - Overall flowchart for the development of CCBs-filled utility poles

1.5 Report organization

The main purpose of this chapter is to provide information for proposed research objectives of this study. Chapter II reviews pertinent literature and the design concepts for a CCBs-filled fiberglass reinforced composite utility pole are described in Chapter III. Various approaches, including dimensional analysis, sensitivity analysis, and finite element analysis were utilized to develop the design concepts of proposed CCBs-filled FRC poles.

Chapter IV discusses the properties of the component materials for CCBs-filled fiber-reinforced composite material, the laboratory test results of the fly ash particle size distribution, and general background information of matrix material and fiber glass. Chapter V conducts theoretical structural analyses and develops the design formulas for a cylindrical composite pole that relates the various dimension parameters of the composite pole with structural bending stiffness of the wooden pole. This chapter also utilizes multi-objective optimization techniques to identify the optimal composite pole design with consideration of material architecture, outer diameter, thickness, strength, and stiffness of the FRC pole.

Chapter VI discusses the prediction of the effective stiffness and strength of the roving layer and continuous strand mat (CSM) layer via a micromechanical analysis approach. Chapter VII discusses macro-mechanical behavior of individual lamina (roving layer and CSM), conducts a macro-mechanics analysis of CCBs-filled FR laminate based on classical plate theory. Various test methods used to evaluate the engineering properties of the CCBs – filled FR composite materials and the manufactured composite pole are given in Chapter VIII. To gain a better understanding of the failure mechanism for the manufactured composite pole, Chapter IX discussed the failure criterion and localized buckling failure that is most likely to occur at the bottom of the composite pole. Chapter X presents results of testing a full-size model composite pole to evaluate its engineering performance when subjected to flexural bending moment. Chapter XI presents economic evaluation of fabricating CCBs-filled composite utility poles. Chapter XII provides summary and conclusions based on the completed research and recommendations for future research and development.

CHAPTER 2: REVIEW OF PERTINENT LTERATURE

2.1 Fly Ash Characteristics

Table 2.1 shows the chemical composition of different oxides such as silicon, aluminum, iron and calcium oxides, etc for typical fly ashes (Chugh, 2000). Due to variation in silica content (36.1 to 48.48%), CaO content from (13.3% to 18%), and loss on ignition (6-18%), bonding behavior of CCBs with polymer, may vary.

Table 2.1 - Oxides composition of fly ash

Composition	F ash	C ash	FBC	Cement
LOI	7.11	1.65	9.73	-
SiO_2	40.99	45.45	36.10	21.79
Al_2O_3	15.73	16.98	13.89	4.46
Fe_2O_3	22.15	23.72	11.08	2.96
CaO	4.31	7.38	18.00	62.20
NaO_2	0.7	0.29	0.55	0.09
MgO	0.57	0.55	0.43	4.06
SO_3	2.57	1.62	8.23	2.69
K_2O	3.43	1.92	1.44	0.48
Mn_2O_3	0.15	0.16	0.08	-
P_2O_5	1.21	0.16	0.40	-
TiO_2	1.08	0.81	0.40	-

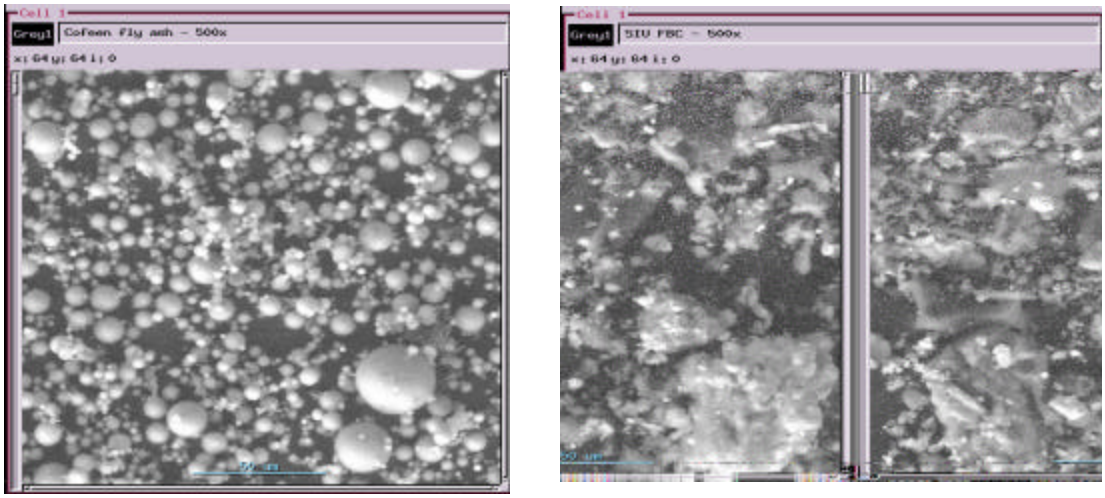

Figure 2.1 - F ash and FBC ash sample magnified by factor of 500

Figure 2.1 shows particle morphology of F-ash and FBC fly ash samples. Figure 2.2 shows the typical particle size distribution of SIU FBC fly ash (Chugh, 2002). The curve shows that about 96.4% of the FBC fly ash particles are smaller than 63 µm (-250 mesh) in size. The average particle size (D_{50}) is about 15 µm. Additional appropriate characteristics are given in Chapter 4.

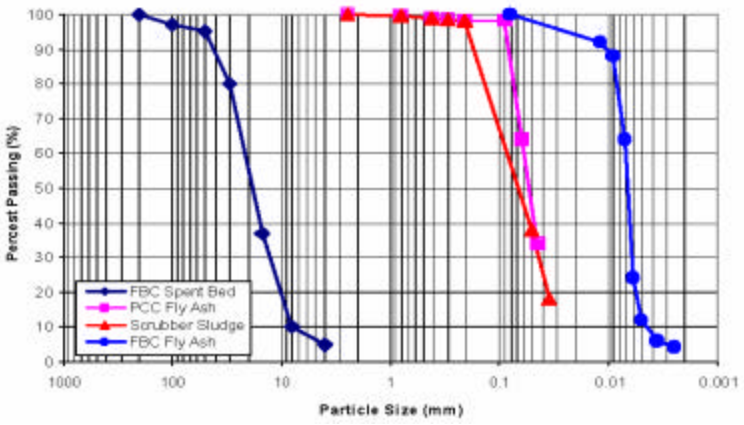

Figure 2.2 - Typical particle size distribution curve, for some CCBs (Chugh, 2002)

2.2 CCBs as filler in composite materials

CCBs have been attempted as filler in thermoplastic and thermo-set resins to make structural materials. Berry et al (1986) used F fly ash as filler material in plastics. In Poland (Crystyna et al, 1986), F fly ash micro-spheres were incorporated in polyurethane to develop composites. Kruger (1987) incorporated fly ash as aggregate in polymer concrete. In India, Srivastava and Shembekar (1990) evaluated the ultimate tensile strength, elastic modulus and fracture properties of epoxy resin filled with fly ash. They incorporated 105 µm mean particle size F fly ash, 20% by weight and found that the tensile strength decreased and elastic modulus increased with the increase in fly ash percentage. Chand (1994) developed F fly ash polyester composites with and without glass fibers and found that higher amount fly ash composites had higher wear loss. Rebeiz (1995) produced unsaturated polyester resin from plastic beverage bottles and mixed it resin with inorganic aggregates (sand and gravel and fly ash) to produce polyester concrete. He suggested that the material could be used in transportation and building components. Rebeiz et al (1995), in another study, found the time and temperature dependent properties of polymer-concrete composed of unsaturated polyester resin and inorganic aggregates (sand and gravel and fly ash). They reported the effect of age and temperature on strength and modulus. They incorporated 30% by weight of fly ash in the mix. The effect of the amount of fly ash on glass transition temperature, degradation temperature and tensile strength of polymer-concrete was also studied. They developed models to predict the strength and elastic modulus using the multiple regression models for polymer mortars using various percentages of fly ash (Rebeiz et al., 1995). Rebeiz et al. (1996a, 1996b) replaced sand with fly ash in polyester mortar and found that replacement of sand with fly ash was beneficial for the production of good quality polyester mortar. Saroja et al (1998) filled F fly ash in an unsaturated polyester resin and cast a sheet. They determined tensile and flexural strength and compared these

properties of fly ash filled unsaturated polyester composites with calcium carbonate filled polyester resin and found that the fly ash filled composite had poorer tensile and flexural strength properties. Fly ash filled unsaturated polyester composites were found to have a higher flexural modulus than those containing calcium carbonate. Fly ash filled unsaturated polyester composites with 10% fly ash were found to have poor acid and solvent (benzene) resistances, but good saltwater, alkali, weathering, and freeze–thaw resistances.

Mechanical properties of metal powder-filled modified methylene di-isocyanate based polyurethane foam were studied and it was found that the measured elastic modulus and strength values were in agreement with the theoretically predicted values (Goods et al, 1998). The results showed that the use of fly ash is beneficial for the production of good quality polymer mortar. They suggested that this polymer mortar could be used in a variety of construction applications such as overlay of pavements, dams and industrial floors. Recently, fly ash filled polyurethane foam composites were developed in India using 60% F-fly ash for replacing wooden doors and windows (Chand and Hashmi, 1999).

2.3 Micro-mechanical analysis of FRC

The aim of this analysis for composite materials is to characterize and predict the behavior of the material in an actual structural application. Although the material properties can be determined by actually testing specimens, there is considerable advantage in analytically predicting the material properties as a function of the properties of the constituent materials.

Many micro-mechanics stress analyses based on both analytical and numerical solutions have been presented in literature in the past. The Concentric Cylinder Model (CCM) is the simplest and the most commonly used. It is a closed-form analysis, but it neglects the effect of neighboring fibers on the local stress state. Therefore, it works well for composites with small fiber volume fraction (FVFs). However, this model has also been successfully used to determine effective properties of composites with large FVFs. Fiber interactions are accounted for in these models using a regular, periodic arrangement of the fibers. Common arrangements such as square and hexagonal arrays are typically considered. Aboudi (1988) presented theories based on the analysis of a rectilinear repeating cell representing a unidirectional composite. These theories are referred to as the “Method of Cells” and the “Generalized Method of Cells”. Finite element analyses and boundary element techniques were proposed by Adams and Crane (1984), and Achenbach and Zhu (1990). Whitney (1967) predicted the elastic modulus of a unidirectional composite with anisotropic filaments from available elasticity solutions and compared them with experimental data for Graphite-Epoxy specimens. His theoretical predictions seem to agree well with the experimental data.

2.4 Failure criteria for FRC materials

There are two different approaches to predict the laminate strength, namely, the ply-by-ply approach and the total laminate approach. In the first approach, the laminate is considered to consist of bonded layers. Each layer is considered to be homogeneous and orthotropic. Lamination theory is used to obtain the stresses and strains developed in each layer. These stresses and strains are transformed to the layer principal axes before the failure criterion is applied to each lamina. The failure envelope for the laminate is obtained by superimposing the failure envelopes of all the layers and determining the

innermost envelope. In the second approach, however, the lamination theory is not needed because the failure criterion is applied directly to the entire laminate, which is considered homogeneous but anisotropic. This approach requires the strength characterization of each laminate under consideration, whereas in the first approach the strength characterization is carried out on a layer and then the strength of any laminate under any stress state is predicted.

Hashin and Rotem (1973) proposed two failure mechanisms: one based on the failure of the fiber and the other based on the failure of the matrix. The first is governed by the longitudinal stress, with reference to the fiber orientation, and the second is governed by the transverse and tangential stresses in the fiber. It is assumed that there are two modes of failure: fiber breakage and matrix crack. The one not associated with the fiber breakage (called matrix failure mode) can be approximated by a quadratic function of transverse and tangential stresses. The assumption that the material is insensitive to the direction of shear stress cancels out the coupling term between the two stresses, leading to

$$(s_t / Y)^2 + (t / S)^2 = 1 \qquad \text{Equation (2.1)}$$

In the expression, s_t is the stress transverse to the fiber, and Y is its allowable value, while t is the tangential stress and S is its allowable value.

Hashin (1980) proposed two failure mechanisms: one associated with the fiber and the other associated with the matrix, distinguishing in both cases between tension and compression. The author recognized limitations and non-coherent consequences derived from the choice of a polynomial expression to represent the failure of the matrix.

Yamada and Sun (1978) proposed a failure criterion of a lamina in a laminate by means of the expression:

$$\left(\frac{s_{11}}{X}\right)^2 + \left(\frac{s_{12}}{S_{is}}\right)^2 = 1 \qquad \text{Equation (2.2)}$$

where, s_{11} and s_{12} are the longitudinal and tangential stresses, X is the strength of the lamina in the fiber direction, and S_{is} the in situ shear strength of the lamina.

Christensen (1988) developed a 3D stress-strain relation for a transversely isotropic material that can be expressed in a regular part, plus with a term, which only includes the effect of the deformation in the direction of the fiber, a term that the author relates to the effect of the reinforcement. The relation was written in terms of four material parameters (E_1, E_2, and, $?_{12}$ plus a term that represents the effect of the reinforcement). To reach such a conclusion, the author assumed different relations between properties of the material at the macro-mechanical level. The form obtained by this apparent constitutive equation led the author to propose a failure prediction based on two different criteria, one associated with the failure of the reinforcement and the other associated with the failure of the system matrix-interface. Although the two expressions of the criteria can be expressed in terms of stresses, the criteria are strain based.

Tsai-Hill failure criterion (1965) is a development of theory derived for metals considering distortional energy. A single equation is used to define the failure envelope, namely,

$$\left(\frac{s_1}{X}\right)^2 - \frac{s_1 s_2}{X^2} + \left(\frac{s_2}{Y}\right)^2 + \left(\frac{t_{12}}{S}\right)^2 \geq 1 \qquad \text{Equation (2.3)}$$

where, X and Y are taken as tensile or compressive strengths depending on the signs of s_1 and s_2, e.g. if $s_1>0$ then $X=X_t$. Note that within each quadrant (as defined by the s_1 - s_2 axes) this failure criterion represents a smooth and continuous curve. This failure criterion yields a good comparison between the predicted failure stresses and experimental data. However, this criterion does not identify the modes of failure. Furthermore, it does not take into account different behavior in tension and compression, which is very important for FRC.

The Tsai-Wu failure criterion (1971) overcomes some of the above limitations. The Tsai-Wu failure criterion is a phenomenological model with its derivation based on linking experimental constants rather than on a physical interpretation of material behavior. This criterion states that failure occurs when

$$A_{11}s_1^2 + 2A_{12}s_1 s_2 + A_{22}s_2^2 + A_{66}t_{12} + B_1 s_1 + B_2 s_2 \geq 1 \qquad \text{Equation (2.4)}$$

The coefficients are determined based on the material strengths as follows

$$A_{11} = \frac{1}{X_t X_c} \qquad B_1 = \frac{1}{X_t} - \frac{1}{X_c}$$

$$A_{22} = \frac{1}{Y_t Y_c} \qquad B_2 = \frac{1}{Y_t} - \frac{1}{Y_c}$$

$$A_{66} = \frac{1}{S^2}$$

The term A_{12} is obtained from bi-axial tests made on the lamina material. In the Tsai-Wu polynomial failure criterion, the determination of the interaction term A_{12} is crucial. A_{12} is not unique and can vary from negative to positive value.

2.5 Summary

This chapter covers typical characteristics of various fly ashes and surveys the relevant studies and research related to fly ash use as filler in polymers. Some of the existing micro-/macro-mechanical stress analysis and strength failure criteria are briefly reviewed. This chapter also reviews existing failure theories and design optimization techniques utilized for FRC structure design.

CHAPTER 3: DESIGN CONCEPTS FOR CCBS-FILLED FRC POLE

3.1 Introduction

This chapter briefly describes the design concepts for a CCBs-filled FRC utility pole. The design requirements for such a pole are presented based on the specifications of the ANSI class-4 wooden utility pole. Then various approaches, including dimensional analysis, sensitivity analysis and finite element analysis are utilized to develop the design concepts for proposed CCBs-filled FRC poles.

3.2 Design requirments for CCBs-filled composite utility pole

ANSI O5.1 - 1992 standards are currently utilized for wooden pole design. A typical Class-4, 35 ft long wooden pole has the following dimensions (Figure 1.2):

Circumference at the top of the pole	= 21 in.
Circumference at 6 ft above the butt	= 35.5 in.
Circumference at the pole bottom:	= 38.48 in.
Taper	= 0.0065 ft/ft length
Weight of the pole without treatment	= 1,100 lb

In the ANSI standard, the average outer-fiber strength of wood (6,000-8,000 psi) is used to calculate minimum circumference values for wooden poles, at the top of the pole and 6 ft above the butt. Another approach, suggested in Reliability Based Design, utilizes strength and stiffness values of pole material tested as a cantilever to develop pole dimensions. A class-4 wood pole, should sustain 2400 lb lateral load applied 2 ft from the top without failure. For such a pole, with elastic modulus of 1,200,000 psi for wood, the maximum top deflection of pole is estimated as 41.5 in. based on classical strength of materials analysis. The CCBs field utility pole must meet or exceed these specifications.

3.3 Laborotary testing of class-4 wooden poles

To determine flexural elastic modulus of commercial class-4 wooden poles, a three-point bending test system was designed at SIUC (Southern Illinois University Carbondale). The testing apparatus included a relatively stiff mechanical testing facility (Figure 3.1). This was used as support and reaction base (30 in. x 30 in.) for three-point test system. A 20-ton jack was used to apply force to the pole, and a force-measuring device was installed to monitor the applied load. To prevent localized damage to the wooden pole, steel plates (4 in. x 4 in. x 0.15 in.) were placed at the contact point between the pole and the reaction support roller and the jack, as shown in Figure 3.2. The bearing plates were supported by rollers so that rotation of the pole around the reaction due to deflection was unrestricted. To measure middle deflection more precisely, a U-shape beam was attached to both supports. Deflection-measuring device was mounted on this beam so that test errors due to the deformation of two supports were eliminated.

Figure 3.1- A 300,000 lb capacity compressive strength testing facility

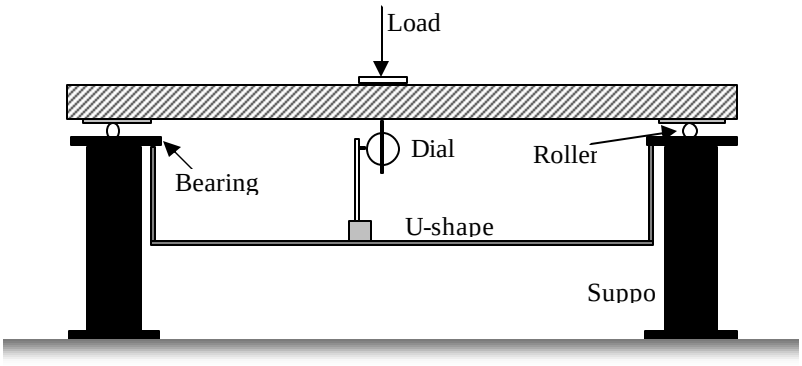

Figure 3.2 - Schematic plot of the three-point bending test apparatus

To calibrate the test system, a 6061-T6-type aluminum bar (4 ft in length and 3 inches in diameter) was tested. Using the above system, elastic modulus of the bar was found to be 9.55 million psi, which is close to the published value of 10 million psi. Several class-4 wood poles 4ft in length and 8.25 inch in diameter purchased from a local utility company were tested. Table 3.1 shows results for elastic modulus for these wooden pole tests and it was found as 401,650 psi.

Since 401,650 psi elastic modulus value is lower than the published value of 1,500,000 psi used by ANSI, a 1-ft tall column cut from the purchased wooden pole was also tested in compression mode for verification. Compression test of this column in a calibrated MTS machine revealed that the elastic modulus of wood is about 600,000 psi, around 50% of the failure stress.

To avoid localized failure at the supporting rollers contact points, some of the wooden pole samples were prepared of prismatic shape (6 in. x 6 in. x 42 in. long) instead of cylindrical shape (8 inch in diameter and 42 in. long) for testing. These tests found elastic modulus (E_{50}) for the wooden pole to be between 440,000 to 600,000 psi.

Table 3.1 - Three-point bending test data for a cylindrical wood pole

diameter (in)	8.25			
center-to-center length (in)	42			
gage precision (in)	0.001			
pressure (psi)	Raw data	Incre. Raw data	Incre. deflection (in)	
0	0			
500	53	53	0.053	
1000	92	39	0.039	Average value
1500	133	41	0.041	**0.0338**
2000	163	30	0.03	
2500	195	32	0.032	
3000	222	27	0.027	
Estimated tangent elastic modulus (50% failure stress:		401,648.73 psi		

Table 3.2 lists the specimen dimensions and the test results. We believe that the measured flexural stiffness of typical wooden utility poles of 1,500,000 psi, as indicated by ANSI may be too high. However, for a conservative design, a 1,200,000 psi elastic modulus was used for wooden pole to develop a comparable CCBs-filled FRC utility pole in this study.

Table 3.2 - Summary of three-point bending test results

Cross-section	Diameter / side (in.)	Equivalent E (psi)
Round	8.2	401,648
Round	8.18	585,277
Round	8.4	671,422
Square	6 x 6	438,958
Square	6 x 6	761,536
Round	8.14	573,491
Square	6 x 6	673,426
Square	6 x 6	625.437
Average		586,537
Standard deviation		130,073

3.4 Design considerations and proposed basic design

Development of composite poles requires consideration of the following variables.

1). Shape of the engineered composite pole: A wooden utility pole naturally tapers towards the top. An engineered composite pole can also be designed to taper toward the top (conical shape) to minimize weight and cost. However, decreased diameter and cross-section at the upper part of the pole will reduce torsional and flexural stiffness. Therefore, the pole with a smaller taper or even cylindrical shape should be considered. Fabrication of a cylindrical pole may be also cheaper.

2). Outer diameter and shell thickness: From a technical point of view, flexural stiffness, torsional stiffness, critical buckling load, and total weight are directly related to the outer diameter and outer-shell thickness of a composite pole.

3). Engineering properties of the outer-shell material: A utility pole is subjected to maximum stress at the bottom and maximum torsional stress near the top. Compressive strength, tensile strength, elastic modulus, post-failure behavior, flexural strength, and other durability characteristics are important in design.

4). Density of the outer-shell: Since total weight, cost, and engineering properties of the outer-shell and the inner-core material depend upon material unit weight, it is also important to consider these in designing the pole.

A conical-shape or cylindrical shape composite pole is illustrated in Figure 1.3.

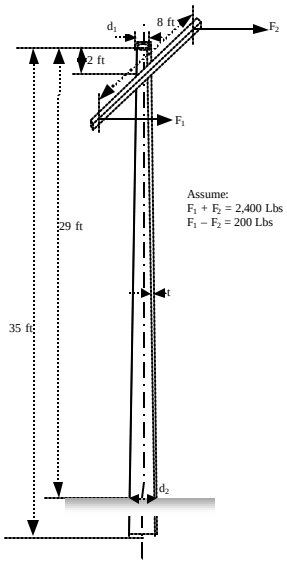

Figure 3.4 - Loading conditions for a class-4 composite pole

3.5 Theoretical analysis

A composite utility pole provides necessary flexural stiffness and torsional stiffness to resist bending moment and the torque caused by unbalanced horizontal pulling forces on both sides of the wire cross-arm. In addition, the pole may also be subjected to wind load, and the gravitational load due to the attachments (cross-arm, ladders, transformers and support guys). In this analysis, only the static load including the horizontal load of 2,400 lb as required by ANSI standard, twisting moment of 800 lb*ft (200 lb differential pulling force by 4 ft of cross arm length in one side), and the gravitational load were considered in the structural analysis. Other dynamic loads like

wind and snow were assumed to be negligible, and were considered through safety factor of two (2) in the analysis. A generalized conical pole structure (shown in Figure 3.4) was considered for analysis. The composite pole was subjected to horizontal load of 2400 Lbs and twisting moment of 800 Lbs *ft 2 ft below the top of the structure.

To determine the top deflection due to the horizontal pulling force and the twisting deformation due to the moment were analyzed separately and combined based on the principle of superposition.

Determination of top deflection:

A dummy horizontal load Q was added at the top of the pole. The free body diagram, shear force distribution, and bending moment distribution for the pole are shown in Figure 3.5.

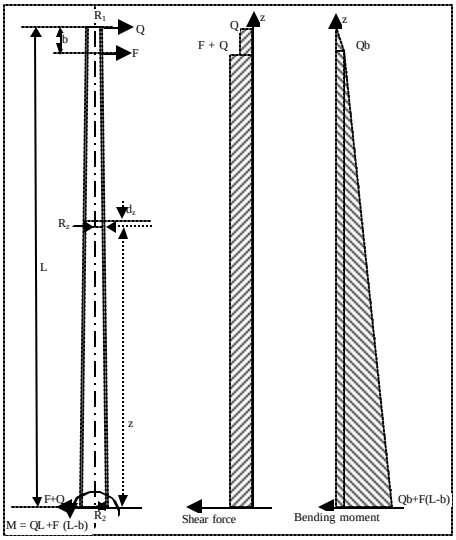

Figure 3.5 - Bending moment and shear force diagram for a utility pole

The strain energy of the whole structure is given as:

$$U = Um + Us \qquad \text{Equation (3.1)}$$

where, Um is the strain energy due to bending moment

$$Um = \int_0^{L-b} \frac{[(L-z)Q+(L-z-b)F]^2}{2[E_{core}I_{core}+E_{shell}I_{shell}]}dz + \int_{L-b}^{L} \frac{[(L-z)Q]^2}{2[E_{core}I_{core}+E_{shell}I_{shell}]}dz \qquad \text{Equation (3.2)}$$

Us is the strain energy due to shear force

$$Us = \int_0^{L-b} \frac{k(F+Q)^2}{2[G_{core}A_{core}+G_{shell}A_{shell}]}dz + \int_{L-b}^{L} \frac{kQ^2}{2[G_{core}A_{core}+G_{shell}G_{shell}]}dz \qquad \text{Equation (3.3)}$$

I_{core} is the moment of inertia for inner-core, $I_{core} = 0.25\pi(R_z\text{-}t)^4$,

I_{shell} is the moment of inertia for outer-shell, $I_{shell} = 0.25\pi[R_z^4\text{-}(R_z\text{-}t)^4]$,

R_z is the outer radius at the height of z from ground line, $R_z = R_2\text{-}(R_2\text{-}R_1)z/L$

A_{core} is the moment of inertia for inner-core, $A_{core} = \pi(R_z\text{-}t)^2$,

A_{shell} is the moment of inertia for inner-core, $A_{shell} = \pi[R_z^2\text{-}(R_z\text{-}t)^2]$, and

k is correction coefficient obtained as the ratio of the shear stress at the neutral surface of the beam to the shear stress, k = 2.0 for thin wall circular cross section.

By Castigliano's theorem, the deflection of the pole at the top is,

$$q = \frac{\partial U}{\partial Q}$$

$$= \frac{\partial Um}{\partial Q} + \frac{\partial Us}{\partial Q}$$

$$= \int_0^{L-b} \frac{[(L-z)Q + (L-z-b)F](L-z)}{[E_{core}I_{core} + E_{shell}I_{shell}]}dz +$$

$$\int_{L-b}^{L} \frac{[(L-z)Q](L-z)}{[E_{core}I_{core} + E_{shell}I_{shell}]}dz + \int_0^{L-b} \frac{k(F+Q)}{[G_{core}A_{core} + G_{shell}A_{shell}]}dz +$$

$$\int_{L-b}^{L} \frac{kQ}{[G_{core}A_{core} + G_{shell}G_{shell}]}dz \qquad \text{Equation (3.4)}$$

Since the dummy load Q does not exist, the deflection of the pole at the top is

$$q\big|_{Q=0} = \left.\frac{\partial U}{\partial Q}\right|_{Q=0} = \int_0^{L-b} \frac{(L-z-b)F(L-z)}{[E_{core}I_{core} + E_{shell}I_{shell}]}dz +$$

$$\int_0^{L-b} \frac{kF}{[G_{core}A_{core} + G_{shell}A_{shell}]}dz \qquad \text{Equation (3.5)}$$

A work sheet using MathCAD Plus 6.0 was developed for the above calculations. For verification purposes, top deflection of various composite poles, including class-4 wooden pole, were compared with finite element method (FEM) results, as given in Table 3.3. It is clear that the utility pole top deflection estimated using Castigliano's theorem has a very good agreement with that based on finite element analysis. Therefore, equation (3.5) was used to calculate top deflection for any proposed conical or cylindrical pole designs.

Table 3.3 - Comparison of deflection results from FEM and analytical approaches

model #	Pole Shape	Outer-shell Thickness (in)	Material	Diameter (in)		Top deflection (in)	
				top	butt	FEM	Analytical
1	Conical		Wood	6.68	11.3	42.22	41.5
2	Conical	0.375	CCBs	6.68	11.3	62.5	62.4
3	Conical	0.55	CCBs	6.68	11.3	49.1	48.3
4	Cylinder	0.375	CCBs	11.3	11.3	42.18	41.5
5	Cylinder	0.55	CCBs	11.3	11.3	37.48	32.2
6	Conical	0.375	CCBs	7.68	11.3	57	56.1
7	Conical	0.375	CCBs	7.68	13	39.23	39.1

Determination of torsional deformation *:*

The pole was assumed to be twisted by the torque generated by differential horizontal loads F_1 and F_2. The resulting twisting moment

$T = |F_1-F_2|*L_{arm}$

$= 200*4 = 800$ lb*ft

Figure 3.6 shows the twisting moment exerted by cross-arm and the reaction moment of the pole at ground line. The strain energy of the whole structure is

$$U = U_T \qquad \text{Equation (3.6)}$$

where U_T is the strain energy due to torsional load

$$U_T = \int_0^{L-b} \frac{T^2}{2[G_{core}J_{core} + G_{shell}J_{shell}]}dz \qquad \text{Equation (3.7)}$$

J_{core} is the polar moment of inertia for inner-core, $J_{core} = 0.5\pi(R_z-t)^4$,

J_{shell} is the polar moment of inertia for outer-shell, $J_{shell} = 2\pi R_z^3 t$,

R_z is the outer radius at the height of z from ground line, $R_z = R_2-(R_2-R_1)z/L$

G_{core} is the shear modulus for inner-core, $G_{core} = \frac{E_{core}}{2(1+m_{core})}$,

G_{shell} is the shear modulus for inner-core, $G_{shell} = \frac{E_{shell}}{2(1+m_{shell})}$,

E and m are elastic modulus and Poisson's ratio.

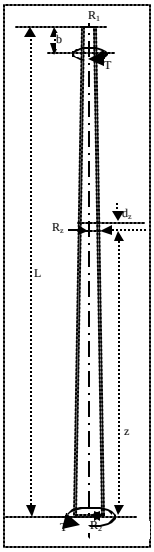

Figure 3.6 - Free body diagram for a pole subjected to twisting moment only

By Castigliano's theorem, the twisting angle q of the pole due to the differential horizontal pulling force is,

$$q = \frac{\partial U}{\partial T} = \int_0^{L-b} \frac{T}{[G_{core}J_{core} + G_{shell}J_{shell}]}\,dz \qquad \text{Equation (3.8)}$$

Assuming elastic modulus of 250,000 psi for inner-core material and 3,000,000 psi for the outer-shell material, a composite utility pole with 0.375 inch shell thickness and 10.75 inch outer diameter will be comparable to class-4 wooden pole in terms flexural bending stiffness. If such a pole is subjected to 800 lb*ft torque on the top due to unbalanced horizontal pulling force, its twisting angle will be 0.835 degrees using the MathCAD worksheet developed based on equation (3.8). As a comparison, a class-4 wooden pole has 1.198 degrees of twisting deformation when assuming elastic modulus of 1.2 million psi and Poisson's ratio of 0.2. Therefore, the engineered composite utility pole is 43% stiffer than wooden pole.

3.6 Dimensional analysis

Design, analysis, and testing of a CCBs-filled composite utility pole depend on many variables like shell thickness, outer diameter, engineering properties of inner-core and outer-shell, pole length, bending moment, external loads, etc. Analyzing or testing all potential combinations of these parameters, just to determine trends, would be enormously expensive. To simulate engineering behavior of a full size (35 ft long) composite pole, a model pole made of the same material should be developed for laboratory testing. Dimensional analysis techniques were used to design such a pole. Dimensional analysis makes understanding the effects of multiple variable changes possible with just a minimal amount of analysis/testing. This analysis searches for or

creates a small number of dimensionless variables that form the foundation for pole design.

The dimensional analysis was carried out for a number of independent variables. Dimensionless parameters or the π-terms were developed using Buckingham's π-theorem, 1914. A functional relationship was expressed between the π-terms such that

$$\pi_1 = f(\pi_2, \pi_3, \ldots\ldots\ldots\ldots\ldots\ldots\pi_n) \qquad \text{Equation (3.9)}$$

The function of the equation (3.9) can be written for both model and prototype. The subscript $_m$ stands for the model and $_p$ stands for the prototype. The relationship between π_{1m} and π_{1p} is obtained from the ratio.

$$\frac{p_{1p}}{p_{1m}} = \frac{f(p_{2p}, p_{3p}, \ldots\ldots\ldots\ldots\ldots\ldots\ldots p_{np})}{f(p_{2m}, p_{3m}, \ldots\ldots\ldots\ldots\ldots\ldots\ldots p_{nm})} \qquad \text{Equation (3.10)}$$

provided that the model is designed and tested such that

$$p_{2p} = p_{2m}$$
$$p_{3p} = p_{3m} \qquad \text{Equation (3.11)}$$
$$\ldots\ldots\ldots, \text{etc.}$$

If the above conditions are satisfied then

$$f(p_{2p}, p_{3p}, \ldots, p_{np}) = f(p_{2m}, p_{3m}, \ldots, p_{nm}) \qquad \text{Equation (3.12)}$$

and hence $p_{1p} = p_{1m}$

In the dimensional analysis for the CCBs-filled composite pole, variables considered in the analysis were outer-shell thickness t, diameter at the bottom d_1, diameter at the top d_2, length L, taper angle $\frac{d_1 - d_2}{2L}$, moment of inertia I, elastic modulus E, and bending moment M. Since the rank of the matrix is 2, the number of dimensionless products in a complete set is 7 – 2 = 5, which may be chosen as:

$$p_1 = \frac{d_1}{d_2},\ p_2 = \frac{ML}{E_1 I_1},\ p_3 = \frac{t}{d_1},\ p_4 = \frac{E_1}{E_2},\ p_5 = \frac{t}{d_2}$$

	d_1	d_2	t	Angle	I	E_1	E_2	M	L
M	0	0	0	0	0	1	1	1	0
L	1	1	1	0	4	-1	-1	2	1
T	0	0	0	0	0	-2	-2	-2	0

A functional relationship can be written for any one of the π-terms, for example, for the $\frac{d_1}{d_2}$

$$\frac{d_{1p}}{d_{2p}} = f1\left(\frac{M_p L_p}{E_p I_p}, \frac{E_{1p}}{E_{2p}}, \frac{t_p}{d_{1p}}, \frac{t_p}{d_{2p}}, \ldots\right) \qquad \text{Equation (3.13)}$$

where, *f1* is the undetermined function.

The equivalent expression for the model yields

$$\frac{d_{1m}}{d_{2m}} = f1\left(\frac{M_m L_m}{E_m I_m}, \frac{E_{1m}}{E_{2m}}, \frac{t_m}{d_{1m}}, \frac{t_m}{d_{2m}}, \ldots\right) \qquad \text{Equation (3.14)}$$

The condition of the model-prototype similitude is that the following design equations are satisfied:

$$\frac{M_p L_p}{E_p I_p} = \frac{M_m L_m}{E_m I_m}$$

$$\frac{E_{1p}}{E_{2p}} = \frac{E_{1m}}{E_{2m}} \qquad \text{Equation (3.15)}$$

$$\frac{t_p}{d_{1p}} = \frac{t_m}{d_{1m}}$$

$$\frac{t_p}{d_{2p}} = \frac{t_m}{d_{2m}}$$

and for this condition $\frac{d_{1p}}{d_{2p}} = \frac{d_{1m}}{d_{2m}}$

From the first part of equation (3.15), it can be rewritten as:

$$\frac{F_m}{F_p} = \frac{E_m I_m}{E_p I_p}\left[\frac{L_p}{L_m}\right]^2 \qquad \text{Equation (3.16)}$$

Equation 3.16 was used to calculate the load required for testing the model pole shown in Table 3.4.

Theoretical analyses revealed that, when the elastic modulus of the composite outer-shell material is 3 million psi, a hollow cylindrical composite pole with 11.5 in. outer diameter and 0.38 in. shell thickness will be comparable to a class-4 wooden pole. It was also found that, the composite pole would be 3% stronger (EI) and 63% lighter (weight) than a class-4 wooden pole. Thus, this design is considered as the most probable design. To test its engineering behavior in the laboratory, a 20 ft long model pole was tested in the lab in cantilever bending mode. Table 2.4 lists the dimensional parameters and engineering properties of both prototype (35 ft long full size pole) and the model pole. If the same outer-shell material was used for both poles, the 20 ft long model pole with 5-inch outer diameter, 0.25-inch shell thickness, and 382.02 lb horizontal load will satisfy the condition of the model-prototype similitude. In other words, such a model pole will simulate the full size hollow composite pole.

Table 3.4 - Results of dimensional analysis for a hollow cylindrical composite pole

Description	**Prototype**	**Model**
Length, L (ft)	35.00	20.00
Outer diameter, d1 (in)	11.50	5.00
Outer radius, r1 (in)	5.75	2.50
Thickness, t (in)	0.38	0.25
Inner radius r2, (in)	5.38	2.25
Eout (psi)	3,000,000	3,000,000
Ein (psi)	0	0
MOI * for shell (in^4)	202.99	10.55
MOI for Inner-core (in^4)	655.55	20.13
Combined EI	608,983,661	31,652,159
Horizontal Force , F (lb)	2400.00	382.00

* moment of inertia

3.7 Utility pole design using finite element method

Finite element method was also used to analyze and compare the response behavior of the wooden pole and the composite utility pole. The FEM modeling considered following three variables:

1) shape of the pole (conical or cylindrical);

2) outer diameter of the pole;

3) thickness of the outer-shell.

Finite element analysis software (Algor) was utilized that can carry out static and dynamic displacement and stress analysis of solids, structures, fluid flow, and heat transfer, among others. This software can be used to perform linear and nonlinear analysis with various failure criteria. For the 3-D flexible brick elements, sandwich elements, gap element, contact elements, truss elements, and beam elements are available for analyzing this problem. Full-scale composite utility pole models were developed using a three-dimensional 6-node or 8-node flexible brick element. Table 3.5 shows the dimensions of the Class-4, 35-ft high utility pole that was used in the finite element modeling. A horizontal force of 2,400 lb was applied to the pole 2 ft below the top, as shown in Figure 3.6.

Since 6 ft of the pole is usually buried in the ground, only the portion above-ground (29 ft long) was simulated. The bottom of the model is constrained in both horizontal and vertical directions. Material properties used in the above models are listed in Table 3.6. Figure 3.6 shows a conical and a cylindrical utility pole model used for FEM analysis. The pole models are either conical or cylindrical in shape, as shown in Figure 3.7 and Table 3.7. For the purpose of comparison, a wooden utility pole model (model #1 in Table 3.7) was developed first as the base model. Then, seven models

(model #2 to #8 in Table 3.8) were developed with different outer-shell thickness and shape of the pole. The outer-shell thickness was either uniform (0.25 inch, 0.375 inch, and 0.55 inch, respectively) or varied from 0.125 inch at the top to 0.375 inch at the bottom. Table 3.8 shows the value of top deflection and maximum principal stress for each model.

Table 3.5 - Dimensions of the composite utility pole model

Top:	diameter = 6.68 in;	circumference = 21 in
6 ft from bottom:	diameter = 11.3 in;	circumference = 35.5 in
Bottom:	diameter = 12.24 in;	circumference = 38.48in
Taper:	0.0065 ft/ft length	

Table 3.6 - Material properties for utility pole design

Material	Elastic modulus (psi)	Poisson's ratio	Compressive strength (psi)	Unit weight (pcf)	Shear modulus (psi)
Inner-core	250,000	0.25	6,000	30	100,000
Outer-shell	3,000,000	0.1	30,000	80	1,363,636
Wood	1,500,000	0.2	9,000	50	625,000

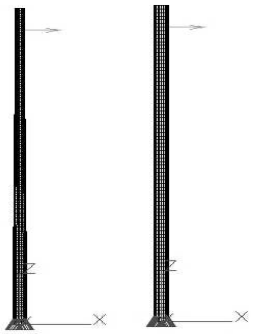

Figure 3.7 - FEM models of conical and cylindrical pole models

Figure 3.8 shows a deflected cylindrical pole model and Figures 3.9 to 3.11 illustrate the minimum principal stress distribution at the bottom of the pole.

A conical composite pole with similar dimensions as a wooden pole and with outer-shell thickness of 0.375 in. and 0.55 in. yielded top deflections of 62.5 in. and 49.1 in., respectively, which are 153% and 48.1% higher than a wooden pole.

- Changing the taper of the pole (model 3 → model 9→ model 7) proved that horizontal deflection at the top decreased as the taper decreased. A cylindrical pole with 0.375 in. outer-shell thickness is comparable to an ANSI wooden conical pole.
- Analysis of the results also revealed that a larger diameter conical pole (model 10, 0.375 in. outer-shell thickness, top and bottom diameter of 7.685 in. and 14 in., respectively) is comparable to a class-4 wooden conical pole based on bending stiffness.

Table 3.7 - FEM models and results for composite utility pole

Model #	Pole Shape	Outer-shell Thickness (in)	Material	Diameter (in)		Range of major Principal stress (psi)		Deflection on top (in)
				Top	Butt	Max.	Min.	
1	Conical		Wood	6.68	11.3	1,347	-5,773	42.2
2	Conical	0.25	Composite	6.68	11.3	3,351	-32,170	107.1
3	Conical	0.375	Composite	6.68	11.3	1,868	-18,611	62.5
4	Conical	0.55	Composite	6.68	11.3	1,467	-14,437	49.1
5	Conical	0.125 top, 0.375 butt	Composite	6.68	11.3	1,913	-19,506	74.7
6	Cylindrical	0.25	Composite	11.3	11.3	2,296	-22,352	205.
7	Cylindrical	0.375	Composite	11.3	11.3	1,898	-18,433	42.2
8	Cylindrical	0.55	Composite	11.3	11.3	1,677	-16,518	37.5
9	Conical	0.375	Composite	7.68	11.3	1,904	-18,470	57.0
10	Conical	0.375	Composite	7.69	13.0	1,349	-13,452	39.2

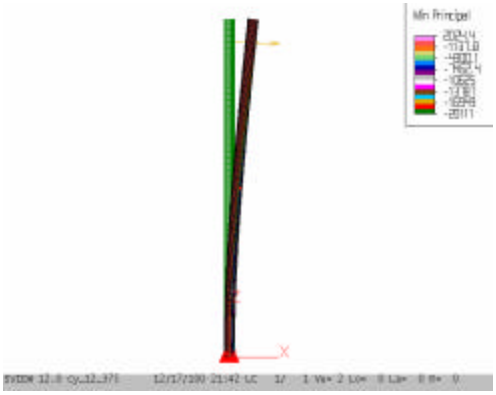

Figure 3.8 - Deflection of an engineered composite utility pole

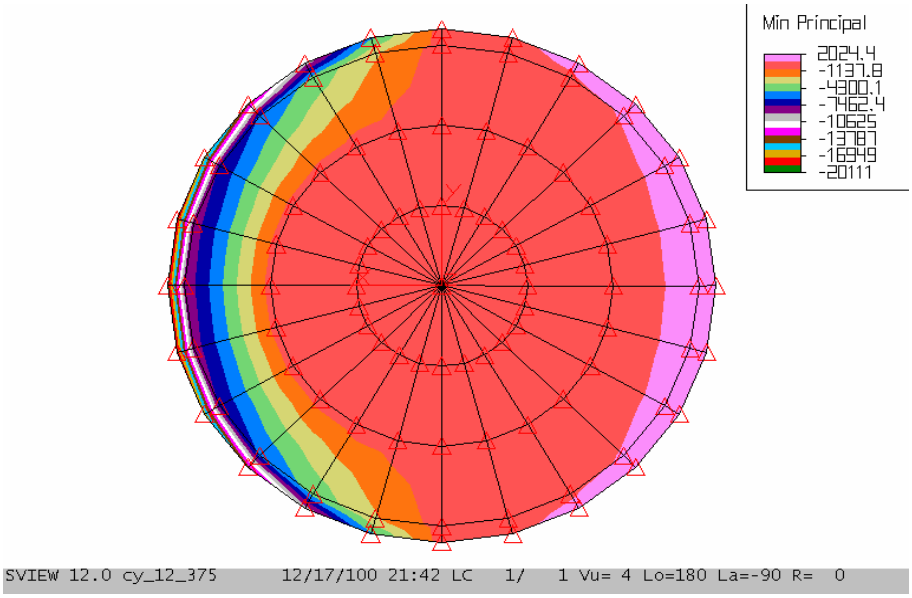

Figure 3.9 - Stress distribution in a pole (plan view at bottom)

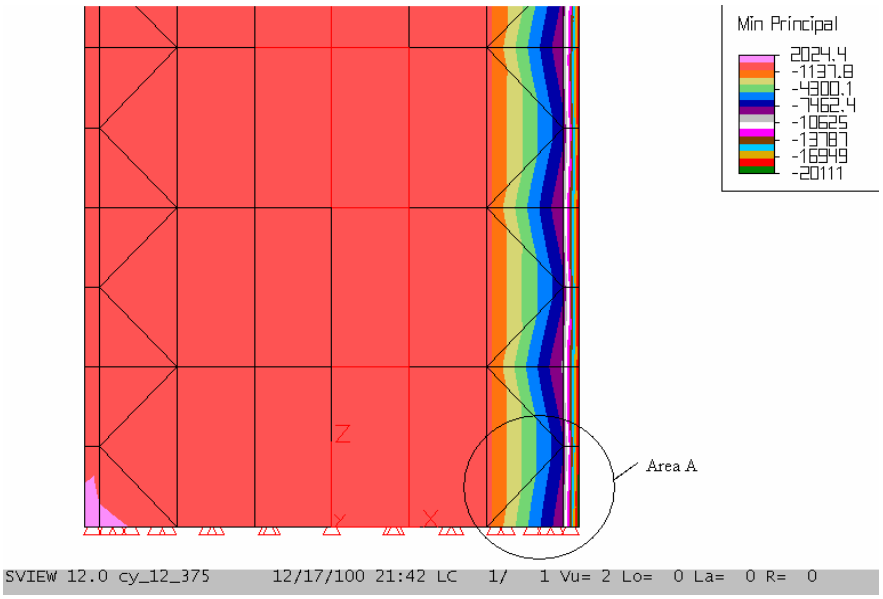

Figure 3.10 - Stress distribution at the bottom portion of the pole (axial cut view)

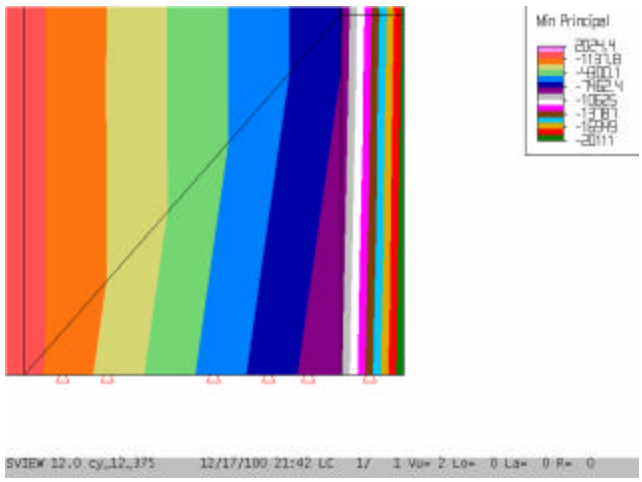

Figure 3.11 - Detailed view of area A in Figure 3.10

To analyze the effects of engineering properties of the inner-core material, outer diameter of the pole, and the inner-core filling height on the maximum principal stress as well as top deflection, five (5) additional models were analyzed (Table 3.8).

- Diameter of the outer-shell is the most important factor affecting the stability of the pole.
- Stiffness of the inner-core material must be high if the outer diameter of the composite pole is to be similar to the bottom diameter of a conical wooden pole. A composite utility pole with 0.375 in. of outer-shell thickness, 12 in. of outer-shell diameter, and 50,000 psi elastic modulus of inner-core would be comparable to the wooden pole. Figure 3.12 shows the top deflection of such a pole with that of a class-4 wooden pole. The engineered composite utility pole is slightly stiffer than a wooden pole.

Finite element analysis was also conducted to investigate the torsional deformation for both composite pole (hollow) and wooden pole due to the differential horizontal pulling force on the cross-arm of the pole (Figure 3.13 and Figure 3.14)

Table 3.8 - Additional FEM results for a composite utility pole

Outer diameter = 11.3 in, outer-shell thickness = 0.375 in.					
Property of inner-core		Top deflection (inch)	Range of maximum principle stress (psi)		Height of inner-core fill
E (psi)	Density (psi)				
50,000	25	51	2,299	-22,340	Full length
100,000	30	48.4	2,183	-21,213	Full length
150,000	35	46.1	2,299	-22,340	Full length
250,000	40	42.2	1,897	-18,433	Full length
250,000	40	43.5	1,899	-18,415	Half length
300,000	35	40.5	1,819	-17,657	Full length
300,000	35	41.9	1,820	-17,645	Half length
400,000	35	37.4	1,679	-16,296	Full length
400,000	35	39.2	1,681	-16,285	Half length
500,000	35	34.8	1,560	-15,132	Full length
500,000	35	36.9	1,561	-15,122	Half length
0	0	54.1	2,58	-32,812	Hollow
Outer diameter = 10 inch, outer-shell thickness = 0.375 in.					
500,000	35	52.3	2,034	-20,398	Full length
800,000	35	43.7	1,678	-16,899	Full length
1000000	35	39.6	1,503	-15,167	Full length
Outer diameter = 12 inch, outer-shell thickness = 0.375 in.					
50,000	35	42	2,024	-20,111	Full length
100,000	35	39.7	1,907	-18,976	Full length
200,000	35	35.8	1,709	-17,041	Full length
Outer diameter = 13 inch, outer-shell thickness = 0.375 in.					
50,000	35	33.8	1,780	-17,717	Full length

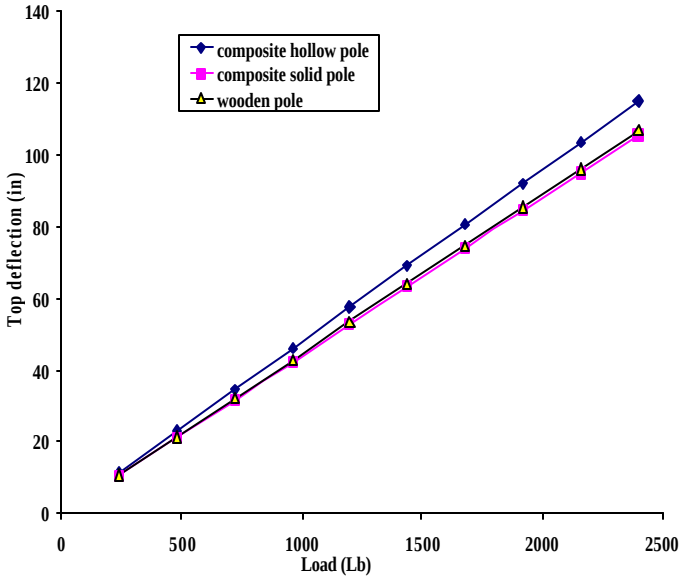

Figure 3.12 - Comparison of top deflection for composite pole and wooden pole

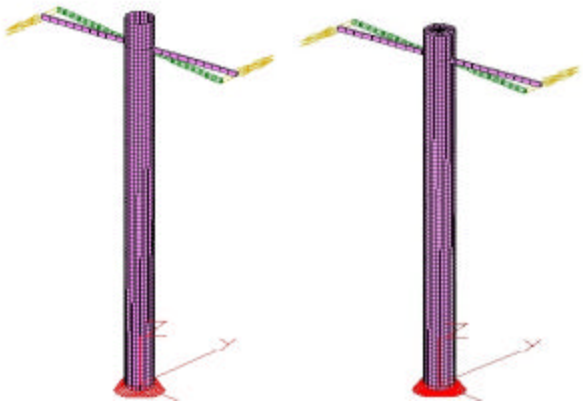

Figure 3.13 - Torsional deformation of the hollow and filled composite pole (x 10)

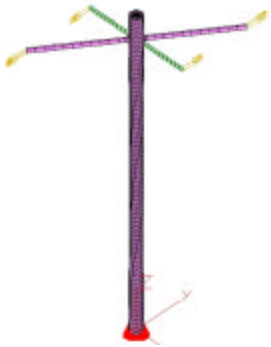

Figure 3.14 - Torsional deformation of a wooden pole (x10)

The figures clearly illustrates that the class-4 wooden pole has less torsional stiffness than the composite pole even though they have similar flexural bending stiffness. Figure 3.15 compares the torsional deformation for both poles under different twisting moments. Figure 3.16 shows the top view of the stress distribution on the wooden pole and cross arm and torsional deformation.

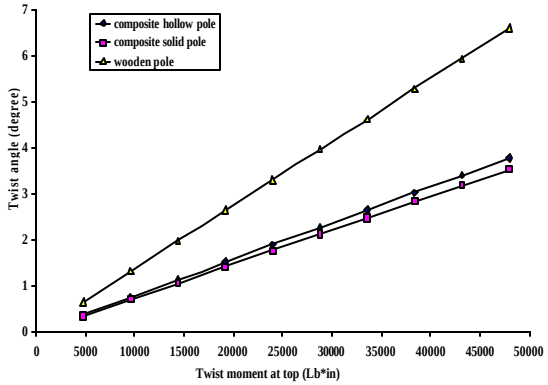

Figure 3.15 - Comparison of the torsional deformation for filled and unfilled composite pole and wood pole

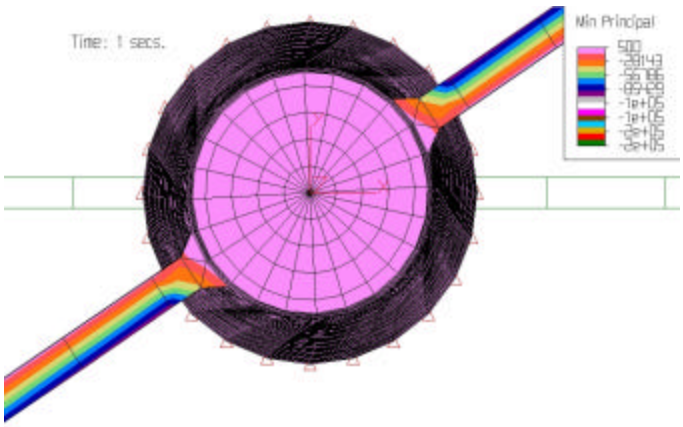

Figure 3.16 - Stress distribution and torsional deformation of wood pole (top view)

The analyses described above form the foundation for development of CCBs-filled composite utility poles.

CHAPTER 4: DEVELOPMENT OF CCBS-FILLED POLYMERIC COMPOSITE MATERIAL

4.1 Introduction

The general background information on matrix material and fiber glass is introduced. Mix compositions are developed for the outer-shell material (using 5 to 30% CCBs and polymer). Compressive strength and elastic modulus are used for screening tests to develop proper mixes. Effects of fly ash loading percentage, particle size, curing time temperature, and post-curing time on engineering properties of the developed composite materials are analyzed based on statistical design.

4.2 Component material characterization

FBC fly ash from was used as the solid filler in polyester polymers to develop CCBs-filled composite. Fiberglass was added as reinforcement to increase the material stiffness and strength.

Selection of fly ash:

Prior to deciding on the FBC fly ash in this study, several fly ashes (F-ash, C-ash, FBC ash) were evaluated experimentally. SIU power plant FBC fly ash gave the best results in terms of enhanced material stiffness and strength. Oxides composition for this FBC fly ash is given in Table 4.1.

Table 14.1 - Oxides composition of the SIU FBC fly ash

Chemical composition	Percentage
SiO_2	31.3
Al_2O_3	10.6
Fe_2O_3	8.3
SO_3	12.8
CaO	20.9
MgO	0.4
LOI	14.7
Free Moisture	0.11
Water of hydrogen	0.71
Total Na_2O	0.4
Total K_2O	1.1
Others (TiO_2+P_2O_5+SrO+BaO)	0.83

Particle size distribution of fly ash :

It is an important property when utilized as a filler. Thus, wet size distribution analysis was conducted on oven-dried FBC fly ash. After measuring the total initial weight of the

oven-dried fly ash sample, it was mixed with water, and the slurry was shaken through a stack of sieves with openings of decreasing size from top to bottom. The sieves used in this analysis were No 70, No 100, No 120, No 140, No 200, No 250, No 270, No 325, No 400, and No 500. For –500-mesh (25.4 µm) material, size distribution analysis was conducted using Microtrac particle size analyzer

Results for both tests were combined and the complete particle size distribution curve was developed, as shown in Figure 4.3. About 96.4% of the FBC fly ash particles are smaller than 63 µm (-250 mesh) in size. The mean particle size (D_{50}) was found to be about 15 µm. Some related parameters are listed in Table 4.2. Since the uniformity coefficient is greater than 4, the fly ash is considered as poorly graded. More than 80% of particles are within the range of 5- 44 microns size.

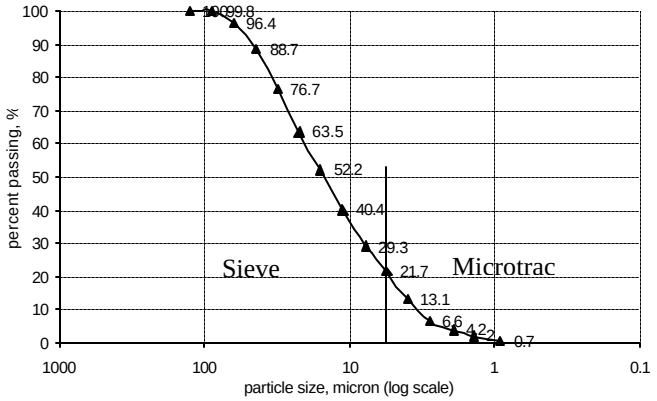

Figure 4.3 - Particle size distribution curve for FBC fly ash

Table 4.2 - Size analysis related parameters for FBC fly ash

Effective size D10:	3.3	micron
D25:	6	micron
D30:	8	micron
D50:	15	micron
D60:	20	micron
D75:	30	micron
Uniformity coefficient Cu:	6.06	
Coefficient of gradation Cc:	0.97	
Sorting coefficient So:	2.24	

Solid specific gravity of fly ash:

It was determined using AASHTO T100-95 – Standard Specification for Specific Gravity of Soils. The average specific gravity of the solid ash particles was 2.66.

Characteristics of matrix material:

The matrix material holds the fibers together, and transfers the load between fibers and between the matrix and the fibers. It also protects the fibers from the environment and mechanical abrasion and carries some of the loads, particularly transverse stress and interlaminar shear stress.

Polymer matrices are the most commonly used type of composite material matrix. The polymer matrix can be either a thermo-set or a thermoplastic. The most common thermo-set resins are polyesters, vinyl-ester, epoxy, and phenolics. Polyester was selected to develop the outer-shell material for proposed CCBs-filled composite utility pole. A thermo-set matrix is formed by the irreversible chemical transformation of a resin system into an amorphous cross-linked polymer matrix. Thermo-set resins have low viscosity that allows for excellent impregnation of the fiber reinforcement and high processing speeds. Thermo-set polymers are the most common resin systems used because of their ease in processing and low cost resin. Gel time (ASTM D2471) is the time the mixed resin can be handled before the viscosity increases to a point where processing is no longer possible. Depending on the choice of catalyst and the reactivity of the resin, cure cycles can vary from minutes to hours, and they occur at room temperature or at high temperature. The reactions are exothermic and gelation is usually rapid. Gelation occurs when the resin has reached a point at which the viscosity has increased so much that the resin barely moves when probed with a sharp instrument. Curing systems do not greatly affect the end properties of a resin but affect the storage life and processing conditions. Once cured, the mixture thickens, releases heat, solidifies, and shrinks. The volumetric shrinkage upon curing varies from 4% for epoxy to 8% for polyester. All resins provide higher thermal insulation than most commonly used construction materials. Vinyl-Esters have high strength while polyesters have moderate strength. Epoxy resins are considered high performance resins since strength is superior to other thermo-sets.

Characteristics of glass fiber:

Fibers are used in composites because they are lightweight, stiff, and strong. Fibers are stronger than the bulk material that constitutes the matrix. This is because of the preferential orientation of molecules along the fiber direction and because of the reduced number of defects present in a fiber as compared to the bulk material matrix. Fibers are used as continuous reinforcements in unidirectional composites by aligning a large number of them in a thin plate or shell, called lamina, layer, or ply. A unidirectional lamina has maximum stiffness and strength along the fiber direction and minimum properties in a direction perpendicular to the fibers. When the same properties are desired in every direction on the plane of the lamina, randomly oriented fibers are used. The resulting composite has the same properties in every direction on the plane of the lamina, and it is weaker in the thickness direction.

Glass fibers exhibit the typical glass properties of hardness, corrosion resistance, and inertness. Furthermore, they are flexible, lightweight, and inexpensive. These properties make glass fibers the most common type of fiber used in low-cost industrial

applications. The high strength of glass fibers is attributed to the low number and size of defects on the surface of the fiber. All glass fibers have similar stiffness but different strength values and different resistance to environmental degradation.

4.3. Preliminary outer-shell material development

The goal of the studies was to find the optimum ratio of the fly ash to polymer suitable for the outer-shell material. Mixes were prepared with six different percentages of fly ash loading levels: 0%, 5%, 10%, 15%, 20% and 25%. Initial analysis of the outer-shell material was based on the determination of three strength characteristics: compressive strength, C_0; elastic tangent modulus, E(t); and the elastic secant modulus, E(s). All tests followed ASTM standards. At this stage the analysis did not consider the fiberglass mesh that was eventually incorporated into the outer shell. No attempt was made to entrain air in these samples (full density).

Initially, F fly ash from the Lake of Egypt Power Plant of Southern Illinois Power Coop in Marion, Illinois, was used. The cubical samples (2 inch x 2 inch x 2 inch) prepared were tested in a MTS loading machine. The upper surfaces of the samples were ground flat and smooth using a grinding wheel (Figures 4.7 and 4.8). After measuring the dimensions of the prepared cubical sample, the samples were loaded at the rate of 1.25 MN/min until the sample failed.

Figures 4.9 and 4.10 show the results obtained. Each set of samples were divided into two separate groups; Samples A and B were cured for 12 hours at ambient temperature. Samples C and D were cured at ambient temperature first and then post-cured at 160 degrees F for 24 hours. The samples were then tested for their compressive strength and elastic modulus. Table 4.3 lists the results. Samples with 15% fly ash mixture were found to have the highest average compressive strength of 15,170 psi with the average tangent elastic modulus (Et) of 367,450 psi and the average secant elastic modulus (Es) of 219,600 psi.

Table 4.3 - Compressive test results for inner-core material (full density)

Sample #	Compressive Strength Qu, psi		Tang. Elastic. Modulus, Et, psi		Sec. Elastic Mod., Es, psi		% Fly ash	Curing Temp.
	Value	Average	Value	Average	Value	Average		
1A	13,896	14,033	316,600	313,100	218,000	207,500	0	ambient
1B	14,170		309,600		197,000		0	ambient
1C	13,642	12,812	316,500	312,250	201,600	190,300	0	160 F
1D	11,982		308,000		179,000		0	160 F
2A	13,507	13,521	307,000	308,625	188,000	185,500	5	ambient
2B	13,535		310,250		183,000		5	ambient
2C	13,730	14,043.5	302,500	301,750	210,000	204,400	5	160 F
2D	14,357		301,000		198,800		5	160 F
3A	N/A	13,306	N/A	281,300	N/A	204,200	10	ambient
3B	13,306		281,300		204,200		10	ambient
3C	13,953	14,055.5	326,400	330,600	195,400	223,950	10	160 F
3D	14,158		334,800		252,500		10	160 F
4A	14,241	14,287	336,300	326,600	214,300	200,900	15	ambient
4B	14,333		316,900		187,500		15	ambient
4C	14,871	15,170	367,600	367,450	226,400	219,600	15	160 F
4D	15,469		367,300		212,800		15	160 F
5A	13,157	12,912	301,200	298,200	199,700	205,250	20	ambient
5B	12,666		295,200		210,800		20	ambient
5C	13,821	14,000	307,250	316,075	206,500	192,650	20	160 F
5D	14,179		324,900		178,800		20	160 F
6A	11,294	10,272	223,400	199,050	154,000	136,100	25	ambient
6B	9,250		174,700		118,200		25	ambient
6C	10,478	11,267	241,200	258,800	141,700	145,500	25	160 F
6D	12,056		276,400		149,300		25	160 F

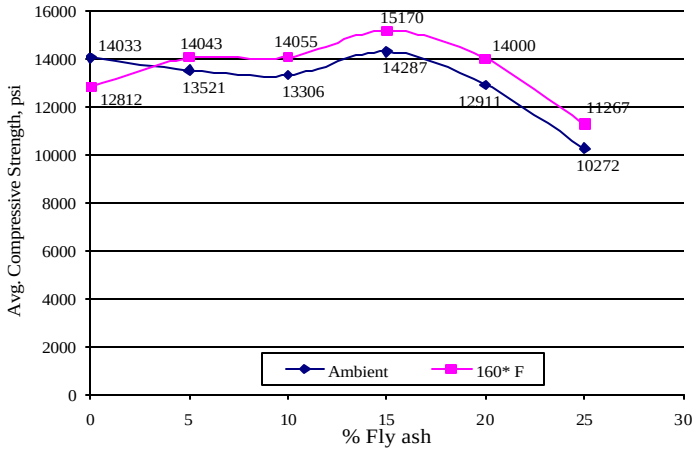

Figure 4.9 - Compressive strength vs. fly ash % at different curing temperatures

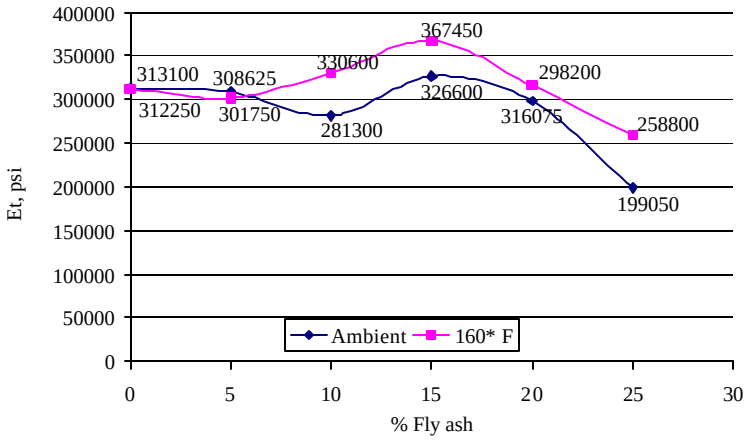

Figure 4.10 - Tangent elastic modulus vs. fly ash % at different curing temperatures

4.4 Outer-shell material development using statistical experimental design

Based on the above preliminary compressive test results, a statistical mix design program was developed to evaluate the effect of FBC fly ash percentage, curing temperature, and post-curing time on the outer-shell engineering properties such as elastic modulus and ultimate strength. Goals of the statistical experimental design were to:

- Quantify the relationships between the five measured response variables and the three independent variables (Table 4.4).
- Find a desirable point in the design space where optimal response is achieved. In other words, mix designs for making optimal outer-shell composite material were to be identified.
- Evaluate interaction effect of three variables on five response variables.
- Meet a set of specifications for several responses simultaneously.

Statistical experiment design:

Three proportions of FBC fly ash (10%, 14% and 18%) were mixed and cured at three curing temperatures (140 F^o, 160 F^o, and 180 F^o). In addition, three levels of post-curing time (8 hr, 16 hr, and 24 hr) were also adopted (Table 4.4). The significance of each variable factor was estimated based on the observed values of dependent variables.

Table 4.4 - Factors and responses considered in the design

Independent and response variables		unit	Range	note
Independent variables	Fly ash %	%	10, 14, 18	3 level
	Mixing time	min	1.5	fixed
	Curing temperature	F	140, 160, 180	3 level
	Post-curing time	hour	8, 16, 24	3 level
	Resin temperature	F	78	Fixed
Response variables	1. Tangent elastic modulus			
	2. Failure strength			
	3. Gel time.			
	4. Perk exothermic temperature.			
	5. UV degradation potential			

Response surface design approach (Design Expert 6.0, 2000) resulted in seventeen (17) tests with different test parameters. Each test was replicated five (5) times to give an adequate estimate of the variation of the response and provide the needed number of degrees of freedom. Thus, eighty-five (85) samples were needed. Ashland Chemicals approved this experimental design, as shown in Table 4.5. In addition, to compare the engineering properties of the CCBs-filled samples with pure resin samples, three more runs (9 samples total, three for each run) were appended to the design by changing post-curing temperature (140 F^o, 160 F^o, and 180 F^o) and by maintaining 0% fly ash loading level and 8 hr post curing time.

Table 4.5 - Design matrix

Run ID	Factors considered		
	Fly Ash %	Curing Temperature, F^o	Post-curing time, hr
1	18	180	16
2	14	180	8
3	14	160	16
4	14	160	16
5	14	140	24
6	10	160	8
7	18	140	16
8	14	140	8
9	14	160	16
10	14	160	16
11	10	180	16
12	10	140	16
13	18	160	8
14	10	160	24
15	14	160	16
16	18	160	24
17	14	180	24

Theoretical analysis background:

Let us assume three independent factors as follows:

x_1, fly ash percentage, %, (factor A)

x_2 curing temperature, F^o, (factor B)

x_3 post-curing time, hr, (factor C)

The treatment of dependent variable *y*, can be any of the engineering properties mentioned earlier, such as elastic modulus, ultimate strength, etc. The analysis of variance (ANOVA) was used to evaluate the effect of each factor and combination of factors based on laboratory test data. The statistical model of expected values of dependent variable can be written as:

$$E(y) = b_0 + \underbrace{b_1 x_1}_{\text{Effects of Fly ash percentage}} + \underbrace{b_2 x_2}_{\text{Effects of curing temperature}} + \underbrace{b_3 x_3}_{\text{Effects of post curing time}}$$

$$+ \underbrace{b_4 x_1^2}_{\text{Quadratic effects of Fly ash percentage}} + \underbrace{b_5 x_2^2}_{\text{Quadratic effects of curing temperature}} + \underbrace{b_6 x_3^2}_{\text{Quadratic effects of post curing time}} \qquad \text{Equation (4.1)}$$

$$+ \underbrace{b_7 x_1 x_2}_{\text{Interaction effects of of Fly ash \% and curing temperature}} + \underbrace{b_8 x_1 x_3}_{\text{Interaction effects of Fly ash \% and post curing time}} + \underbrace{b_9 x_2 x_3}_{\text{Interaction effects of of curing temperature and post curing temperature}}$$

The significance of each coefficient β_i (i = 0,…,9) was obtained using the F-test in ANOVA. For each effect and their combinations, as shown in the above equation, mean square error (MSE) and sum square error (SSE) was calculated from the engineering parameters estimated from laboratory tests. The F values were compared with 95% confidence level to evaluate the significance of each factor. The R square value (R^2) for each model was also estimated along with the importance coefficient for each factor.

Eighty (80) out of ninety four (94) samples were found valid for statistical analysis after laboratory testing. The averaged test results are shown in Table 4.6.

Table 4.6 - Engineering properties of various mixes

run #	Avg compressive strength, psi	Avg tangent elastic modulus, psi	Standard deviation of compressive strength, psi	Standard deviation of tangent elastic modulus, psi
1	14,259	482,068	20,679	516
2	14,839	468,705	11,906	241
4	15,566	499,521	17,485	328
5	14,513	444,706	29,970	1,419
6	13,796	405,043	6,977	393
7	15,365	467,210	12,635	307
8	13,463	383,001	25,813	706
9	14,211	414,403	9,171	90
10	15,487	458,219	15,037	322
11	16,032	472,486	7,516	378
12	17,009	513,314	9,388	311
13	15,866	476,393	15,512	341
14	14,943	447,568	5,071	179
15	16,774	502,786	407	362
16	16,645	480,687	8,608	167
17	15,460	494,434	1,200	157

Results and discussions:

Analysis of variance showed that fly ash percentage (A), post-curing temperature (B), post-curing time (C), and interaction of post-curing time and temperature (B*C) are the most significant factors in determining the failure strength, as shown in Table 4.7. A linear regression model was developed below:

Compressive Strength = 23555.3 - 215.3* A

-38.7 * B - 716.7 * C+4.9 * B * C

Equation (4.2)

A similar analysis for elastic modulus revealed that fly ash percentage (A), post-curing temperature (B), post-curing time (C), and square of post-curing temperature (B2), interaction of fly ash percentage and post-curing temperature (A*B), are the significant factors, respectively, as shown in Table 4.8. A quadratic model was developed to relate the value of elastic modulus with three input factors, as shown below:

Elastic Modulus = -4.3E5 - 36272.2 * A

+ 12895.2 * B

+1415.7 * C - 43.2 * B^2
+194.20531 * A * B

Equation 1(4.3)

Table 4.7 - ANOVA table of compressive strength of outer-shell material

Source	Sum of Squares	Degree of freedom	Mean Square	F Value	Prob > F	Remarks
Model	1.56E+07	4	3.90E+06	7.73	0.0025	Significant
A	5.93E+06	1	5.93E+06	11.75	0.0050	Significant
B	5.00E+06	1	5.00E+06	9.90	0.0084	Significant
C	2.23E+06	1	2.23E+06	4.42	0.0573	
BC	2.45E+06	1	2.45E+06	4.85	0.0479	Significant
Residual	6.06E+06	12	5.05E+05			
Lack of Fit	3.60E+06	8	4.50E+05	0.73	0.6738	Insignificant
Pure Error	2.46E+06	4	6.16E+05			
Correlation Total	2.17E+07	16				

Table 24.8 - ANOVA table for elastic modulus of the outer-shell material

Source	Sum of Squares	DF	Mean Square	F Value	Prob > F	Remarks
Model	1.69E+10	5	3.38E+09	9.49	0.0010	significant
A	3.46E+09	1	3.46E+09	9.72	0.0098	
B	1.02E+10	1	1.02E+10	28.58	0.0002	
C	1.03E+09	1	1.03E+09	2.88	0.1176	
B2	1.27E+09	1	1.27E+09	3.56	0.0859	
AB	9.66E+08	1	9.66E+08	2.71	0.1278	
Residual	3.91E+09	11	3.56E+08			
Lack of Fit	2.15E+09	7	3.07E+08	0.70	0.6834	not significant
Pure Error	1.76E+09	4	4.41E+08			
Cor Total	2.08E+10	16				

The effect of two most significant factors, fly ash percentage and post-curing temperature, on the outer-shell elastic modulus is illustrated through a three-dimensional surface in Figure 4.11, which was derived from combined test results of the seventeen runs and the three additional runs. Depending on the curing temperature, the value of elastic modulus peaks when fly ash percentage is about 12% to 14%. The higher the curing temperature, the more fly ash can be added to achieve higher stiffness value.

Although post-curing time is not statistically significant in the analysis, it does have positive effect on the outer-shell elastic modulus. The elastic modulus of the outer-shell material increases with increase in post-curing time, as shown in Figure 4.12, and Figure 4.13. The elastic modulus increased by 4.7% and 4.1% when post-curing time is increased from 8 to 16 hr and from 16 to 24 hr, respectively.

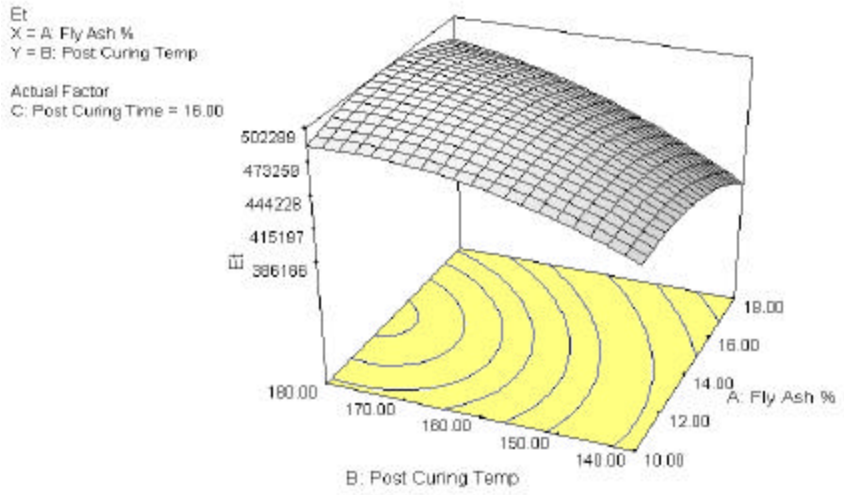

Figure 4.11 - Tangent elastic modulus vs. fly ash percentage and post-curing temperature

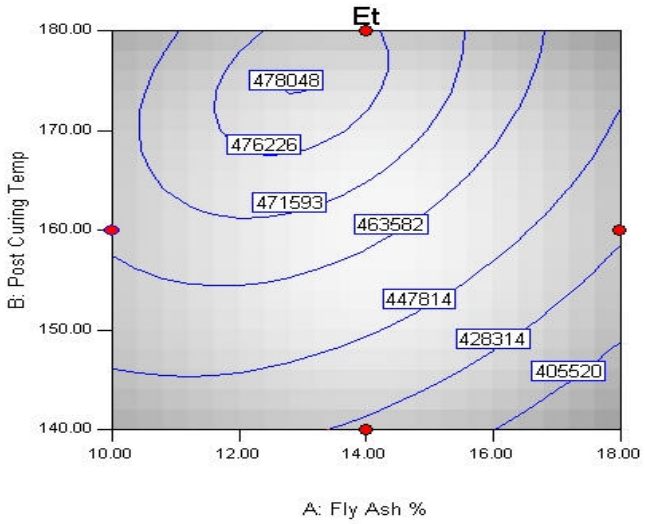

Figure 4.12 - Et vs. fly ash percentage and post-curing temperature after 16 hr post-curing

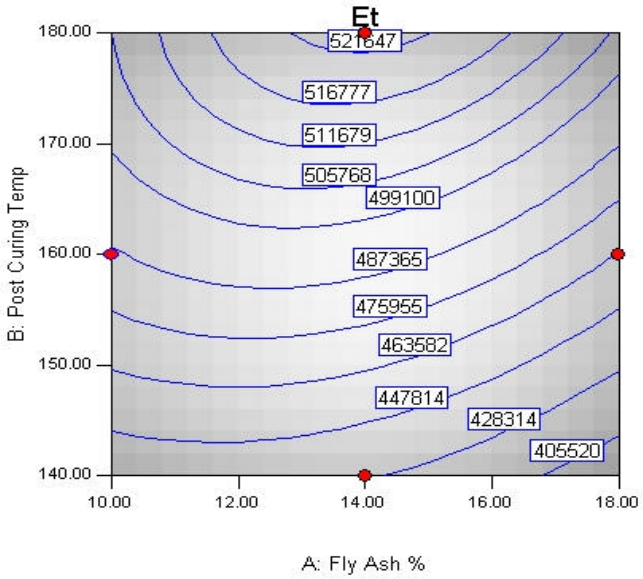

Figure 4.13 - Et vs. fly ash percentage and post-curing temperature after 24 hr post-curing

For gel time and peak exothermic temperature, the peak exothermic temperature (with 75 F^o ambient temperature) was approximately 200 F^o with a high of 211 F^o and a low of 181F^o. The average gel time was approximately 6.5 minutes, with a high of 7 min. 7 sec., and a low of 5 min. 46 sec. The three factors, fly ash percentage, curing temperature, and post-curing time did not have statistically significant effect on gel time or exothermic temperature.

Optimal material fabrication scheme:

The selection of the best material for fabrication of outer-shell is considered based on superior engineering properties and maximum utilization of fly ash. Figure 4.12 shows that the highest value of elastic modulus is achieved with 12% to 16% of fly ash and it varies depending on the curing temperature. With higher curing temperature, more fly ash can be added to the outer-shell material. In addition, it was found that longer post-curing time slightly increased elastic modulus of the outer-shell material. Based on these results, the best fabrication scheme for the outer-shell material identified was selected as 14% by weight fly ash, - 180 F^o curing temperature, and 24 hrs. post-curing time.

Effect of fly ash particle size and loading level:

It was hypothesized that cross-linking among polymer molecules around larger fly ash particles might be weaker than that around smaller particles. Micro-cracks may develop around larger size particles at lower stress levels. Therefore, it was thought that using finer fly ash should enhance engineering properties of a CCBs-based composite. This may also allow higher fly ash loading levels while maintaining the same engineering properties. An understanding of this hypothesis can be very advantageous for the CCBs-based composite utility pole design because larger addition of fly ash will decrease resin requirements and also cost of the engineered pole.

In this hypothesis testing, curing temperature and post-curing time were therefore fixed as 180 F^o and 24 hr, respectively. Primary emphasis of the study was to evaluate the effects of the particle size and percentage loading level of the fly ash. Three levels of

particle size and seven levels of fly ash percentage levels were selected. Three sets of fly ash were prepared by sieving the fly ash through US standard sieves (200 mesh, 325 mesh, and 400 mesh), and then the fly ash was mixed with polymer at different loading levels (0%, 5%, 10%, 15%, 20%, 25%, and 30%). Cylindrical samples (1.5 inch diameter and 3.0 inch height were used for testing. Utilization of the factorial design resulted in twenty-one (21) samples. Similar to the previous experimental design, each sample was replicated five (5) times. Thus, one hundred and five (105) cylindrical samples were prepared. Compressive tests on these samples were carried out as described previously.

The elastic modulus was calculated using linear regression experimental stress-strain data between 2000 and 3000 με. Estimated elastic modulus value was not accepted until its linear regression function had R^2 value larger than 0.98. The dimensions, elastic modulus and failure strength for each sample are listed in Tables 4.9 through 4.12.

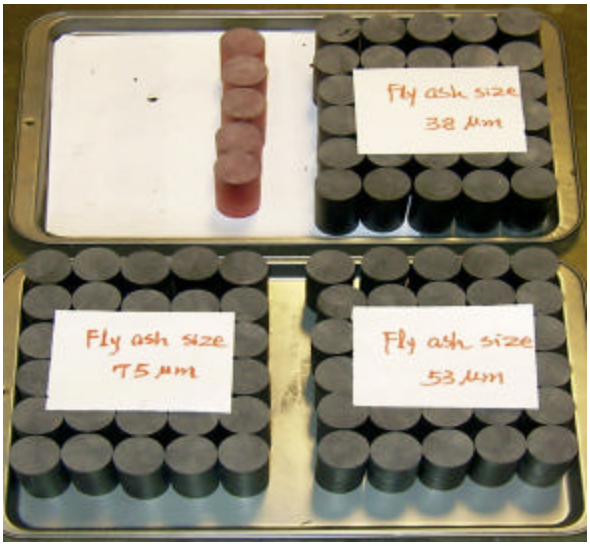

Figure 4.14 - Prepared ASTM samples for compression test

Table 4.13 lists the average values of the elastic modulus, failure strength, gel time, and viscosity. It was found that sieved fly ash did improve engineering properties of the CCBs-based composite. Elastic modulus and failure strength of sieved-fly-ash sample at each loading level are generally 10,000 – 50,000 psi and 3,000 – 5,000 psi higher than those containing as-received fly ash samples, respectively. Thus, removal of big particles from as–received fly ash was useful to develop a stronger and stiffer composite.

Table 4.9 - Compression test results for -75 microns CCBs-based composite material

Fly ash %	Sample #	Height, in	Diameter, in	E, psi	Strength, psi
0	a	2.758	1.565	447,948	15,805
	b	2.752	1.527	468,672	17,614
	c	3.087	1.524	479,152	17,351
	e	2.934	1.525	475,410	17,345
5	a	3.084	1.525	516,829	17,556
	b	3.077	1.529	516,282	17,432
	d	3.082	1.550	502,710	17,224
	e	3.086	1.525	499,849	17,522
10	a	3.021	1.534	505,272	17,246
	b	2.980	1.533	489,442	17,170
	c	3.100	1.532	530,131	17,166
	d	3.081	1.526	518,894	17,230
	e	3.169	1.535	537,100	17,077
15	a	3.188	1.542	562,245	17,326
	b	3.126	1.527	565,121	17,644
	c	3.077	1.531	502,238	17,061
	d	3.178	1.544	554,265	17,152
	e	3.211	1.538	538,748	17,010
20	a	3.216	1.534	592,911	17,724
	b	3.068	1.531	524,077	16,756
	c	3.032	1.537	554,163	16,085
	d	3.148	1.542	606,761	17,204
	e	3.206	1.529	598,518	17,228
25	a	3.074	1.536	607,725	17,810
	b	3.088	1.574	638,075	17,835
	c	3.101	1.541	640,717	18,025
	e	3.028	1.536	639,974	18,161
30	a	3.377	1.549	711,250	18,119
	c	3.224	1.538	655,422	18,739
	d	3.244	1.540	699,704	19,114
	e	3.127	1.532	710,243	19,135

Table 4.10 - Compression test results for -53 microns CCBs-based composite material

Fly ash %	Sample #	Height, in	Diameter, in	E, psi	Qu, psi
5	a	2.991	1.532	509,974	17,374
	b	3.113	1.542	527,360	17,160
	c	3.068	1.539	479,448	17,127
	d	3.042	1.556	504,862	17,139
	e	3.037	1.545	459,875	16,722
10	a	3.128	1.520	469,668	16,413
	b	3.166	1.531	500,603	16,616
	c	3.137	1.528	456,448	16,123
	d	3.145	1.522	487,115	16,684
	e	3.152	1.539	449,077	15,762
15	a	3.153	1.532	536,326	16,706
	b	3.120	1.529	515,069	16,543
	c	3.073	1.532	520,441	16,273
	d	3.138	1.533	500,307	16,068
	e	3.150	1.531	514,920	16,489
20	a	3.140	1.531	570,647	17,087
	b	3.064	1.534	562,491	17,034
	c	3.013	1.528	585,303	16,461
	d	3.165	1.534	502,603	16,232
	e	3.233	1.527	577,446	16,583
25	a	3.002	1.526	564,346	17,737
	b	3.205	1.547	551,330	17,095
	c	3.185	1.527	584,567	17,527
	d	3.208	1.538	520,799	16,506
	e	3.232	1.534	601,784	16,989
30	a	3.042	1.540	629,166	18,211
	b	3.128	1.533	576,299	17,967
	c	3.130	1.525	619,496	18,116
	d	3.132	1.530	644,769	18,572
	e	3.022	1.527	720,731	18,750

Table 4.11 - Compression test results for -38 microns CCBs-based composite material

Fly ash %	Sample #	Height, in	Diameter, in	E, psi	Qu, psi
5	a	3.002	1.525	503,437	16,859
	b	3.085	1.542	498,870	16,704
	c	3.025	1.535	497,240	16,708
	d	3.063	1.547	513,551	16,837
	e	3.074	1.524	469,915	16,884
10	a	3.076	1.527	540,702	17,117
	b	3.072	1.530	518,183	16,645
	c	3.021	1.531	570,399	16,852
	d	2.986	1.533	466,754	15,943
	e	2.987	1.523	481,204	16,791
15	a	3.091	1.545	537,259	16,671
	b	3.073	1.525	507,116	15,681
	c	2.982	1.534	528,255	17,084
	d	3.044	1.540	553,559	16,335
	e	3.072	1.525	497,244	15,802
20	a	3.014	1.531	579,468	17,166
	b	3.079	1.527	575,600	17,124
	c	2.861	1.528	502,855	17,243
	d	2.930	1.529	496,931	17,351
	e	3.026	1.527	546,243	16,782
25	a	3.125	1.522	628,119	18,633
	b	3.143	1.546	650,998	18,465
	c	3.106	1.536	611,331	17,484
	d	3.240	1.543	642,609	18,290
	e	3.039	1.535	682,335	18,244
30	a	3.180	1.536	616,214	18,113
	b	3.205	1.536	690,690	18,531
	c	3.043	1.535	650,360	17,023
	d	3.097	1.527	692,607	18,521
	e	3.066	1.527	694,250	18,327

Table 4.12 - Compression test results for as-received CCBs-based composite material

Fly ash %	Sample #	Height, in	Diameter, in	E, psi	Qu, psi
5	a	3.118	1.530	487,084	16,411
	b	3.142	1.530	495,627	16,186
	c	3.082	1.533	483,899	16,322
	d	3.122	1.537	437,200	16,417
	e	3.125	1.531	454,866	16,606
10	a	3.103	1.536	534,441	16,928
	b	3.238	1.532	501,067	16,972
	c	3.191	1.530	492,682	16,731
	d	3.008	1.531	517,579	16,833
	e	3.050	1.535	533,880	16,954
15	a	2.980	1.540	561,461	17,366
	b	N/A	N/A	N/A	N/A
	c	2.990	1.548	544,744	16,945
	d	2.940	1.542	556,003	16,981
	e	3.001	1.541	552,739	17,193
20	a	3.051	1.545	569,676	16,869
	b	3.009	1.549	563,072	16,695
	c	3.093	1.540	618,104	17,271
	d	3.007	1.543	601,868	17,012
	e	3.203	1.539	581,169	16,866
25	a	3.367	1.538	618,372	17,036
	b	3.315	1.540	606,993	17,621
	c	3.198	1.536	646,903	17,146
	d	3.348	1.544	625,311	17,152
	e	3.230	1.543	476,925	16,349
30	a	3.304	1.536	678,594	17,700
	b	3.298	1.536	677,464	17,700
	c	3.258	1.536	683,021	17,596
	d	3.238	1.531	674,347	17,526
	e	3.271	1.532	697,362	17,291

Table 4.13 - Effect of fly ash particle size and loading level on outer-shell properties

(1). Average Elastic Modulus, psi				
Fly ash %	75 micron	53 micron	38 micron	As-received
0	467,795	467,795	467,795	467,795
5	508,918	514,065	496,603	487,084
10	522,850	472,582	527,622	515,930
15	555,095	517,413	524,687	553,737
20	599,397	573,972	540,220	586,778
25	639,589	564,565	643,078	624,395
30	707,066	617,433	668,824	682,157
(2). Average failure Strength, psi				
Fly ash %	75 micron	53 micron	38 micron	As-received
0	17,029	17,029	17,029	17,029
5	17,434	17,224	16,798	16,381
10	17,180	16,320	16,851	16,905
15	17,283	16,416	16,315	17,121
20	17,385	16,791	17,133	16,943
25	17,958	17,171	18,223	17,239
30	18,777	18,217	18,103	17,563
(3). Gel time, seconds				
Fly ash %	75 micron	53 micron	38 micron	As-received
0	298	298	298	298.0
5	311	318	321	327.0
10	327	324	340	345.0
15	339	347	377	323.0
20	358	389	407	358.0
25	596	583	520	585.0
30	679	617	551	683.0
(4). **Viscosity of mixture, cPs**				
Fly ash %	75 micron	53 micron	38 micron	
0	1,630	1,630	1,630	
5	2,004	1,887	1,784	
10	2,680	2,479	2,374	
15	3,550	3,325	3,157	
20	4,650	4,415	4,283	
25	5,830	5,683	5,476	
30	7,180	7,013	6,873	

Another important result observed was the effect of the fly ash loading level on the elastic modulus of the composite. In previous studies, it was found that elastic modulus peaks around 10% - 15% ash loading level. Test results with more uniform size fly ash show that the elastic modulus of the composite increased with fly ash loading levels up to 30%, as shown in Figure 4.15. This is a positive finding because adding fly ash up to 30% (by weight) will decrease material cost by saving resin.

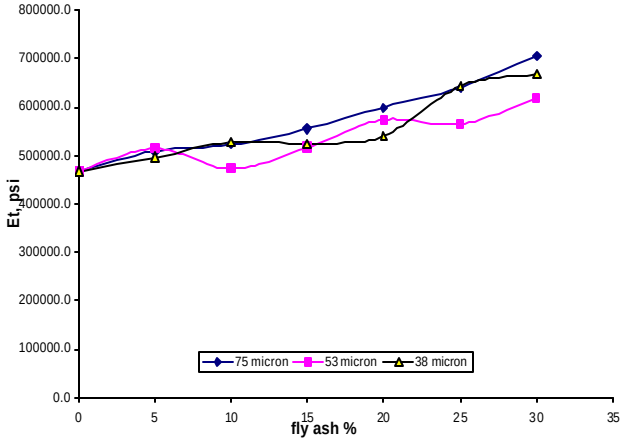

Figure 4.15 - Tangent elastic modulus vs. fly ash loading level

The gel time of the fly ash–polymer mixture increased with the increase in the fly ash loading level. The gel time increased significantly beyond 20% fly ash loading for all three types of samples, as shown in Figure 4.20. However, increase in gel time is much larger for large size particles in fly ash.

The viscosity of the fly ash-polymer mixture for all three types of sample also increases rapidly with the increase in fly ash loading level, as shown in Figure 4.17. Reducing particle size of the fly ash decreases viscosity of the mixture slightly.

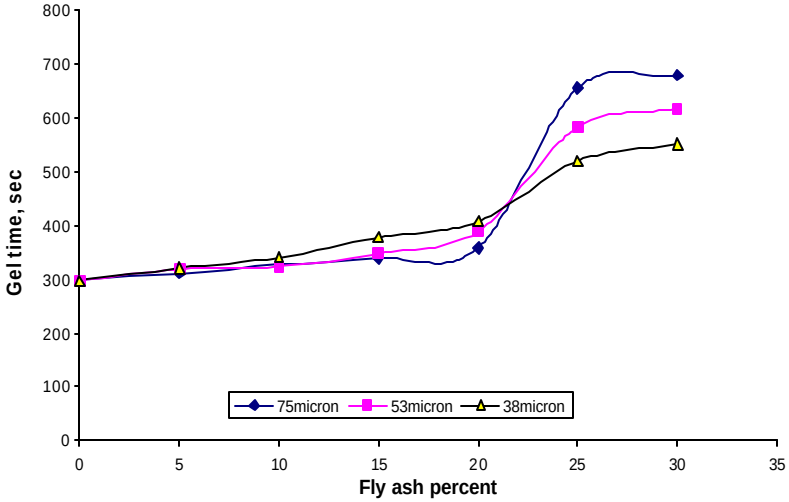

Figure 4.16 - Gel time of the fly ash-resin mixture vs. fly ash loading level

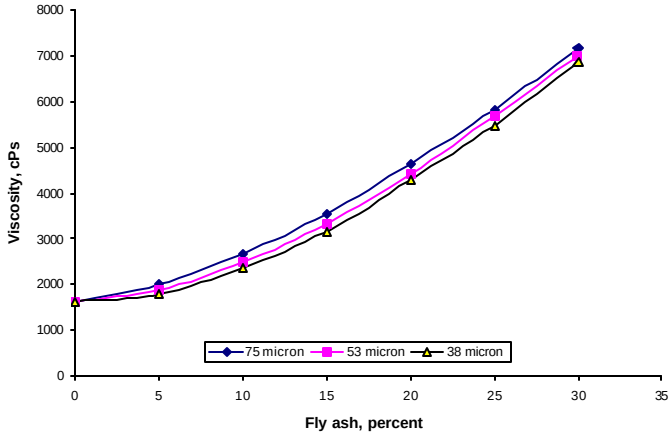

Figure 4.17 - Viscosity of the fly ash-resin mixture vs. fly ash loading level

4.5 Effect of type of the fly ash

Compared with SIUC-FBC fly ash, C-fly ash has uniform size distribution and spherical particle shape. Therefore, it was hypothesized that adding C-fly-ash from a local power plant might have a positive effect on enhancing engineering properties of the outer-shell material. To verify this hypothesis, studies were conducted to compare the engineering properties of the FBC-fly-ash-based composite and C-fly-ash-based composite for the outer-shell material. Samples of both kinds of fly ash were scanned first under an electron microscope for comparison. Figures 4.18 and 4.19 show the size distribution and particle shape of the both types of fly ash under different magnifications.

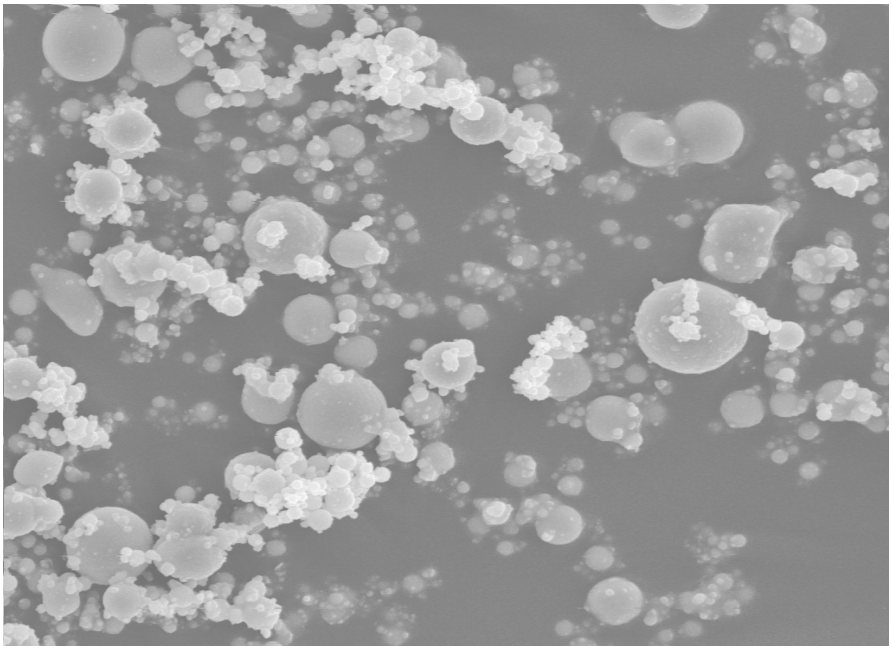

Figure 4.18 - C fly ash sample (X 1,000)

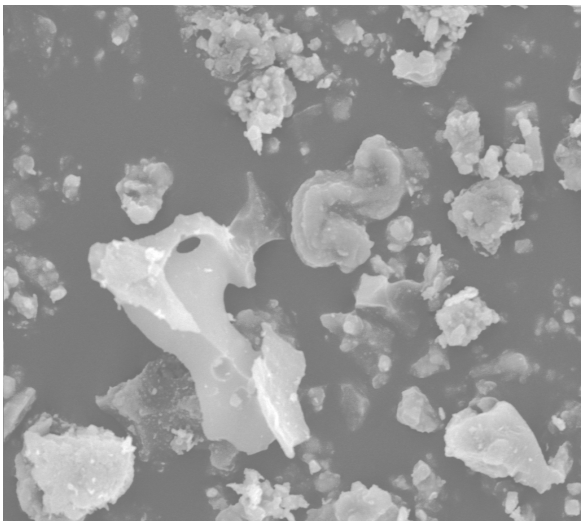

Figure 4.19 - FBC fly ash sample (X 1,000)

The particles of C fly ash are mostly spherical with more uniform size whereas the FBC fly ash has more irregular shape particles distributed over a wide size range. These physical properties may have a large effect on the engineering properties and viscosity of ash-resin mixtures. It was thought that with uniform size distribution and spherical particle shape, C fly ash would not decrease viscosity of polymer-ash mixture as much as FBC fly ash does. This will provide advantages in the design and implementation of the manufacturing facility for composite utility poles. However, this characteristic may have a negative effect on the stiffness and strength of final composite material. On the other hand, with irregular shape particles, FBC fly ash appears to have positive effect on enhancing material properties.

To verify the above hypothesis, unconfined compression tests were conducted on 2-inch cubes for FBC fly ash based and C-fly-ash-based composites to evaluate and to analyze the effect of fly ash type and fly ash loading percentage on composite material engineering properties.

Initial experiments were conducted to analyze the effect of fly ash type and fly ash loading on compressive strength, elastic modulus, gel time, pH value, and viscosity of the mixture with fly ash loading level varying 0%, 5%, 10%, 15%, and 20%.

Three samples were prepared for each fly ash percentage (0%, 5%, 10%, 15%, and 20%) for SIUC FBC fly ash and C fly ash. Thus, eighty-one specimens were prepared and tested. The test results of elastic modulus and failure strength for each fly ash percentage are listed in Table 4.14 and Table 4.15. Test results of the three specimens for each fly ash percentage and each group are very consistent. Figures 4.20 through 4.23 show the average value of elastic modulus and failure strength vs. fly ash loading percentage for both types of fly ash.

Table 4.14 - Unconfined compression test results FBC-based composite material

		Group 1		Group 2		Group 3	
FBC ash %		Et, psi	Qu, psi	Et, psi	Qu, psi	Et, psi	Qu, psi
0	a	348,881	12,192	262,411	11,123	348,881	12,192
	b	350,163	12,266	348,156	11,660	350,163	12,266
	c	344,662	12,033	315,923	11,427	344,662	12,033
5	a	391,537	12,850	371,695	11,882	391,537	12,850
	b	391,965	12,848	315,784	11,363	391,965	12,848
	c	396,064	12,836	354,238	11,859	396,064	12,836
10	a	358,866	11,344	376,496	12,363	358,866	11,344
	b	363,205	11,530	366,466	12,169	363,205	11,530
	c	369,628	11,519	405,637	13,095	369,628	11,519
15	a	464,810	14,414	502,246	14,974	464,810	14,414
	b	413,496	14,225	508,781	15,008	413,496	14,225
	c	421,640	14,273	433,767	14,535	421,640	14,273
20	a	539,262	15,476	552,170	15,856	539,262	15,476
	b	523,660	15,083	626,487	17,589	523,660	15,083
	c	542,000	15,407	534,704	14,782	542,000	15,407

Table 4.15 - Unconfined compression test results of C fly ash composite material

		Group 1		Group 2		Group 3	
C ash %		Et, psi	Qu, psi	Et, psi	Qu, psi	Et, psi	Qu, psi
0	a	348,881	12,192	262,411	11,123	454,695	15,038
	b	350,163	12,266	348,156	11,660	445,351	14,803
	c	344,662	12,033	315,923	11,427	429,849	15,070
5	a	237,488	8,480	252,811	8,835	266,439	8,949
	b	249,882	8,674	255,380	8,512	262,034	8,715
	c	258,261	8,802	235,886	8,761	187,035	8,820
10	a	182,421	9,336	318,573	9,933	221,961	9,655
	b	305,981	9,891	239,407	9,898	329,877	10,602
	c	297,938	9,958	259,384	10,247	324,660	10,562
15	a	302,923	10,067	307,869	10,362	319,075	10,258
	b	256,258	9,737	272,878	10,085	286,709	10,128
	c	341,796	10,246	264,772	9,696	264,928	10,099
20	a	360,884	11,017	237,483	10,331	189,696	7,166
	b	192,530	10,119	356,427	10,580	239,101	7,574
	c	291,732	10,309	371,283	10,632	244,249	7,696

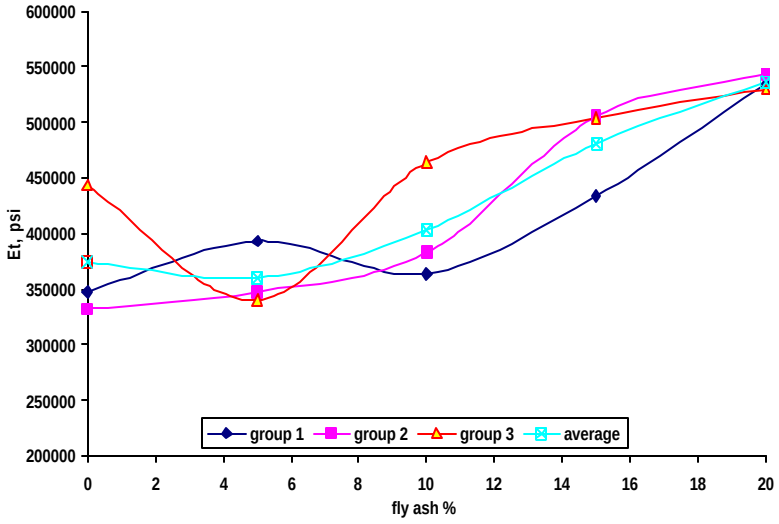

Figure 4.20 - Elastic modulus vs. fly ash % for FBC-fly-ash-based composite material

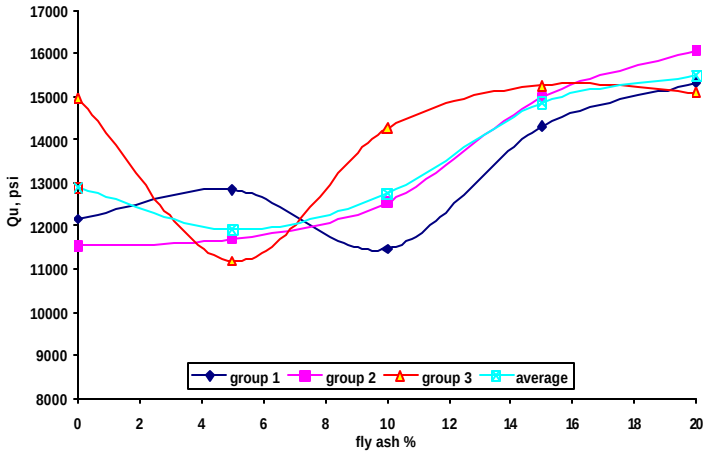

Figure 4.21 - Failure strength vs. fly ash % for FBC-fly-ash-based composite material

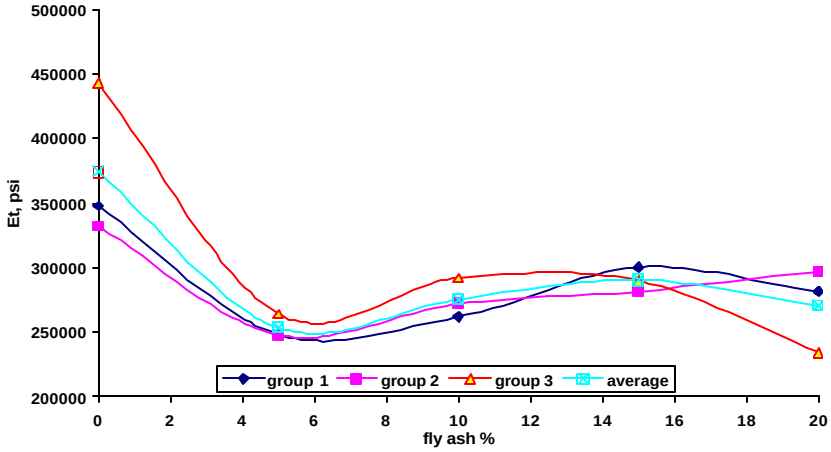

Figure 4.22 - Elastic modulus vs. fly ash % for C-fly-ash-based composite material

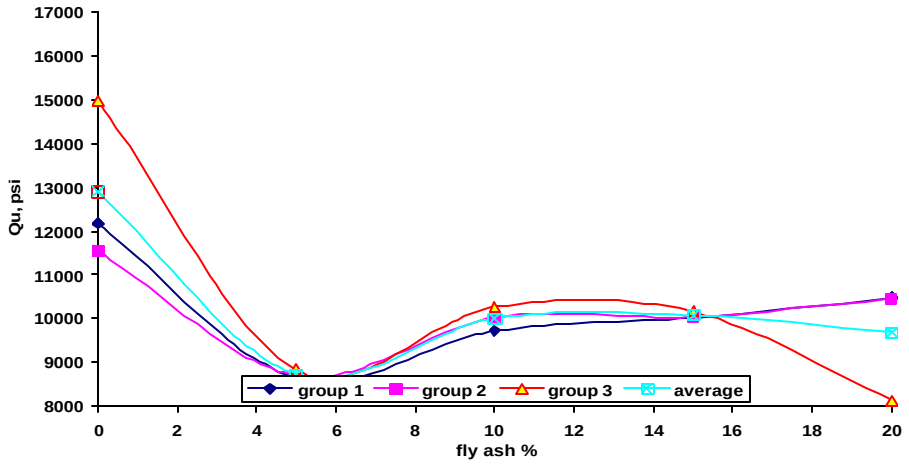

Figure 4.23 - Failure strength vs. fly ash % for C-fly-ash-based composite material

The results are summarized below.

(1). Addition of C fly ash into the outer-shell material did not improve material stiffness and strength. The elastic modulus and strength decreased by about 30% even with only 5% C fly ash addition. In addition, there is no trend that Et and Qu may increase as fly ash percentage increases.

(2). For FBC fly ash, the results agreed very well with the results obtained in the earlier studies. Adding FBC fly ash into outer-shell material increased material elastic modulus and strength by 5% to 65% depending on the fly ash percentage. The results revealed that adding fly ash up to 20% increased the strength and stiffness of the composite material. Since the viscosity of the resin-ash mixture is quite high at 20% fly ash loading, it was decided that the addition of fly ash will be limited to 15%. This should result in 30% increase in strength and stiffness of the final composite material as compared to resin-only composite material.

CHAPTER 5: DESIGN, MANUFACTURE, AND OPTIMIZATION OF THE COMPOSITE POLE

5.1 Introduction

Structural analyses were conducted to develop the design formulas for a cylindrical composite pole, which relates the various dimension parameters of the composite pole with structural bending stiffness of the wooden pole (section 5.1). Assuming structural bending stiffness same for the wooden and composite poles, various pole designs were developed with different combinations of outer diameter and shell thickness. To optimize the composite utility pole design, multi-objective optimization techniques were utilized with a consideration of material architecture, outer diameter, thickness, strength, and stiffness of the FRC pole.

5.2 Structural analysis

The basic concept of this analysis is to keep the product of the elastic modulus (E) and the moment of inertia (I) of the cross section the same for both wooden and composite poles and then compare their cost and weight. This would imply that the top deflection of the composite pole will be equivalent to that of the wooden pole for the same applied load. To achieve this goal, an equation was developed to determine the outer-shell thickness of composite pole based on the outer-shell radius and flexural stiffness of wooden pole (EI_{wood}).

The EI of the composite pole is given by the following equation,

$$(EI)_{Comp} = \frac{p}{4}[E_o(r^4 - (r-t)^4) + E_i(r-t)^4] \qquad \text{Equation (5.1)}$$

For EI of the composite pole equal to that of the wooden pole,

$$(EI)_{wood} = (EI)_{Comp} \qquad \text{Equation (5.2)}$$

Therefore, the equation (5.1) can be rewritten as,

$$t = r - \sqrt[4]{\frac{1}{(E_i - E_o)}\left[\frac{4(EI)_{wood}}{p} - E_i r^4\right]} \qquad \text{Equation (5.3)}$$

where, E: modulus of elasticity of wooden pole

I: Moment of inertia of the wooden pole

E_o: Modulus of elasticity of the outer-shell material

E_i: Modulus of elasticity of the inner-core material

r : Outer radius of the composite pole

t: Outer-shell thickness of the composite pole

Using different values of outer radius (r), series of values of shell thickness (t) and 2r/t were calculated. Only cylindrical poles without inner-core material were considered.

5.3 Candidate designs when the pole is unfilled

The structural strength and stiffness are basically governed by outer-shell material and inner-core material does not impact the pole design if hollow pole design is considered. Tables B.10, B.11, and B.12 in Appendix B list the EI ratio, weight ratio, and cost ratio of the hollow composite pole to wooden pole when elastic modulus is 3.5

million psi. Figure 5.1 summarize the data listed in these tables. Figure 5.2 shows the hollow pole design when the elastic modulus of the outer-shell is 3 million psi. and Figure 5.3 show the design parameters when the elastic modulus of the outer-shell is 2.5 million psi.

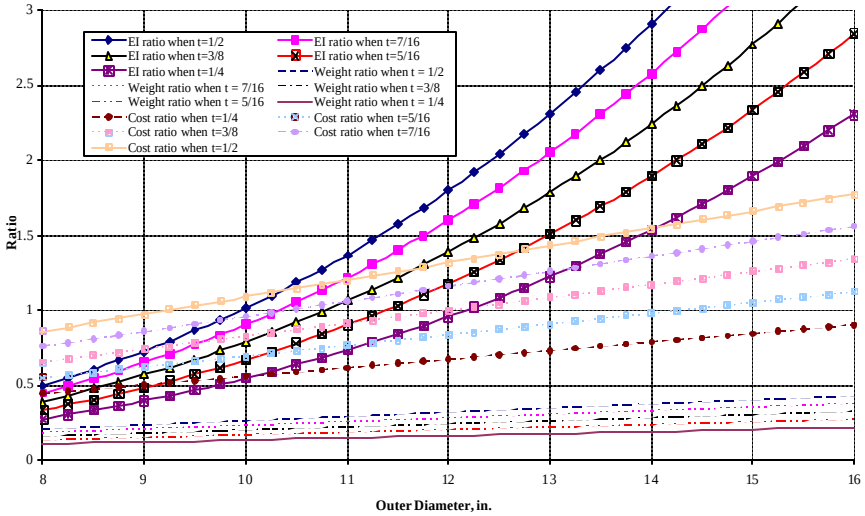

Figure 5.1 - Comparison of wooden pole and hollow pole when Eout=3.5 million psi

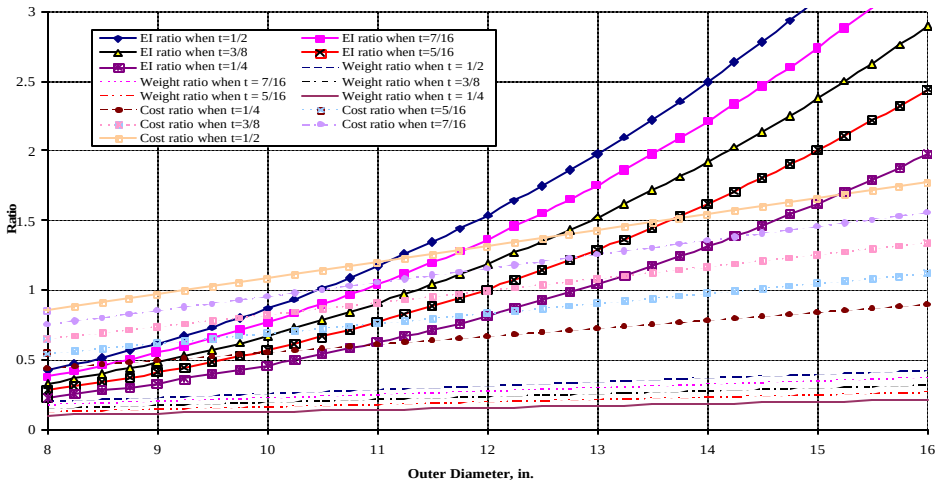

Figure 5.2 - Comparison of wooden pole and hollow pole when Eout=3 million psi

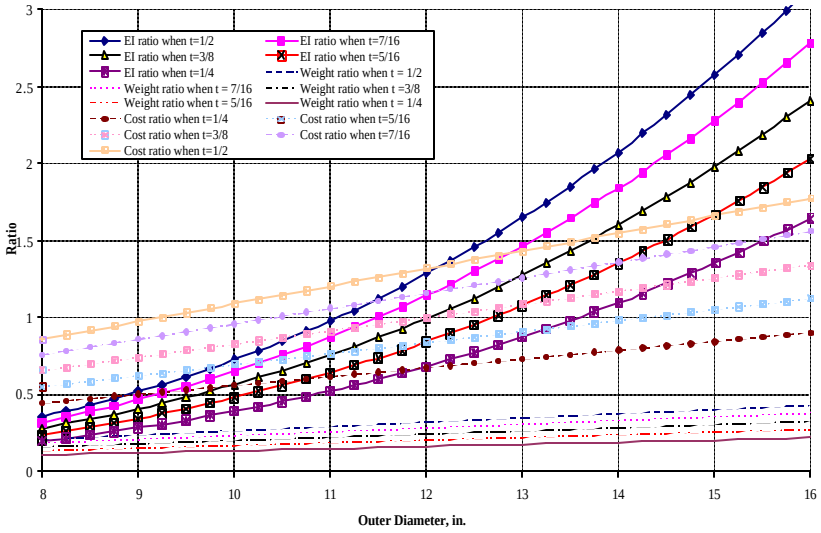

Figure 5.3 - Comparison of wooden pole and hollow pole when Eout = 2.5 million psi

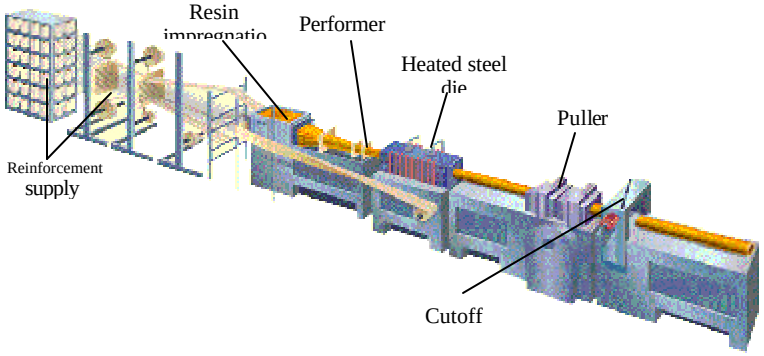

Figure 5.4 - Pultrusion process

Table 5.1 - Candidate design of the hollow class-4 composite utility pole

Outer-shell E (million psi)			3.5	3	2.5
Outer-shell thickness , in	7/8	Outer Dia.	8.75	9.25	9.75
		EI ratio	1.021	1.051	1.041
		Wt Ratio	0.38	0.41	0.43
	13/16	Outer Dia.	9	9.5	10
		EI ratio	1.063	1.087	1.07
		Wt Ratio	0.37	0.39	0.41
	3/4	Outer Dia	9	9.5	10
		EI ratio	1.002	1.024	1.007
		Wt Ratio	0.33	0.36	0.39
	11/16	Outer Dia	9.25	9.75	10.25
		EI ratio	1.025	1.041	1.018
		Wt Ratio	0.33	0.35	0.37
	5/8	Outer Dia	9.5	10	10.5
		EI ratio	1.036	1.046	1.018
		Wt Ratio	0.31	0.33	0.34
	9/16	Outer Dia	9.75	10.25	10.75
		EI ratio	1.033	1.038	1.005
		Wt Ratio	0.29	0.3	0.32
	1/2	Outer Dia	10	10.5	11.25
		EI ratio	1.014	1.014	1.049
		Wt Ratio	0.26	0.28	0.3
	7/16	Outer Dia	10.5	11	11.5
		EI ratio	1.054	1.045	1
		Wt Ratio	0.24	0.26	0.27
	3/8	Outer Dia	11	11.5	12.25
		EI ratio	1.063	1.046	1.059
		Wt Ratio	0.22	0.23	0.25
	5/16	Outer Dia	11.5	12	12.75
		EI ratio	1.033	1.01	1.014
		Wt Ratio	0.19	0.2	0.22
	1/4	Outer Dia	12.25	13	13.75
		EI ratio	1.02	1.048	1.037
		Wt Ratio	0.17	0.18	0.19

Table 5.2 summarizes the candidate design for the hollow composite utility poles. Removal of the inner-core material dramatically decreases the overall weight of the composite pole by 50%. Analysis shows that, when outer-shell has 3.5 million psi elastic modulus, the hollow pole design with 11 in. of outer diameter and 3/8 inch of wall thickness is comparable to class-4 wooden pole. In similar way, if E of the outer-shell is 3 million psi, then the hollow pole design with 11.5 in. outer diameter will be comparable. If E of the outer-shell is only 2.5 million psi, increasing the outer diameter of the pole to 12.25 in. will also make the composite pole comparable to wooden pole. The above results indicate that if elastic modulus is higher, the diameter of the pole can be decreased and the composite pole may be lighter. This decreases the volume of resin needed and total cost of the composite pole. The optimum pole design should be selected from these candidate designs based on obtainable outer-shell stiffness and comprehensive cost analysis of the pole.

5.4 Manufacturing of the CCBs-filled FRC model utility pole

Since proposed utility pole has a uniform cross-section. Pultrusion process was adopted in this study to manufacture the FRC pole. Pultrusion is a manufacturing process in which unidirectional filaments (fiber bundles or roving) with other fabric mats are impregnated with resin and pulled through a heated die to produce long prismatic structural components with a desired cross-section, as shown in Figure 5.4. The process has higher production efficiency.

As the glass passes through the wet-out bath and through the injection manifolds, it is completely saturated with a thermo-set resin that includes the CCBs fillers, catalyst, etc. As the glass enters the back of the die it is under high pressure, which forces out any air and excess resin from the reinforcement. Once inside the controlled heated die, the part passes through various stages of heat, which initiates catalyst systems to react within the laminate allowing the layers of reinforcements to be mechanically fixed to each other resulting in a solidified laminate exiting the die. Upon exiting the puller, the laminate passes through the final stage of a cut off saw where it is cut to its final length.

Figure 5.5 shows CCBs-filled FRC utility model pole that just comes out of pultrusion process, and Figure 5.6 shows 200 ft of final model pole produced. The wall thickness of the pultruded CCBs-filled composite outer-shell is about 0.24 inch with a relatively small number of reinforcement layers. Combinations of reinforcements, rovings and continuous strand mats (CSM), were used through the thickness of the final product, as shown in Figure 5.7.

Figure 5.5 - Pultrusion of the model composite utility pole

Figure 5.6 - Pultruded CCBs-filled FRC utility model poles

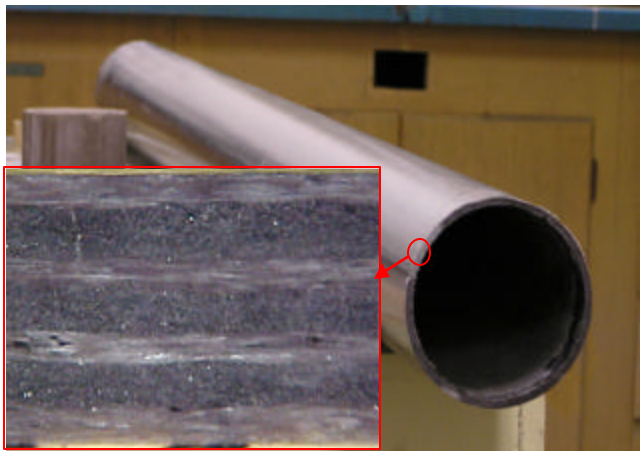

Figure 5.7 - Close view of the model pole and magnified cross-section

Roving is made up of fiberglass unidirectional filaments, which are manufactured in continuous rolls. Roving is present in pultruded composites and comprises about 60% of the total glass content. In addition to supplying the necessary strength to pull the profile, roving supplies the product with high tensile, and flexural strength properties and is a big contributor to the overall section stiffness.

The continuous strand mat (CSM) is the remainder of glass reinforcement used in the pultrusion process and represents about 40% of the total glass content. It consists of relatively long swirl fibers that are randomly oriented (in-plane). The CSM is designed specifically for the pultrusion process and offers good wet-out characteristics, conformability to a variety of shapes, and good physical properties including the required pull strength. It is used to obtain the desired engineering properties of the product in the transverse direction. Whereas the roving ties the composite together in the longitudinal direction, the mat is responsible for tying the composite together in all directions, but mainly in the transverse direction.

To improve the product's resistance to ultraviolet (UV) degradation and make the profile more user-friendly, synthetic veils were used to enhance the surface of pultruded profiles. The veil was added to the outside of a profile just prior to entry into the die. Since the veil brings more resin to the surface and the resin is the ingredient that provides corrosion resistance, adding the veil increases the corrosion resistance. The CCBs-filled FRC model poles were pultruded with a surface veil as well as UV inhibitors to protect the pole against UV degradation.

5.5 Optimization of the composite pole design

An attempt is made here to optimize the design of the CCBs-filled FRC utility pole. The primary objective of the study is to concurrently optimize the material architecture and cross-sectional area of the pultruded CCBs-filled FRC utility pole.

Material characterization of ply material:

Analysis and design optimization of the cylindrical shape FRC utility pole requires several material properties; primarily longitudinal and transverse elastic modulus and strengths and in-plane shear stiffness and strength for each layer. To find proper design variables, material architecture and laminate properties of the pultruded composite need to be developed. Although the pultruded FRC material is not a laminated structure in a rigorous sense, its material architecture can be simulated as such. As stated in the previous section, the pultruded CCBs-filled composite include the following three types of layers:

(1) Thin layers of randomly-oriented chopped fibers (Veil) placed on the surface of the composite. This is a resin-rich layer primarily used as a protective coating, and its contribution to the laminate response can be neglected;

(2) Continuous Strand Mats (CSM) layers which consist of relatively long, swirl fiber bundles that are randomly oriented in the plane of the mat. This system is used as a multi-directional secondary reinforcement system, which provides material continuity and strength in the transverse direction.

(3) Roving layers containing continuous unidirectional fiber bundles, which contribute the most to the stiffness and strength of a section.

The different forms of reinforcement are usually repeated several times throughout the thickness of the pultruded member. The CSM and roving systems can be idealized as layers with different thickness through the cross-section, depending on the level of reinforcement used. Figure 5.8 shows the veil, roving, and CSM layers in a failed tensile test sample.

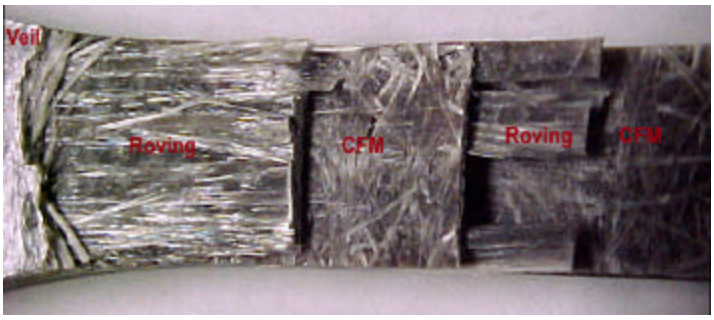

Figure 5.8 - Roving and CSM layers in a failed tension specimen

Figure 5.9 shows the polished cross-section throughout the thickness of the CCBs-filled pultruded composite material. It is clear that the CSM layer and roving layer are stacked alternatively. There are numbers of void systems inside the pultruded section as seen in Figure 5.12. The level of voids in pultruded composites has been previously studied and the void content in the pultruded profiles is about 3-5%. Denoting V as veil, C as continuous strand mat, and R as roving layer, the manufactured composite outer-shell consists of V/C/R/C/R/C/R/C/V.

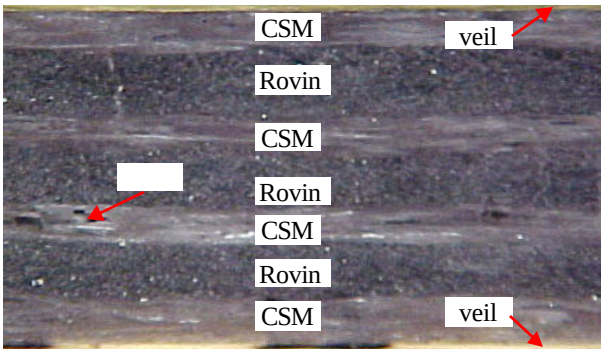

Figure 5.9 - Polished cross-section throughout the thickness of the composite material

The main concern is the design optimization of material architecture and dimensions of CCBs-filled FRC utility pole, which consists of E-glass fibers and polyester matrix. The material properties of the constituents (E-glass fiber and polyester matrix) are considered to be isotropic. The material architecture of CCBs-filled FR

outer-shell material includes sets of continuous strand mats (CSM), and roving (unidirectional fibers) arranged through the thickness of each panel. In the analysis, a symmetric lay-up is considered consisting of an idealized *(2m-1)* number of layers with *m* CSM layers and *m-1* roving layers, as shown in Figure 5.10.

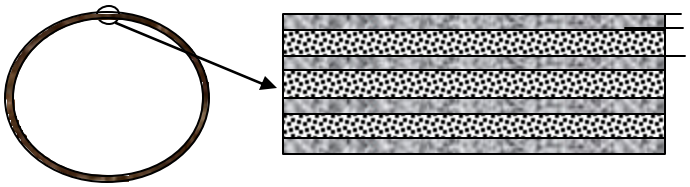

Figure 5.10 - Idealized lay-up system for pultruded composite outer-shell

The idealized layer thicknesses of CSM and roving layers are t_{CSM} and t_r and their corresponding FVFs [$(Vf)_{CSM}$ and $(Vf)r$] were evaluated using a series of burnout tests following the ASTM D2584 that describe the methods for ignition loss of cured reinforced resins.

Each layer is modeled as a homogeneous, linearly elastic, and generally orthotropic material. The ply materials used are specified as 0.229 kg/m^2 [3/4 oz/ft^2] CSM, and 227.6 m/kg [113 yield(yard/lb)] roving, which are commercially available and commonly used in pultruded FRC. The units used in this study are *oz* for CSM and *yield* for rovings, because these units are widely accepted in manufacturing and design. The ply thicknesses (t_{CSM}) and FVFs $(Vf)_{CSM}$ can be obtained based on the previous ASTM burnout test result. Their average values are found t_{CSM} = 0.025 inch and $(Vf)_{SF}$ = 36%. The total thickness of a CCBs-filled FRC panel, t, is defined as

$$t = nt_{csm} + (n-1)t_r \qquad \text{Equation (5.4)}$$

where for a given panel thickness t and CSM thickness t_{csm}, roving layer thickness can be computed from equation (5.4).

The design variables for material architecture are the lay-up number n and roving layer thickness t_r. By knowing n and t_r for a panel of a the panel thickness t and the fiber percentages of CSM and roving layers can be obtained.

Optimization objectives:

A particularly attractive advantage of FRP composites is the ability to tailor the material system along with the geometric shape for a given application. This advantageous characteristic of pultruded FRP composites can be achieved while overcoming the controlling constraints, such as deflection limit, material failure, and critical buckling load. An optimal combination of the factors like outer-shell thickness, outer diameter, number of ply, thickness of roving layer, and fiber volume fraction need to be analyzed and identified so that the developed composite pole will be comparable to class-4 wooden pole in terms of maximum stiffness and minimum weight. The task was to find the outer

diameter, outer-shell thickness, and material architecture (lay-up) of a composite circular thin-walled cylinder with specified applied bending moment, M, such that:

- the cross-sectional area, A, is minimized;
- total weight of the designed composite pole is less than that of a class-4 wooden pole;
- the maximum compressive stress in the cylindrical pole, N_{max} is smaller than the compressive strength, N_{cr}, of a uniaxially compressed cylinder, times a safety factor SF (knock-down factor);
- The maximum tensile stress in the pole outmost fiber is lower than its maximum tensile strength.
- The global bending stiffness, S, exceeds a minimum required stiffness, S_{req}. This guarantees the top deflection of the developed composite pole will not exceed the limit required by ANSI standard.

Problem formulation :

The optimal design of the CCBs-filled pultruded FRC cylindrical utility pole can be considered as a standard problem of finding a design variable vector *b* that will minimize an objective function *F(b)* subjected to equality constraints, $G_i(b) = 0$ *(i = i to p)*, and inequality constraints, $G_i(b) \le 0$ *(i = (p+1) to m)*, and with explicit lower and upper bounds on the design variables given as $b_{il} \le b_i \le b_{iu}$, for *i = 1 to n*.

The global bending stiffness of a cylindrical composite utility pole can be calculated using Euler-Bernoulli beam theory (James, 1990), which is related to moment of inertia and cross sectional area. The cross-sectional area of a thin-walled cylinder is:

$$A = p\,(D - t)t \qquad \text{Equation (5.5)}$$

where D is outer diameter of the cylindrical shell, and t is the average shell thickness.

Second area moment of inertia (I) is:

$$I = p\,\frac{(D-t)^3}{8}t \qquad \text{Equation (5.6)}$$

Average flexural modulus in axial direction is:

$$E_{xx} = \frac{12(D_{11}D_{22} - D_{12}^{\,2})}{t^3 D_{22}} \qquad \text{Equation (5.7)}$$

Average flexural modulus in the circumferential direction is:

$$E_{yy} = \frac{12(D_{11}D_{22} - D_{12}^{\,2})}{t^3 D_{11}} \qquad \text{Equation (5.8)}$$

Average shear modulus is:

$$G_{xy} = \frac{12D_{66}}{t^3} \qquad \text{Equation (5.9)}$$

Poisson's ratio is:

$$m_{xy} = \frac{D_{12}}{D_{22}} \qquad \text{Equation (5.10)}$$

For a cylindrical utility pole that is subject to bending loads, it's bending stiffness, S, is:

$$S = E_{xx}I = \frac{12(D_{11}D_{22} - D_{12}^{\ 2})}{t^3 D_{22}} p \frac{(D-t)^3}{8} t \qquad \text{Equation (5.11)}$$

where D_{ij} is component of the [D] matrix computed based on the classical plate theory, as given in (7.30) in Chapter 7.

The cross-sectional area of the cylindrical composite pole is closely related to engineering properties of the reinforcements which are to be maximized. It also represents the structural weight which is to be minimized under buckling and stiffness constraints. In mathematical terms the optimization problem can be expressed as:

$$\text{Minimize } A = p[D - (nt_{csm} + (n-1)t_r)](nt_{csm} + (n-1)t_r)$$

$$\text{Maximize } S = [D_{11} - (D_{12}^2 / D_{22})]p \frac{3(D-t)}{2t^2}$$

$$\text{Minimize } N_{max} = \frac{4MD}{p(D-t)^3 t}$$

$$\text{Minimize } T_{max} = \frac{4MD}{p(D-t)^3 t} \qquad \text{Equation (5.12)}$$

Given the following constraints:

$$2 \le n \le 7$$

$$0.02 \text{ inch} \le t_r \le 0.2 \text{ inch}$$

$$8 \text{ inch} \le t \le 16 \text{ inch}$$

$$S = S_{req}$$

$$N_{max} = Ncr/SF$$

$$T_{max} = N_{tr}/SF$$

$$W_t = A\ L\ ?_{avg} = 1100 \text{ lb} \qquad \text{Equation (5.13)}$$

where, t is the outer-shell thickness, $t = nt_{csm} + (n-1)t_r$, based on actual manufacturing process, assume $t_r = 2\ tc_{sm}$;

n is the number of CSM layers;

D is the outer diameter of the cylindrical composite utility pole, 8 inch $\le t_r \le$ 16 inch based on preliminary design;

L is the length of the pole, 35 ft;

M is the bending moment applied to the pole. M = 2400 *35 =84,000 lb*ft

$?_{avg}$ is average density of CCBs-filled FRC, $?_{avg}$=80 pcf;

S_{req} is the required bending stiffness of the utility pole. The equivalent bending stiffness value (5.825E+08 lb*in^2) of class-4 wooden pole was applied here;

SF: design safety factor, SF = 1.5.

N_{cr} and N_{tr}: Compressive and tensile strength of the outer-shell, N_{cr} = 55,000 psi and N_{tr} = 45,000 psi

D_{ij} is the component determined from equation (7.30).

Optimal composite pole designs:

In this study, the multiple objective functions in equation (5.13) represent the outer-shell cross sectional area (A), flexural bending stiffness of the pole (S), maximum compression stress (N_{max}) and maximum tensile stress (T_{max}) that occurs on the outer-shell material when the full length composite pole is subjected to 2,400 lb horizontal load in cantilever bending mode. The constraint functions in equation (5.13) are the upper and/or lower bounds of the design variables, and involve inequalities.

The minimization or maximization of the objective functions can be accomplished with available constraint functions. However, the evaluation of the objective functions for the deflections, micro-mechanics analysis, macro-mechanics analysis, and failure analysis can be a difficult problem. It would be a time-consuming effort if a traditional mathematical optimization technique was adopted because the objective functions and their constraint functions involve compounded, nonlinear, and inexplicit calculation. Thus, to solve the optimization problem without going through complicated mathematical manipulations, the objective functions were explicitly expressed in terms of design variables and were evaluated for a number of design points. It is important to mention that the flexural bending stiffness (S) in this step is very hard to express explicitly as a function of design variables because its computation involves complicated micro-mechanics analysis, micro-mechanics analysis, and classical plate theory. To overcome this difficulty computer programs were developed using MathCAD to calculate the [D] matrix for given material architecture variables (number of lamina, layer thickness, overlay pattern, roving fiber orientation, fiber volume fraction, etc). The [D] matrix was then used to calculate laminate bending stiffness.

The design variables are number of laminas (2n-1, n is number of CSM), roving layer thickness (t_r), CSM layer thickness (t_{csm}), and diameter of outer-shell (D). In the calculations, the number of CSM lamina were considered as 2, 3, 4, 5, 6, and 7 as limited by constraints. To provide multi-directional secondary reinforcement system for the composite and maximize material continuity and strength in transverse direction, the outer most laminas are all CSM. Since the CSM and roving lamina are laid alternately, the number of roving lamina is 1, 2, 3, 4, 5, and 6 corresponding to the number of the CSM lamina. Thus, the total number of laminas in the composite is 3, 5, 7, 9, 11, and 13, respectively. For each lamina lay-up pattern, the thickness of the roving lamina was increased from 0.02 inch to 0.2 inch by increments of 0.01 inch. AS a common practice of actual pultrusion process, the thickness of CSM layer in this analysis is assumed as one-half of that of the roving lamina. From the preliminary pole design stated in section 5.2, the design space of the outer-shell diameter (D) for the composite pole was considered in the range of 8 inch to 16 inch. In the optimization calculations, the value of D was increased from 8 inch to 16 inch in increment of 0.25 inch.

Optimization results when the pole is hollow:

For given number of laminas, roving lamina thickness, CSM lamina thickness, and outer-shell thickness, increasing the outer diameter will increase total weight, structural bending stiffness, and outer-shell cross-sectional area of the pole, and it will also decrease the maximum stress in the outer-shell composite. Table 5.3 lists the value variation of the objective functions with increase in the outer diameter when the number of laminas is 5, roving lamina thickness is 0.05 inch, CSM lamina thickness is 0.025, and

shell thickness is 0.175 in. By applying other constraints (maximum stress, flexural bending stiffness), it is clear the last design in Table 5.3 that can satisfy the design requirements. In other words, a composite pole with 5 laminas (3 CSM of 0.025 inch, and 2 roving layer of 0.05 inch), a total 0.175 in shell thickness, and 16 in outer diameter will be comparable to a class-4 wooden pole. In this case, the engineered pole will not fail for 2,400 lb horizontal load applied at the pole top, and will be 85% lighter and 55% stronger that the wooden pole.

Table 5.2 - Variation of objective function values with the outer diameter

D, in	Total weight, lb	Sigma max, psi	flexural stiffness, S, lb*in^2	Cross sectional area A, ft^2
8	83.7	122,453	1.09E+08	0.0299
8.5	89.0	108,043	1.32E+08	0.0318
8.75	91.7	101,774	1.44E+08	0.0327
9	94.3	96,035	1.57E+08	0.0337
9.25	97.0	90,768	1.70E+08	0.0346
9.5	99.7	85,923	1.85E+08	0.0356
9.75	102.4	81,456	2.00E+08	0.0366
10	105.0	77,328	2.16E+08	0.0375
10.25	107.7	73,506	2.33E+08	0.0385
10.5	110.4	69,960	2.51E+08	0.0394
10.75	113.1	66,665	2.70E+08	0.0404
11	115.7	63,598	2.89E+08	0.0413
11.25	118.4	60,737	3.10E+08	0.0423
11.5	121.1	58,065	3.31E+08	0.0432
11.75	123.7	55,566	3.54E+08	0.0442
12	126.4	53,224	3.77E+08	0.0451
12.25	129.1	51,028	4.01E+08	0.0461
12.5	131.8	48,965	4.27E+08	0.0471
12.75	134.4	47,024	4.53E+08	0.048
13	137.1	45,196	4.81E+08	0.049
13.25	139.8	43,473	5.10E+08	0.0499
13.5	142.5	41,847	5.39E+08	0.0509
13.75	145.1	40,310	5.70E+08	0.0518
14	147.8	38,857	6.03E+08	0.0528
14.25	150.5	37,480	6.36E+08	0.0537
14.5	153.1	36,176	6.70E+08	0.0547
14.75	155.8	34,938	7.06E+08	0.0556
15	158.5	33,763	7.43E+08	0.0566
15.25	161.2	32,646	7.81E+08	0.0576
15.5	163.8	31,584	8.21E+08	0.0585
15.75	166.5	30,572	8.62E+08	0.0595
16	169.2	29,609	9.04E+08	0.0604

Following a similar approach, feasible designs of the hollow engineered composite poles for all possible combinations of the design variables were identified. An examination of these feasible designs revealed that the increase in the number of laminas, lamina thickness, and outer-shell thickness increased structural bending stiffness, overall weight, and shell cross sectional area, and decreased maximum stress. With minimum overall pole weight and shell cross sectional area as the optimization criteria, the promising designs of the hollow composite pole were narrowed down to the following designs (Table 5.4).

Table 5.3 - Promising designs for the hollow composite utility pole

No. of laminas	t_r, in	t_csm, in	t, in	D, in	Weight, lb	s_{max}, psi	S, lb*in^2	A_shell, ft^2
3	0.09	0.045	0.18	15.75	171.20	29751.77	6.93E+08	0.0611
5	0.05	0.025	0.175	16	169.17	29608.84	9.04E+08	0.0604
7	0.05	0.025	0.25	13.5	202.35	29793.17	8.23E+08	0.0723
9	0.04	0.02	0.26	13.25	206.31	29839.10	8.41E+08	0.0737
11	0.04	0.02	0.32	12.25	233.20	28935.80	8.22E+08	0.0833
13	0.03	0.015	0.285	12.75	217.01	29645.52	8.48E+08	0.0775

Apparently, the second design in Table 5.4 is the best one. While guaranteeing enough material strength, it provides the highest flexural bending stiffness with minimal overall weight and shell cross-sectional area. This means that a hollow composite utility pole with 0.175 in shell thickness and 16 inch outer diameter composite pole can be 55% stronger and 85% lighter than a wooden pole if its outer-shell is made of 5 layers of lamina (3 CSM layer of 0.025 in and 2 roving lamina of 0.05 in).

Considering material architecture (number of laminas, layer lay-up pattern, lamina thickness), outer diameter, shell thickness, material strength, structural bending stiffness, multi-objective optimization techniques were utilized to optimize the composite utility pole design. It was found that, when the composite pole is hollow, the optimal design is a cylindrical hollow composite pole with 0.175 in shell thickness and 16 inch outer diameter composite pole, which will be 55% stronger and 85% lighter than a wooden pole if its outer-shell is made of 5 layers of lamina (3 CSM layer of 0.025 in and 2 roving lamina of 0.05 in). When the pole is filled up with inner-core material, the optimal design is a cylindrical composite pole with 0.3 in shell thickness and 12.5 inch outer diameter, which will be 37% stronger and 2% lighter than a wooden pole if its outer-shell is made of 7 layers of lamina (4 CSM layer of 0.06 in and 2 roving lamina of 0.03 in).

CHAPTER 6: MICRO-MECHANICS ANALYSES

6.1. Introduction

Micro-mechanics is the study of composite materials taking into account the interaction of the constituents. It is used to predict stiffness and strength of a FRC material. Micro-mechanics allows the designer to represent a heterogeneous material as an equivalent homogeneous anisotropic material. A CCBs-filled FRC material is basically a composite laminate, which consists of multiple roving layers and continuous strand mat (CSM) layers. This chapter discusses the prediction of the effective stiffness and strength of the both layers through micromechanical analysis approach. The in-situ material properties for the fiber and the matrix are assumed to have the same values in both CSM and roving layers. Fiber volume fraction (FVF) of individual layers is determined by the burnout test (ASTM2584). The micromechanical and mechanics of materials approaches were then utilized to evaluate and determine the stiffness and material properties of the roving layers and CSM layers.

6.2 Determination of fiber volume fraction through the ASTM burnout test

Micro-mechanics and macro-mechanics analyses on a composite material require material specifications, such as fiberglass and resin type, reinforcement pattern, fiberglass mass and volume ratio. However, much of this information was not provided by the manufacturer, since it is considered confidential. Therefore, efforts were made to conduct material mass and volume fraction tests in the laboratory following the Standard Method for Ignition Loss of Cured Reinforced Resins and a procedure for determining the volume fraction of glass in FRP composites (ASTM D2584). The experiment was conducted under the assumption that the resin of the composite is organic and will be decomposed to volatile matter. Ignoring small amounts of other volatiles (water, resin solvent), the ignition loss was considered as the resin content of the sample.

The test specimens were cut from the developed test panel and processed as close in size to the ASTM standards as possible (1 inch by 1 inch by 0.24 inch). The specimens were put into an oven to be dried at 140 F^o for 24 hours and cooled to ambient temperature in desiccators. After measuring the initial dried mass, the specimens were put into crucibles and were burned until fiber, CCBs, and carbon formed the residue. The residue was then placed in a furnace and degraded, leaving only reinforcement and CCBs. Figure 6.1 shows the burnout test samples taken out of furnace.

Figure 6.1 - Burnout test samples

After the resin was burnt, analysis of the laminate was performed on the burnout remains. The post-burnout mass of specimens was measured after the samples were cooled to ambient temperature. Then the specimens were carefully disassembled and roving lamina residue and CSM residue were separated from each other.

With the measured mass of each residue, calculations were conducted to determine the FVF within roving lamina and CSM lamina. In this calculation, the resin and CCBs filler were assumed to be distributed uniformly throughout the material thickness. In order to determine the thickness fraction of the layers, the relative thickness of the roving (0.1411/0.2378) and CSM layers (0.0967/0.2378) were first determined using an optical microscope, shown in Figure 6.2. Unit weight of fiberglass, resin, and CCBs filler were measured as 158.6 pcf, 78 pcf, and 104.8 pcf, respectively.

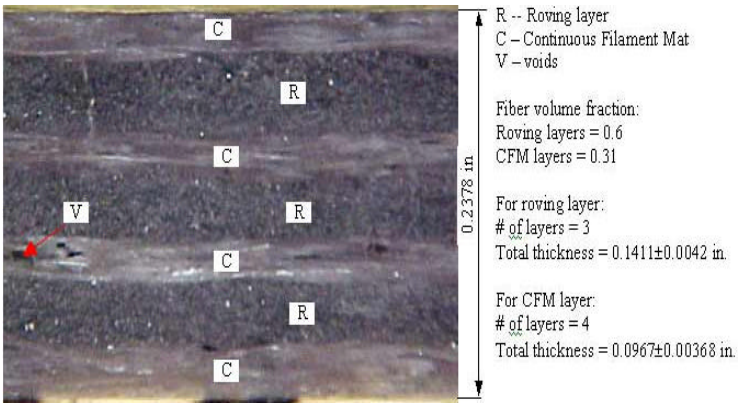

Figure 6.2 - Polished cross-section of the CCBs-filled composite

Table 6.1 shows the FVF results of the burnout tests for ten specimens. The FVF of the roving layer is found to be about 45.35% for both fly ash percentages. The FVF of CSM layers is 38% in the 5% fly ash sample and 35.7% in the 10% fly ash sample.

Table 6.1 - FVF of CCBs-based composite via burnout test results

Fly ash %	Sample #	Ms	Ma	Mar	Mac	Mr	Mf	Mrr	Mrc	Mfr	Mfc	Mgr	Mgc	Vsr	Vsc	FVFr	FVFc
		g	g	g	g	G	g	g	g	G	g	g	g	cm^3	cm^3	%	%
5	1	6.60	4.001	2.718	1.283	2.6	0.13	1.54	1.058	0.077	0.053	2.64	1.23	2.32	1.36	44.8	35.5
	2	6.52	3.977	2.655	1.322	2.54	0.13	1.51	1.032	0.075	0.052	2.58	1.27	2.27	1.36	44.8	36.9
	3	7.73	4.91	3.105	1.805	2.82	0.14	1.67	1.146	0.084	0.057	3.02	1.75	2.58	1.64	46.2	42
	4	6.84	4.267	2.873	1.394	2.57	0.13	1.53	1.046	0.076	0.052	2.8	1.34	2.37	1.4	46.5	37.8
	5	6.70	4.073	2.681	1.392	2.63	0.13	1.56	1.069	0.078	0.053	2.6	1.34	2.32	1.41	44.2	37.3
Average																45.3	37.9
Std Dev.																0.98	2.43
10	1	6.77	4.25	2.884	1.342	2.52	0.25	1.5	1.026	0.15	0.103	2.73	1.24	2.36	1.37	45.6	35.6
	2	6.59	4.096	2.832	1.277	2.49	0.25	1.48	1.013	0.148	0.101	2.68	1.18	2.33	1.33	45.4	34.7
	3	6.58	4.144	2.805	1.32	2.43	0.24	1.44	0.99	0.144	0.099	2.66	1.22	2.29	1.33	45.8	36.1
	4	6.41	4.013	2.701	1.275	2.39	0.24	1.42	0.974	0.142	0.097	2.56	1.18	2.23	1.3	45.2	35.7
	5	6.24	3.928	2.611	1.259	2.31	0.23	1.37	0.938	0.137	0.094	2.47	1.17	2.15	1.27	45.3	36.3
Average																45.4	35.7
Std Dev.																0.22	0.6

Ms: mass of dried sample before test; Ma: mass of residue after test ;

Mar: mass of roving residue after test; Mac: mass of CSM residue after test;

Mr: Mass of resin; Mf: Mass of CCBs filler;

Mrr: Mass of resin in roving lamina; Mrc: Mass of resin in CSM lamina

Mfr: Mass of filler in roving lamina; Mfc: Mass of filler in CSM lamina;

Mgr: mass of glass in roving lamina; Mgc: Mass of glass in CSM lamina

Vsr: Sample volume related to roving lamina; Vsc: Sample volume related to CSM lamina;

FVFr: FVF of roving lamina; FVFc: FVF of CSM lamina

Unit conversion factor: 1 gram = 0.0022046 pound; 1 cubic centimeter = 0.0610237 cubic inch

6.3 Micro-mechanics analysis of the lamina

The CCBs-based FRP composite consists of CCBs-mixed polymer reinforced with alternating layers of unidirectional E-glass roving and CSMs. Three layers of fiber roving and four layers of CSM stack one on another in an alternating pattern as shown in Figure 6.2 and Figure 6.3. Denoting R as roving and C as CSM, the material architecture of the laminated composition can be coded as [C/R/C/R/C/R/C]. The in-situ fiber and matrix properties were estimated through published approaches and are reported in Table 6.2.

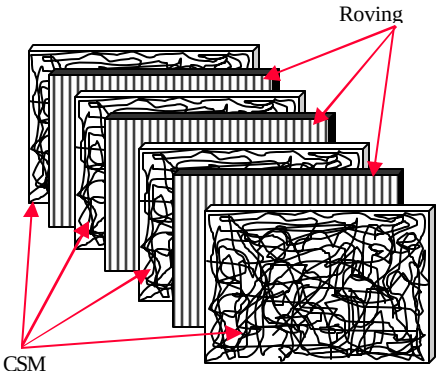

Figure 6.3 - Material architecture of CCBs-based FRP composite

Table 6.2 - Properties of fiber and matrix

	E (ksi)	?	γ
E-glass fiber	10500	0.2	2.54
Matrix	493	0.3	1.25
CCBs	N.A.	N.A.	1.68
E: Young's modulus; μ: Poisson's ratio; γ: Specific gravity			

The interaction of the constituent materials (micro-mechanics) is essential to the understanding of the macro-mechanics of the laminated composite. Micro-mechanics helps to predict the lamina properties, which can be used for laminate analysis. Micro-mechanics is a natural adjunct to macro-mechanics when viewed from design rather than analysis point of view. Two related approaches, rule of mixture and the mechanics of material, are used in this study for the determination of the stiffness and other engineering properties for the roving layer and CSM layer.

Roving layer: Figure 6.4 illustrates schematic material architecture of a roving layer.

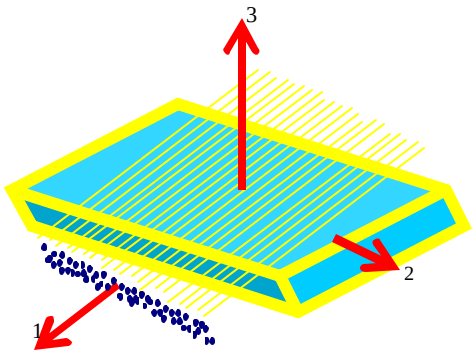

Figure 6.4 - Schematic illustration of material architecture of roving layer

Stiffness: Both fibers and matrix are assumed to be isotropic. Their stiffness can be completely represented by two engineering properties: the modulus of elasticity E and Poisson's ratio μ, as listed in Table 6.2. From a micro-mechanics point of view, the CCBs-filled fiber reinforced roving layer is basically a combination of the three isotropic materials (fiber, CCBs, and matrix). It can be represented as an equivalent, homogeneous, transversely isotropic material, the stiffness of which can be described by five elastic properties:

- E_1: modulus of elasticity in fiber direction, psi;
- E_2: modulus of elasticity in the direction perpendicular to fibers, psi;
- G12: in-plane shear modulus, psi;
- G23: out-of-plane shear modulus, psi;
- m_{12}: in-plane Poisson's ratio.

The above properties are functions of fiber volume fraction, fiber engineering properties, and matrix engineering properties. Prediction of these parameters based on constituent material properties and FVF are discussed below:

The longitudinal modulus, or modulus in the direction of the fiber direction (E_1), can be predicted very well by the rule of mixture (ROM) formula. The main assumption of the formulation is that the strains in the fiber direction of the roving layer are the same in the fiber as in the matrix. This assumption leads to the formula below,

$$E_1 = E_f V_f + E_m (1 - V_f) \qquad \text{Equation (6.1)}$$

where, E_f is the modulus of elasticity for fiber,

E_m is the modulus of elasticity for matrix, and

V_f is the fiber volume fraction;

Determination of the modulus in the direction transverse to the fiber (E_2) can be predicted using inverse ROM, which can be derived based on the assumption that the stress is the same in the fiber and the matrix. This leads to the inverse ROM, as given by,

$$\frac{1}{E_1} = \frac{1-V_f}{E_m} + \frac{V_f}{E_f} \qquad \text{Equation (6.2)}$$

The above prediction provides lower bound, and is not accurate in the majority of cases. A better prediction is obtained using the semi empirical Halpin-Tsai formula (Halpin, Tsai, 1969),

$$E_2 = E_m[\frac{1+x\,hV_f}{1-hV_f}]$$
$$h = \frac{(E_f / E_m)-1}{(E_f / E_m)+x} \qquad \text{Equation (6.3)}$$

where x is an empirical parameter. The value of x =2 usually gives a good fit for the cases of circular or square fibers.

The in-plane Poisson's ratio m_{12} by definition is the ratio of the resulting strain in transverse direction to the applied strain in longitudinal direction. The mechanics of material approach leads to a ROM equation,

$$m_{12} = m_f V_f + m_m(1-V_f) \qquad \text{Equation (6.4)}$$

where, m_f is the Poisson's ratio for fibers, and

m_m is the Poisson's ratio for the matrix.

The in-plane shear modulus (G_{12}) can also be predicted via inverse ROM formula,

$$\frac{1}{G_{12}} = \frac{1-V_f}{G_m} + \frac{V_f}{G_f} \qquad \text{Equation (6.5)}$$

Again, equation (6.5) is simple but not an accurate equation for the prediction of the in-plane shear modulus G_{12}. The cylindrical assemblage model (Hashin, 1964) gives a better approximation:

$$G_{12} = G_m[\frac{(1+V_f)+(1-V_f)G_m/G_f}{(1-V_f)+(1+V_f)G_m/G_f}] \qquad \text{Equation (6.6)}$$

The interlaminar shear modulus (G_{23}) can be computed with the semi empirical stress-partitioning parameter technique (Tsai, 1980),

$$G_{23} = G_m[\frac{V_f+(1-V_f)h_{23}}{(1-V_f)h_{23}+V_f G_m/G_f}]$$
$$h_{23} = \frac{3-4m_m+G_m/G_f}{4(1-m_m)} \qquad \text{Equation (6.7)}$$

Strength: The prediction of strength for the CCBs-filled fiber reinforced roving layer is much more difficult as compared to the elastic constants. For prediction the assumption of perfect interfacial bond is appropriate because the stresses involved are very small. Failure occurs at the weakest point in a material and a weak interface will lead to

premature failure when a substantial load is expected at the interface. Strengths of the unidirectional reinforced roving layer under five different loading conditions are of interest in this study: 1) F_{1t} : longitudinal tensile strength, psi; 2) F_{1c} : longitudinal compressive strength, psi; 3) F_{2t} : transverse tensile strength, psi; 4) F_{2c} : transverse compressive strength, psi; an 5) F_{12} : in-plane shear strength, psi;

Unidirectional composites exhibit greater strength in the longitudinal direction since the load is mostly carried by the fibers. In other loading conditions, load sharing is about equal between the fibers and the matrix. The prediction of in-plane uniaxial strengths for roving layers is discussed below.

If the composite is loaded in the longitudinal (fiber) direction, it will usually break when the stress in the fiber reaches their strength s_{fu}. Under this condition, it can be assumed that the longitudinal composite tensile strength is governed by the fiber tensile strength. Based on the ROM concept (Barbero, 1999), the longitudinal tensile strength of a roving layer can be predicted as,

$$F_{1t} = s_{fu}[V_f + (1 - V_f)E_m / E_f] \qquad \text{Equation (6.8)}$$

where, s_{fu} is the average ultimate tensile strength of fibers. Usually s_{fu} = 356,000 psi for E-glass fiber.

The longitudinal compressive strength of roving lamina is about 50% lower than the longitudinal tensile strength. The mode of failure is generally triggered by fiber micro-buckling, when individual fiber buckles inside the matrix. The buckling process is complicated and is basically controlled by fiber misalignment, shear modulus, and shear strength of the composite. The theory, developed by Barbero (1999) based on micro-buckling of fiber, was adopted in this study to predict longitudinal compressive strength of the roving lamina:

$$F1c = (\frac{c}{a} + 1)^b G_{12}$$
$$c = \frac{G_{12}\Omega}{F_{12}} \qquad \text{Equation (6.9)}$$

where, c is a dimensionless parameter;

a and b empirical parameter derived from curve fitting, a=0.21, and b=-0.69

Ω is standard deviation of fiber misalignment, radians.

F_{12} : in-plane shear strength, psi. Computation formula is shown in equation (6.12).

The transverse tensile strength of the roving lamina F_{2c} is controlled by the matrix tensile strength, the fiber-matrix interface strength, and the defects in the matrix. The transverse tensile strength is usually lower than bulk matrix. This is because the fibers are generally much stiffer than the matrix, and they may be very close and even touching each other. This induces stress concentration in the matrix that may cause premature failure when the material is loaded. None of the analytical models in the published literature predict F_{2c} accurately. In this study, the empirical formula proposed by Nielson (1967) was utilized to predict F_{2c} of roving lamina.

$$F_{2t} = s_{mtu} C_v [1 + (V_f - \sqrt{V_f})(1 - E_m / E_f)]$$

$$Cv = 1 - \sqrt{\frac{4V_f}{p(1 - V_f)}} \qquad \text{Equation (6.10)}$$

where, s_{mtu} is the tensile strength of the bulk matrix, 12,000 psi for polyester resin used in this study;

V_v is the void volume fraction, 0.02 is assumed in this study.

The same approach as for F_{2t} was followed for transverse compressive strength F_{2c}, as shown in the formula below,

$$F_{2t} = s_{ctu} C_v [1 + (V_f - \sqrt{V_f})(1 - E_m / E_f)] \qquad \text{Equation (6.11)}$$

where, s_{mcu} is the compressive strength of the bulk matrix, 17,000 psi for polyester used in this study.

In a similar manner, in-plane shear strength F_{12} can be estimated using the formula below,

$$F_{12} = t_{mu} C_v [1 + (V_f - \sqrt{V_f})(1 - G_m / G_f)] \qquad \text{Equation 2(6.12)}$$

where, t_{mu} is the shear strength of the bulk matrix, 12,000 psi for polyester used in this study.

Estimated engineering parameters: Utilizing the formulas discussed in earlier sections, the engineering parameters for a CCBs-filled roving layer were computed, as listed in Table 6.3.

Table 6.3 - Predicted engineering properties of roving lamina

Engineering Properties	**Value**
Modulus of elasticity in fiber direction, E_1	5.02 million psi
Modulus of elasticity in transverse direction, E_2	1.46 million psi
In-plane shear modulus, G_{12}	0.46 million psi
Out-of-plane shear modulus, G23	0.41 million psi
In-plane Poisson's ratio, μ_{12}	0.266
In-plane Poisson's ratio, μ_{21}	0.077
Longitudinal tensile strength, F_{1t}	0.171 million psi
Longitudinal compressive strength, F_{1c}	13,290 psi
Transverse tensile strength, F_{2t}	7,438 psi
Transverse compressive strength, F_{2c}	10,540 psi
In-plane shear strength, F_{12}	7,434 psi

Continuous strand mat layer: The CSM layer is a medium where resin is reinforced with several mats of relatively long swirl filaments. The fibers are randomly distributed in the plane of the mat. CSM is used to obtain multi-directional properties on pultrusion and other processes where unidirectional roving constitutes the main reinforcement.

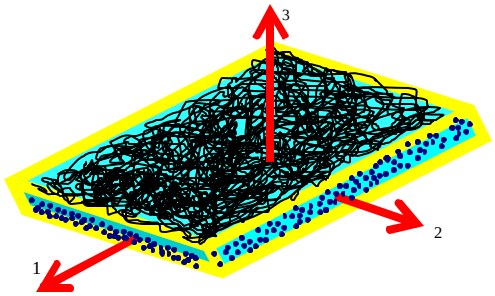

Figure 6.5 - Schematic illustration of material architecture of CSM layer

Stiffness: The elastic properties of CSM can be predicted assuming that they are random composites. A layer of composite with randomly oriented fibers can be idealized as a laminate with a large number of thin unidirectional layers, each with a different

orientation from 0^o to 180^o. The properties of the random composite are the average properties of this fictitious laminate. The isotropic properties E, G, and ν of the randomly oriented continuous filament mat can be obtained from the known properties of a unidirectional material with the same fiber volume fraction.

The modulus of elasticity can be predicted using:

$$E = \frac{3}{8}E_1 + \frac{5}{8}E_2 \qquad \text{Equation (6.13)}$$

where E1 and E2 are the longitudinal and transverse modulus of a fictitious unidirectional layer having the same fiber volume fraction as the CSM layer.

The shear modulus can be determined using:

$$G = \frac{1}{8}E_1 + \frac{1}{4}E_2 \qquad \text{Equation (6.14)}$$

The Poisson's ratio can be estimated by

$$m = \frac{E}{2G} - 1 \qquad \text{Equation (6.15)}$$

Strength: Continuous strand mat is considered a randomly oriented composite, even if in practice there is some preferential orientation of the fibers. The resulting composite is considered to be quasi-isotropic, which means that the properties are the same along any orientation on the surface of the layers. Its tensile strength may be estimated by empirical formulas developed by Haln (1975), as below:

$$Ft = \frac{4aF_{2t}}{p}[1 + 0.5\ln(\frac{F_{1t}}{a^2 F_{2t}})] \quad \text{for } a \le \sqrt{\frac{F_{1t}}{F_{2t}}}$$

$$Ft = \frac{4F_{2t}}{p}\sqrt{\frac{F_{1t}}{F_{2t}}} \quad \text{for } a > \sqrt{\frac{F_{1t}}{F_{2t}}} \qquad \text{Equation (6.16)}$$

There is no formula available to predict the compressive strength, in-plane shear strength, and interlaminar shear strength for continuous strand mat. Following Barbero (1999) approaches, this study assumes that the compressive strength is equal to one-half of tensile strength, the in-plane shear strength is one-half of the tensile strength, and the two interlaminar shear strengths are approximated by the shear strength of the matrix.

Estimated engineering parameters: With the formulas discussed above, the engineering parameters for CCBs-filled continuous strand mat were computed, as listed in Table 6.4.

Table 6.4 - Predicted engineering properties of CSM lamina

Engineering Properties	**Value**
Modulus of elasticity in fiber direction, E_1	1.628 million psi
Modulus of elasticity in transverse direction, E_2	1.628 million psi
In-plane shear modulus, G_{12}	0.58 million psi
Out-of-plane shear modulus, G23	0.58 million psi
In-plane Poisson's ratio, μ_{12}	0.405
In-plane Poisson's ratio, μ_{21}	0.405
Tensile strength, F_t	21,750 psi
Compressive strength, F_c	10,875 psi
In-plane shear strength, F_{12}	10,875 psi

6.4. Summary

The results show that the micromechanical models can be used for pultruded composites. Also, existing models for the prediction of strength properties are presented and used for the prediction of strength for roving and continuous strand mat layers.

CHAPTER 7: MACRO-MECHANICS ANALYSIS

7.1 Introduction

Macro-mechanical behavior of a lamina, and macro-mechanics analysis of a CCBs-filled FR laminate based through classical plate theory are discussed. Macro-mechanics analyzes the behavior of the lamina with the consideration of average mechanical properties of the material. Stress-strain relations in an orthotropic material in a state of plane stress with stiffness coefficients are considered. The estimated laminate engineering properties are later compared with the experimental results obtained.

7.2 Lamina mechanics

The constitutive equations of a lamina (roving or CSM layer) oriented arbitrarily with respect to a coordinate axis are discussed. This is a necessary step before conducting macro-mechanics analysis in Section 7.3. The assumption of plane stress is used to obtain a reduced version of the constitutive equations for the lamina.

In the analysis, two sets of coordinate systems are used. The material coordinate system (denoted by axes 1, 2, 3) is a Cartesian system (Figure 7.1) with the 1-axis aligned with the fiber direction. The 2-axis is on the surface of the composite, and is perpendicular to the 1-axis. The 3-axis is perpendicular to the composite surface and to the other two axes. Each layer has its own material coordinate system aligned with the fiber direction. The global coordinate system (denoted by x, y, z) is common to all the laminas in the laminate.

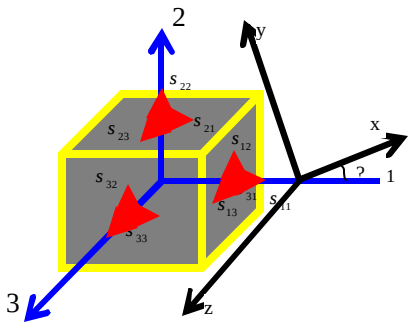

Figure 7.1 - Global and material coordinate system

The independent components of the stress or strain matrix hereafter will be written in contracted notation, as listed in the table below,

Table 7.1 - Definition of contracted notation

$s_{11} = s_1$	$e_{11} = e_1$
$s_{22} = s_2$	$e_{22} = e_2$
$s_{33} = s_3$	$e_{33} = e_3$
$s_{23} = s_{32} = s_4$	$2e_{23} = 2e_{32} = g_{23} = g_{32} = e_4$
$s_{31} = s_{13} = s_5$	$2e_{13} = 2e_{31} = g_{13} = g_{31} = e_5$
$s_{12} = s_{21} = s_6$	$2e_{12} = 2e_{21} = g_{12} = g_{21} = e_6$

Roving layer: A pultruded CCBs-filled FRC material is manufactured with a collection of thin lamina, roving and CSM. It is used in the form of a shell, which has two dimensions (length and width), which are much larger than the third dimension (thickness). Thus, it is reasonable to assume that the transverse stress is zero ($s_3 = 0$). The stress-strain equations for a roving lamina in a state of plane stress ($s_3 = 0$) can be easily derived as below through Hooke's law.

$$\begin{Bmatrix} s_1 \\ s_2 \\ s_6 \end{Bmatrix} = \begin{bmatrix} Q_{11} & Q_{12} & 0 \\ Q_{21} & Q_{22} & 0 \\ 0 & 0 & Q_{66} \end{bmatrix} \begin{Bmatrix} e_1 \\ e_2 \\ g_6 \end{Bmatrix} \qquad \text{Equation (7.1)}$$

complemented with

$$\begin{Bmatrix} s_4 \\ s_5 \end{Bmatrix} = \begin{bmatrix} Q^*_{44} & 0 \\ 0 & Q^*_{55} \end{bmatrix} \begin{Bmatrix} g_4 \\ g_5 \end{Bmatrix} \qquad \text{Equation (7.2)}$$

in compact form, (7.1) and (7.2) can be written as

$$\{s\} = [Q]\{e\}$$
$$\{t\} = [Q^*]\{?\} \qquad \text{Equation (7.3)}$$

where, $\{s\} = \{s_1, s_2, s_6\}^T$ are the in-plane stresses,

$\{e\} = \{e_1, e_2, ?_6\}^T$ are the in-plane strains,

$\{t\} = \{s_4, s_5\}^T$ are the interlaminar stresses,

$\{?\} = \{?_4, ?_5\}^T$ are the interlaminar strains,

[Q] is the 3x3 reduced stiffness matrix, and

[Q*] is the 2x2 interlaminar stiffness matrix.

The components of the 3x3 [Q] matrix and 2x2 [Q*] matrix are

$$Q_{11} = \frac{E_1}{1 - m_{12} m_{21}}$$

$$Q_{12} = \frac{m_{12} E_2}{1 - m_{12} m_{21}}$$

$$Q_{22} = \frac{E_2}{1 - m_{12} m_{21}}$$

$$Q_{66} = G_{12} = G_{13}$$

$$Q_{44}^* = G_{23}$$

$$Q_{55}^* = G_{13}$$

Equation (7.4)

As shown in Figure 6.4, the engineering properties in 2-axis and 3-axis directions are similar, and thus it can be considered as a transversely isotropic material. Therefore, it can be assumed that $G_{13} = G_{12}$ for roving layer. With stiffness properties predicted using formulas (6.1) – (6.7), as listed in Table 6.3, stiffness matrices for CCBs-filled roving lamina are given as:

$$\begin{bmatrix} Q_{11} & Q_{12} & 0 \\ Q_{21} & Q_{22} & 0 \\ 0 & 0 & Q_{66} \end{bmatrix} = \begin{bmatrix} 5.123 & 0.3966 & 0 \\ 0.3966 & 1.492 & 0 \\ 0 & 0 & 0.458 \end{bmatrix} \text{ million psi}$$

$$\begin{bmatrix} Q^*_{44} & 0 \\ 0 & Q^*_{55} \end{bmatrix} = \begin{bmatrix} 0.4058 & 0 \\ 0 & 0.4058 \end{bmatrix} \text{ million psi}$$

Equation (7.5)

Continuous strand mat: The concept that the CCBs-filled roving lamina is in plane-stress state is also applicable to CSM lamina. This means that the transverse stress is zero ($s_3 = 0$) in CSM lamina. Therefore, the stress-strain relationship for CSM layer is given by:

$$\begin{Bmatrix} s_1 \\ s_2 \\ s_6 \end{Bmatrix} = \begin{bmatrix} Q_{11} & Q_{12} & 0 \\ Q_{21} & Q_{22} & 0 \\ 0 & 0 & Q_{66} \end{bmatrix} \begin{Bmatrix} e_1 \\ e_2 \\ e_6 \end{Bmatrix}$$

$$\begin{Bmatrix} s_4 \\ s_5 \end{Bmatrix} = \begin{bmatrix} Q_{44}^* & 0 \\ 0 & Q_{55}^* \end{bmatrix} \begin{Bmatrix} g_4 \\ g_5 \end{Bmatrix}$$

Equation (7.6)

where, [Q] is the stiffness matrix and [Q*] is the interlaminar stiffness matrix.

Considering the fibers in a CSM are randomly oriented, its engineering properties are considered same in all directions. Similar to the roving layer, the isotropic properties E, G, and ν, as predicted by equations (6.13) – (6.15) can be used to develop the stiffness matrix of a randomly oriented continuous strand mat. The components of the both matrices in Eq. (7.6) are:

$$Q_{11} = \frac{E}{1 - m^2}$$

$$Q_{12} = \frac{mE}{1 - m^2}$$

$$Q_{22} = Q_{11}$$

$$Q_{66} = G$$
$$Q_{44}^* = Q_{55}^* = G \qquad \text{Equation (7.7)}$$

Predicted stiffness matrix of CSM are given below,

$$\begin{bmatrix} Q_{11} & Q_{12} & 0 \\ Q_{21} & Q_{22} & 0 \\ 0 & 0 & Q_{66} \end{bmatrix} = \begin{bmatrix} 1.947 & 0.788 & 0 \\ 0.788 & 1.947 & 0 \\ 0 & 0 & 0.58 \end{bmatrix} \text{ million psi}$$

$$\begin{bmatrix} Q^*_{44} & 0 \\ 0 & Q^*_{55} \end{bmatrix} = \begin{bmatrix} 0.58 & 0 \\ 0 & 0.58 \end{bmatrix} \text{ million psi}$$

Equation (7.8)

7.3 Lamina stiffness matrix in global coordinate system

A laminate is a set of laminas which are bonded together to form a plate or shell. Formulas that describe the engineering properties of the laminate are discussed in section 7.4. Before developing laminate properties, it is necessary to transform the lamina stiffness matrix from the material coordinate system (1, 2, and 3) to a global coordinate system (x, y, and z). The stress-strain equations (7.1), (7.2), and (7.6) are limited to the stresses and strains oriented along material coordinates. To simplify the analysis, it is convenient to relate stresses and strains in global coordinates directly. This can be done by using a stiffness matrices transformation:

$$\begin{bmatrix} \overline{Q}_{11} & \overline{Q}_{12} & \overline{Q}_{16} \\ \overline{Q}_{12} & \overline{Q}_{22} & \overline{Q}_{26} \\ \overline{Q}_{16} & \overline{Q}_{26} & \overline{Q}_{66} \end{bmatrix} = \begin{bmatrix} \cos^2(q) & \sin^2(q) & -2\cos(q)\sin(q) \\ \sin^2(q) & \cos^2(q) & 2\cos(q)\sin(q) \\ \cos(q)\sin(q) & -\cos(q)\sin(q) & \cos^2(q)-\sin^2(q) \end{bmatrix}^{-1}$$
$$\begin{bmatrix} Q_{11} & Q_{12} & Q_{16} \\ Q_{12} & Q_{22} & Q_{26} \\ Q_{16} & Q_{26} & Q_{66} \end{bmatrix}$$
$$\begin{bmatrix} \cos^2(q) & \sin^2(q) & -2\cos(q)\sin(q) \\ \sin^2(q) & \cos^2(q) & 2\cos(q)\sin(q) \\ \cos(q)\sin(q) & -\cos(q)\sin(q) & \cos^2(q)-\sin^2(q) \end{bmatrix}$$

and

$$\begin{bmatrix} \overline{Q}_{44} & \overline{Q}_{45} \\ \overline{Q}_{45} & \overline{Q}_{55} \end{bmatrix} = \begin{bmatrix} \cos(q) & \sin(q) \\ -\sin(q) & \cos(q) \end{bmatrix}^{-1} \begin{bmatrix} Q_{44} & Q_{45} \\ Q_{45} & Q_{55} \end{bmatrix} \begin{bmatrix} \cos(q) & \sin(q) \\ -\sin(q) & \cos(q) \end{bmatrix}$$

where,

$$\overline{Q}_{11} = Q_{11}\cos^4? + Q_{22}\sin^4? + 2(Q_{12} + 2Q_{66})\sin^2? \cos^2?$$

$$\overline{Q}_{12} = (Q_{11} + Q_{22} - 4Q_{66})\cos^2? \sin^2? + Q_{12}(\sin^4? + \cos^4?)$$

$$\overline{Q}_{22} = Q_{11}\sin^4? + Q_{22}\cos^4? + 2(Q_{12} + 2Q_{66})\sin^2? \cos^2?$$

$$\overline{Q}_{16} = (Q_{11} - Q_{12} - 2Q_{66})\cos^3? \sin? + (Q_{22} - Q_{12} - 2Q_{66})\cos? \sin^3?$$

$$\overline{Q}_{26} = (Q_{11} - Q_{12} - 2Q_{66})\cos? \sin^3? + (Q_{22} - Q_{12} - 2Q_{66})\cos^3? \sin?$$

$$\overline{Q}_{66} = (Q_{11} + Q_{22} - 2Q_{12} - 2Q_{66})\cos?^2\sin^2? + Q_{66}(\cos^4? + \sin^4?)$$

Equation (7.9)

$$\overline{Q}^*_{44} = Q^*_{44}\cos^2? + Q^*_{55}\sin^2?$$

$$\overline{Q}^*_{55} = Q^*_{44}\sin^2? + Q^*_{55}\cos^2?$$

Equation (7.10)

$$\overline{Q}^*_{45} = (Q^*_{55} - Q^*_{44})\cos? \sin?$$

In above equations, the $\overline{Q}_{ij}$ and $\overline{Q}^*_{ij}$ are the components of the transformed reduced stiffness matrix. The Q_{ij} and Q^*_{ij} can be obtained from equations (7.2) and (7.7). The angle ? is measured counterclockwise from the x-axis to 1-axis, as shown in Figure 7.1.

The in-plane stress-strain relationship of the lamina (roving or CSM) in global coordinate system is given by the equations below:

$$\begin{Bmatrix} s_x \\ s_y \\ s_{xy} \end{Bmatrix} = \begin{bmatrix} \overline{Q}_{11} & \overline{Q}_{12} & \overline{Q}_{16} \\ \overline{Q}_{12} & \overline{Q}_{22} & \overline{Q}_{26} \\ \overline{Q}_{16} & \overline{Q}_{26} & \overline{Q}_{66} \end{bmatrix} \begin{Bmatrix} e_x \\ e_y \\ g_{xy} \end{Bmatrix}$$

Equation (7.11)

A similar formula can be found for the interlaminar components,

$$\begin{Bmatrix} s_{yz} \\ s_{xz} \end{Bmatrix} = \begin{bmatrix} \overline{Q}^*_{44} & \overline{Q}^*_{45} \\ \overline{Q}^*_{45} & \overline{Q}^*_{55} \end{bmatrix} \begin{Bmatrix} g_{yz} \\ g_{xz} \end{Bmatrix}$$

Equation (7.12)

7.4 Macro-mechanics of a CCBs-filled FR laminate

Composite structures are built with laminates having several layers with various orientations. The layer orientations are chosen to provide adequate stiffness and strength in the direction of the applied loads, taking into account that the composite material is much stronger and stiffer in the fiber direction than in the other directions. As stated in previous sections, the material architecture of the composite material has more than one lamina, which are stacked in a certain pattern so that the reinforcements (fibers) are placed to achieve the desired laminate engineering properties.

While using a laminated composite allows the designer to optimize the material structural system, it complicates the analysis. Therefore, a relationship between the forces and moments applied to a laminate and the strains and curvatures induced in each lamina is required for the analysis and design of laminated plates and shells.

Micro-mechanics link the properties of the composite material to the properties of the constituents (fiber and matrix), as developed in Section 6.2. With the transformed lamina stiffness matrix as discussed in Section 7.2, the relationships between the structural properties of the laminate and laminas can be developed using the classical plate theory.

As shown in Figure 7.2, the basic building block of a CCBs-filled cylindrical composite utility pole is a plate element, which is subjected to bending moments and applied normal loads. To analyze the state of stress of the plate element of the laminate outer-shell, the constitutive equations, plate stiffness, and compliance equations for such elements are presented in this section.

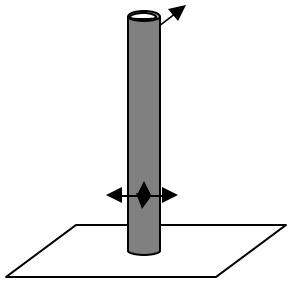

Figure 7.2 - A plate element in CCBs-filled cylindrical composite utility pole

Classical plate theory:

Classical plate theory allows analysis of stress and deformation for a composite plate, as shown in Figure 7.3. The figure shows the forces and bending moment resultants acting on a laminate composite plate element. The global coordinate system is located in such a way that x-axis is in the direction of roving fiber, x-y plane is the middle surface of the composite plate, and z is in direction of plate thickness.

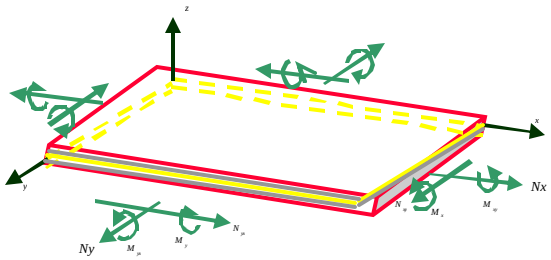

Figure 7.3 - Forces and moments resultants on a laminated plate element

Classical plate theory is based on the following assumptions known as Kirchoff hypotheses (Reddy, 1997) which are analogous to those associated with the simple bending theory of beams. Referring to Figure 7.4, the assumptions are:

- Small deflections and small strains, which means f_x and f_y are very small, and transverse deflection is the same for every point through the thickness of the plate.
- The plate is incompressible in transverse direction, which implies that the normal strain $e_{zz} \tilde{} 0$.
- Plane sections remains plane and perpendicular to the middle surface. This means that a line originally straight and perpendicular to the middle surface remains straight after the plate is deformed (line AD in Figure 7.4). This assumption is based on the experimental observation and implies that the shear strain $?_{xz}$ and $?_{yz}$ are constant throughout the thickness. This assumption is accurate for thin laminates and is a good approximation in most cases except when the laminate is thick.
- The stress normal to the middle plane s_z is small compared with the other stress components and may be neglected.

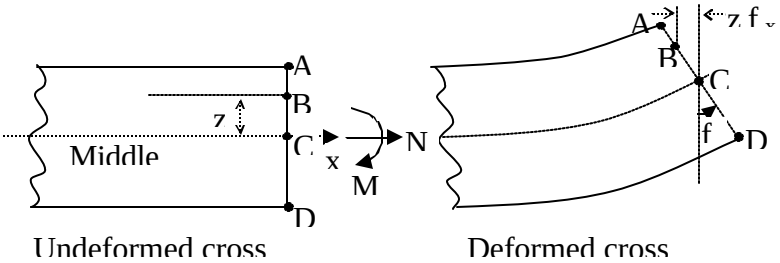

Figure 7.4 - Geometry of a deformed laminate

Figure 7.4 shows the deformation of the plate cross section in the x-z plane. Similar behavior will occur on the cross section in y-z plane when the composite plate is subjected to N_y and M_y.

With the above assumptions, the displacements at every point throughout the thickness are:

$$U(x, y, z) = U_o(x, y) - z\, f_x(x,y)$$

$$V(x, y, z) = V_o(x, y) - z\, f_y(x,y)$$

$$W(x, y, z) = W_o(x, y) \qquad \text{Equation (7.13)}$$

where, U(x, y, z) and V(x, y, z) are the displacement along the x-axis and y-axis, respectively (Figure 7.3). The functions Uo, Vo, and Wo represent the displacement of every point (x, y) of the middle surface of the laminate plate. The functions $f_x(x,y)$ and $f_y(x,y)$ are the rotation of the normal to the middle surface at each point (x, y).

Based on Kirchoff"s hypothesis, the composite laminate now has only e_x, e_y, and $?_{xy}$ strains, with all remaining strain components equal to zero. The nonzero strains can be expressed in terms of displacements:

$$e_x = \frac{\partial U}{\partial x}$$

$$e_y = \frac{\partial V}{\partial y}$$

$$?_{xy} = \frac{\partial V}{\partial x} + \frac{\partial U}{\partial y}$$

$$?_{yz} = \frac{\partial V}{\partial z} + \frac{\partial W}{\partial y}$$

$$?_{xz} = \frac{\partial U}{\partial z} + \frac{\partial W}{\partial x} \qquad \text{Equation (7.14)}$$

Then, using (7.13) and (7.14), the strains can be written as

$$e_x = \frac{\partial Uo}{\partial x} - z\frac{\partial j_x}{\partial x}$$

$$e_y = \frac{\partial Vo}{\partial y} - z\frac{\partial j_y}{\partial y}$$

$$?_{xy} = \frac{\partial Vo}{\partial x} + \frac{\partial Uo}{\partial y} - z\left(\frac{\partial j_y}{\partial x} + \frac{\partial j_x}{\partial y}\right) \qquad \text{Equation (7.15)}$$

The three equations in (7.15) can be written as,

$$\begin{Bmatrix} e_x \\ e_y \\ g_{xy} \end{Bmatrix} = \begin{Bmatrix} e^0{}_x \\ e^0{}_y \\ g^0{}_{xy} \end{Bmatrix} + z \begin{Bmatrix} k_x \\ k_y \\ k_{xy} \end{Bmatrix} \qquad \text{Equation (7.16)}$$

where, $e^0{}_x$, $e^0{}_y$, $g^0{}_{xy}$ represent the in-plane strains in the middle surface, which occur due to the stretching and shear of the plate and are defined as,

$$e^0{}_x(x,y) = \frac{\partial Uo}{\partial x}$$

$$e^0{}_y(x, y) = \frac{\partial Vo}{\partial y}$$

$$g^{0}_{xy}(x, y) = \frac{\partial Vo}{\partial x} + \frac{\partial Uo}{\partial y} \qquad \text{Equation (7.17)}$$

and the curvature of the plane due to bending k_x and k_y, and due to twisting k_{xy} are given by

$$k_x(x, y) = - \frac{\partial j_x}{\partial x}$$

$$k_y(x, y) = - \frac{\partial j_y}{\partial y}$$

$$k_{xy}(x, y) = - \left(\frac{\partial j_y}{\partial x} + \frac{\partial j_x}{\partial y}\right) \qquad \text{Equation 3(7.18)}$$

Since the rotations of the normal line (like AD in Figure 7.4) are equal to the slopes of the middle surface, or

$$f_x = \frac{\partial Wo}{\partial x}$$

$$f_y = \frac{\partial Wo}{\partial y} \qquad \text{Equation (7.19)}$$

substituting back into (7.18), the curvatures can be written in terms of Wo only as

$$k_x(x, y) = - \frac{\partial^2 Wo}{\partial x}$$

$$k_y(x, y) = - \frac{\partial^2 Wo}{\partial y}$$

$$k_{xy}(x, y) = - 2\frac{\partial^2 Wo}{\partial x \partial y} \qquad \text{Equation (7.20)}$$

Equations (7.16) along with (7.20) form the basis of the classical plate theory. Although the transverse shear deformation ($?_{xz}$ and $?_{yz}$) are neglected in this theory, it still gives reasonable approximation if the laminate is thin.

Stress resultants: To relate the laminate forces and moments to stress in each lamina, the stresses are integrated over the laminate thickness (t) to obtain the resultant forces and moments (Figure 7.3),

$$\begin{Bmatrix} N_x \\ N_y \\ N_{xy} \end{Bmatrix} = \int_{-t/2}^{t/2} \begin{Bmatrix} s_x \\ s_y \\ s_{xy} \end{Bmatrix} dz$$

$$\begin{Bmatrix} M_x \\ M_y \\ M_{xy} \end{Bmatrix} = \int_{-t/2}^{t/2} \begin{Bmatrix} s_x \\ s_y \\ s_{xy} \end{Bmatrix} z dz \qquad \text{Equation (7.21)}$$

Since the integration in (7.21) spans over several laminas, the integrals are divided into summations of integrals over each lamina

$$\begin{Bmatrix} N_x \\ N_y \\ N_{xy} \end{Bmatrix} = \sum_{k=1}^{m} \int_{z_{k-1}}^{z_k} \begin{Bmatrix} s_x \\ s_y \\ s_{xy} \end{Bmatrix}^k dz$$

$$\begin{Bmatrix} M_x \\ M_y \\ M_{xy} \end{Bmatrix} = \sum_{k=1}^{m} \int_{z_{k-1}}^{z_k} \begin{Bmatrix} s_x \\ s_y \\ s_{xy} \end{Bmatrix}^k z dz \qquad \text{Equation (7.22)}$$

where, k is the lamina number counting from the top down (Figure 7.5), m is the total number of the lamina in the laminate, and z_k is the coordinate of the bottom surface of the kth lamina (Figure 7.5).

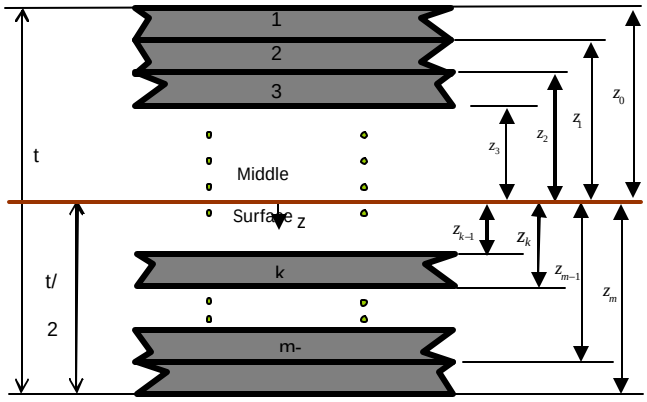

Figure 7.5 - Lamina numbering system

Laminate stiffness matrix: Since the thickness of the laminate is small compared with the in-plane dimensions of the composite plate, every lamina is in a state of plane stress. Therefore, the stress-strain relations for k^{th} lamina in the material coordinate system (7.1) and (7.2) are,

$$\begin{Bmatrix} s_1 \\ s_2 \\ s_6 \end{Bmatrix}^k = \begin{bmatrix} Q_{11} & Q_{12} & 0 \\ Q_{21} & Q_{22} & 0 \\ 0 & 0 & Q_{66} \end{bmatrix}^k \begin{Bmatrix} e_1 \\ e_2 \\ g_6 \end{Bmatrix}^k$$

$$\begin{Bmatrix} s_4 \\ s_5 \end{Bmatrix}^k = \begin{bmatrix} Q^*_{44} & 0 \\ 0 & Q^*_{55} \end{bmatrix}^k \begin{Bmatrix} g_4 \\ g_5 \end{Bmatrix}^k \qquad \text{Equation (7.23)}$$

where the superscript k indicates the lamina number (Figure 7.5).

The stress-strain relations in a global coordinate system are given by (7.11) and (7.12), namely:

$$\begin{Bmatrix} s_x \\ s_y \\ s_{xy} \end{Bmatrix}^k = \begin{bmatrix} \overline{Q}_{11} & \overline{Q}_{12} & \overline{Q}_{16} \\ \overline{Q}_{12} & \overline{Q}_{22} & \overline{Q}_{26} \\ \overline{Q}_{16} & \overline{Q}_{26} & \overline{Q}_{66} \end{bmatrix}^k \begin{Bmatrix} e_x \\ e_y \\ g_{xy} \end{Bmatrix}^k$$

$$\begin{Bmatrix} s_{yz} \\ s_{xz} \end{Bmatrix}^k = \begin{bmatrix} \overline{Q}^*_{44} & \overline{Q}^*_{45} \\ \overline{Q}^*_{45} & \overline{Q}^*_{55} \end{bmatrix}^k \begin{Bmatrix} g_{yz} \\ g_{xz} \end{Bmatrix}^k \qquad \text{Equation (7.24)}$$

Recall that the strain-displacement relations are given by (7.16), that is:

$$\begin{Bmatrix} e_x \\ e_y \\ g_{xy} \end{Bmatrix}^k = \begin{Bmatrix} e^0{}_x \\ e^0{}_y \\ g^0{}_{xy} \end{Bmatrix}^k + z \begin{Bmatrix} k_x \\ k_y \\ k_{xy} \end{Bmatrix}^k \qquad \text{Equation (7.25)}$$

Replacing (7.25) into (7.25), we have:

$$\begin{Bmatrix} s_x \\ s_y \\ s_{xy} \end{Bmatrix}^k = \begin{bmatrix} \overline{Q}_{11} & \overline{Q}_{12} & \overline{Q}_{16} \\ \overline{Q}_{12} & \overline{Q}_{22} & \overline{Q}_{26} \\ \overline{Q}_{16} & \overline{Q}_{26} & \overline{Q}_{66} \end{bmatrix}^k \left[\begin{Bmatrix} e^0{}_x \\ e^0{}_y \\ g^0{}_{xy} \end{Bmatrix}^k + z \begin{Bmatrix} k_x \\ k_y \\ k_{xy} \end{Bmatrix} \right] \qquad \text{Equation (7.26)}$$

Substituting (7.26) into (7.22), we have:

$$\begin{Bmatrix} N_x \\ N_y \\ N_{xy} \end{Bmatrix} = \sum_{k=1}^{m} \begin{bmatrix} \overline{Q}_{11} & \overline{Q}_{12} & \overline{Q}_{16} \\ \overline{Q}_{12} & \overline{Q}_{22} & \overline{Q}_{26} \\ \overline{Q}_{16} & \overline{Q}_{26} & \overline{Q}_{66} \end{bmatrix}^k \begin{bmatrix} \int_{z_{k-1}}^{z_k} \begin{Bmatrix} e^0{}_x \\ e^0{}_y \\ g^0{}_{xy} \end{Bmatrix}^k dz \\ + \int_{z_{k-1}}^{z_k} z \begin{Bmatrix} k_x \\ k_y \\ k_{xy} \end{Bmatrix} dz \end{bmatrix}, \text{ and}$$

$$\begin{Bmatrix} M_x \\ M_y \\ M_{xy} \end{Bmatrix} = \sum_{k=1}^{m} \begin{bmatrix} \overline{Q}_{11} & \overline{Q}_{12} & \overline{Q}_{16} \\ \overline{Q}_{12} & \overline{Q}_{22} & \overline{Q}_{26} \\ \overline{Q}_{16} & \overline{Q}_{26} & \overline{Q}_{66} \end{bmatrix}^k \begin{bmatrix} \int_{z_{k-1}}^{z_k} \begin{Bmatrix} e^0{}_x \\ e^0{}_y \\ g^0{}_{xy} \end{Bmatrix}^k z dz \\ + \int_{z_{k-1}}^{z_k} \begin{Bmatrix} k_x \\ k_y \\ k_{xy} \end{Bmatrix} z^2 dz \end{bmatrix} \qquad \text{Equation (7.27)}$$

Since neither the middle surface strain nor the curvatures are functions of z, equations (7.27) can be rewritten as,

$$\begin{Bmatrix} N_x \\ N_y \\ N_{xy} \end{Bmatrix} = \begin{bmatrix} A_{11} & A_{12} & A_{16} \\ A_{12} & A_{22} & A_{26} \\ A_{16} & A_{26} & A_{66} \end{bmatrix} \begin{Bmatrix} e^0{}_x \\ e^0{}_y \\ g^0{}_{xy} \end{Bmatrix} + \begin{bmatrix} B_{11} & B_{12} & B_{16} \\ B_{12} & B_{22} & B_{26} \\ B_{16} & B_{26} & B_{66} \end{bmatrix} \begin{Bmatrix} k_x \\ k_y \\ k_{xy} \end{Bmatrix}$$

Equation (7.28)

$$\begin{Bmatrix} M_x \\ M_y \\ M_{xy} \end{Bmatrix} = \begin{bmatrix} B_{11} & B_{12} & B_{16} \\ B_{12} & B_{22} & B_{26} \\ B_{16} & B_{26} & B_{66} \end{bmatrix} \begin{Bmatrix} e^0{}_x \\ e^0{}_y \\ g^0{}_{xy} \end{Bmatrix} + \begin{bmatrix} D_{11} & D_{12} & D_{16} \\ D_{12} & D_{22} & D_{26} \\ D_{16} & D_{26} & D_{66} \end{bmatrix} \begin{Bmatrix} k_x \\ k_y \\ k_{xy} \end{Bmatrix}$$

Equation (7.29)

where, $N^T=(N_x, N_y, N_{xy})$ is the vector of in-plane force resultants;

$M^T=(M_x, M_y, M_{xy})$ is the vector of moment resultants;

$e^T=(e^o_x, e^o_y, ?^o_{xy})$ is the vector of middle surface strain resultants;

$k^T=(k_x, k_y, k_{xy})$ is the vector of plate curvature resultants;

A_{ij}, B_{ij}, and D_{ij} are the elements of the compliance matrix as defined below.

$$A_{ij} = \int_{-\frac{t}{2}}^{\frac{t}{2}} \left(\overline{Q}_{ij}\right)_k dz = \sum_{k=1}^{m} \left(\overline{Q}_{ij}\right)_k \left(z_k - z_{k-1}\right)$$

$$B_{ij} = \int_{-\frac{t}{2}}^{\frac{t}{2}} \left(\overline{Q}_{ij}\right)_k z dz = \frac{1}{2}\left[\sum_{k=1}^{m} \left(\overline{Q}_{ij}\right)_k \left(z_k^2 - z_{k-1}^2\right)\right]$$

$$D_{ij} = \int_{-\frac{t}{2}}^{\frac{t}{2}} \left(\overline{Q}_{ij}\right)_k z^2 dz = \frac{1}{3}\left[\sum_{k=1}^{m} \left(\overline{Q}_{ij}\right)_k \left(z_k^3 - z_{k-1}^3\right)\right]$$

Equation (7.30)

where, $\left(\overline{Q}_{ij}\right)_k$ is the component of the stiffness matrix of kth lamina of the laminate in global coordinate system.

Combining equations (7.28) and (7.29), we have,

$$\begin{Bmatrix} N_x \\ N_y \\ N_{xy} \\ \hline M_x \\ M_y \\ M_{xy} \end{Bmatrix} = \left[\begin{array}{ccc:ccc} A_{11} & A_{12} & A_{16} & B_{11} & B_{12} & B_{16} \\ A_{12} & A_{22} & A_{26} & B_{12} & B_{22} & B_{26} \\ A_{16} & A_{26} & A_{66} & B_{16} & B_{26} & B_{66} \\ \hline B_{11} & B_{12} & B_{16} & D_{11} & D_{12} & D_{16} \\ B_{12} & B_{22} & B_{26} & D_{12} & D_{22} & D_{26} \\ B_{16} & B_{26} & B_{66} & D_{16} & D_{26} & D_{66} \end{array}\right] \begin{Bmatrix} e_x^0 \\ e_y^0 \\ ?_{xy}^0 \\ \hline ?_x \\ ?_y \\ ?_{xy} \end{Bmatrix} \qquad \text{Equation (7.31)}$$

Equations (7.31) are called stiffness equations because of their similarity with Hooke's law. In the compounded stiffness matrix, the coefficients A_{ij}, B_{ij}, and D_{ij} are functions of the laminate thickness, fiber orientation, lamina stacking sequence, and material properties of the laminas. Each element matrix ([A], [B], or [D]) has a particular role in the analysis of the laminate. The [A] matrix is in-plane stiffness matrix because it directly relates in-plane strains (e^o_x, e^o_y, $?^o_{xy}$) to in-plane forces (N_x, N_y, N_{xy}). The [D] matrix is the bending stiffness matrix because it relates curvatures (k_x, k_y, k_{xy}) to bending moments (M_x, M_y, M_{xy}). The [B] matrix relates in-plane strains to bending moments and curvatures to in-plane forces. Therefore, [B] is called a bending-extension coupling matrix.

Equivalent laminate elastic moduli: A set of equivalent laminate moduli (E_x, E_y, G_{xy}, μ_{xy}) can be determined from the [A], [D] matrix as discussed in section above. The moduli represent the stiffness of a fictitious, equivalent, orthotropic plate that behaves like the actual laminate under the same loads. If the laminate is under in-plane loads, and there are no bending loads, the equivalent laminate stiffness can be computed as follows. The average in-plane elastic modulus in roving fiber direction is:

$$E_{xx} = [A_{11} - (A_{12}^2 / A_{22})]/t \qquad \text{Equation (7.32)}$$

Average in-plane elastic modulus in the circumferential direction is

$$E_{yy} = [A_{22} - (A_{12}^2 / A_{11})]/t \qquad \text{Equation (7.33)}$$

Average in-plane shear modus is,

$$G_{xy} = A_{66}/t \qquad \text{Equation (7.34)}$$

and in-plane Poisson's ratio is

$$m_{xy} = A_{12} / A_{22} \qquad \text{Equation (7.35)}$$

The above formulas are valid for in-plane loads only, and they can not be used to predict bending response of a CCBs-filled FR cylindrical laminate composite utility pole. Instead of using matrix [A], bending stiffness matrix [D] should be utilized to predict flexural moduli. The average flexural modulus in the axial direction is

$$E_{xx} = \frac{12(D_{11}D_{22} - D_{12}^2)}{t^3 D_{22}} \qquad \text{Equation (7.36)}$$

average flexural modulus in the circumferential direction is

$$E_{yy} = \frac{12(D_{11}D_{22} - D_{12}^2)}{t^3 D_{11}} \qquad \text{Equation (7.37)}$$

average shear modulus is

$$G_{xy} = \frac{12D_{66}}{t^3}$$ Equation (7.38)

and Poisson's ratio is

$$m_{xy} = \frac{D_{12}}{D_{22}}$$ Equation (7.39)

For a cylindrical utility pole that is subject to bending loads, its structural bending stiffness, S, is

$$S = E_{xx}I = \frac{12(D_{11}D_{22} - D_{12}^{\ 2})}{t^3 D_{22}} p \frac{(D-t)^3}{8} t$$ Equation (7.40)

7.5. Predicted engineering properties of the CCBs-filled laminate

The classical plate theory is used to predict macro-mechanical behavior of the CCBs-based laminated composite. Denoting R as roving and C as CSM, the material architecture of the CCBs-filled FR laminated composite can be coded as [C/R/C/R/C/R/C], as shown in Figure 6.3. The material architecture can be considered symmetric with respect to the middle surface. Therefore, all the bending-extension coupling coefficients B_{ij} in equation (7.31) are zero. In addition, since the local coordinate system of the roving and CSM layers are the same as the global coordinate system, ? is zero and 90^o. Consequently, $\left(\overline{Q}_{ij}\right)_k = \left(Q_{ij}\right)_k$.

The determination of material properties for individual lamina was addressed in Chapter 6. A program was developed using Mathcad for macro mechanical analysis of the CCBs-based composite (Appendix C). Table 7.2 lists the stacking sequence of the laminate and thickness of each lamina, which were measured directly from microscopic picture of the cross section of CCBs-filled FRC.

Table 7.2 - Stacking sequence and thickness of each layer

Layer	Material	Layer thickness, in
1	CSM	0.02510
2	Roving	0.05170
3	CSM	0.02000
4	Roving	0.04330
5	CSM	0.02420
6	Roving	0.04360
7	CSM	0.02960
Total thickness, in		0.23750

Equations (7.41) list the [A], [B], and [D] matrix for the CCBs-filled FRC outer-shell material are given below:

$$\begin{bmatrix} A_{11} & A_{12} & A_{16} \\ A_{12} & A_{22} & A_{26} \\ A_{16} & A_{26} & A_{66} \end{bmatrix} = \begin{bmatrix} 1.004e6 & 1.629e5 & 0 \\ 1.629e5 & 4.716e5 & 0 \\ 0 & 0 & 1.211e5 \end{bmatrix}$$

$$\begin{bmatrix} B_{11} & B_{12} & B_{16} \\ B_{12} & B_{22} & B_{26} \\ B_{16} & B_{26} & B_{66} \end{bmatrix} = \begin{bmatrix} -1557 & 409 & 0 \\ 409 & 679 & 0 \\ 0 & 0 & 69.81 \end{bmatrix}$$

$$\begin{bmatrix} D_{11} & D_{12} & D_{16} \\ D_{12} & D_{22} & D_{26} \\ D_{16} & D_{26} & D_{66} \end{bmatrix} = \begin{bmatrix} 4209 & 899.7 & 0 \\ 899.7 & 2439 & 0 \\ 0 & 0 & 592.2 \end{bmatrix} \qquad \text{Equation (7.41)}$$

Substituting the values of [A] and [D] matrix into the formula (7.32) – (7.39), the equivalent orthotropic stiffness of the CCBs-filled composite was calculated. Table 7.3 lists the apparent in-plane engineering properties obtained using the classical plate theory.

Table 7.3 - Apparent engineering properties of the laminate

	E_x (million psi)	E_y (million psi)	G_{xy} (million psi)	μ_{xy}
Predicted in-plane stiffness	3.99	1.874	0.51	0.345
Actual in-plane stiffness	3.95	1.354	-	-
Predicted bending stiffness	3.473	2.012	0.53	0.369

The theoretical prediction of the longitudinal elastic modulus (Ex = 3.94 million psi) is in good agreement with laboratory test results (E1= 3.95 million psi). However, the theoretical transverse elastic modulus (Ey = 1.92 million psi) and experimental value (E2 = 1.35 million psi) do not agree well.

7.6. Summary

The predicted engineering laminate properties are in relatively good agreement with the average of the experimental values given in Chapter 8.

CHAPTER 8: ENGINEERING PROPERTIES CHARACTERIZATION

8.1 Introduction

Fiber-reinforced composites may be orthotropic materials, which are usually very strong along the fiber direction and relatively weak in the transverse direction. In this study, various laboratory test methods were used to evaluate the engineering properties of the CCBs-filled FRC outer-shell material, following ASTM standards. Tests included axial tension, axial compression, off-axis tension, off-axial compression, flexural bending, water absorption, dielectric constant, and UV degradation. For off-axis tensile and compressive tests results, a comparison was made between the experimental values and the predicted laminate stiffness values.

8.2 Tensile engineering properties

A utility pole is primarily subjected to compressive loading on one side and tensile loading on the other side when bent due to pull force exerted by the transmission wires. In addition, due to an unbalanced pulling force on the cross-arm, the composite utility pole may also be subjected to a torsional moment. As the result of the combined effect of tension and torsion, major tensile stress in certain parts of the outer-shell may deviate from the axial (longitudinal) direction. Thus, the utility pole may be subject to off-axis tensile loading conditions. Therefore, it is important to evaluate the engineering properties of the composite material under both tensile and off-axis tensile loading conditions.

Longitudinal and transverse in-plane tensile properties:

The tests were conducted along the pultrusion and transverse (perpendicular to pultrusion) directions following procedures outlined in ASTM D 638-97. Variation of the distance between two designated points on the specimen was automatically measured by an extensometer, to calibrate this system. Several standard aluminum ASTM samples (Figure 8.1) were tested and average value of about 9.97 million psi for elastic modulus was observed for these calibration samples. The tensile test sample had geometry as shown in Figure 8.2, which represents a type I specimen specified in ASTM D638-97 based on the given thickness (0.25 in.) of the composite material.

Specimens were first cut from original pultruded plates using a power saw. Then the raw specimens were trimmed and ground precisely to desired dimensions using a grinding machine. Two types of samples were prepared: lengthwise (LW) sample and crosswise (CW) sample. Seven (7) samples were prepared for each pultruded plate with two fly ash loading levels of 5% and 10%. Five to eight (5-8) specimens, for each type of sample, were prepared and thirty-three (33) were tested in total. All the specimens were loaded incrementally at the rate of 1.2 mm/min. Some samples are shown in Figure 8.3.

Figure 8.1 - Aluminum calibration specimens

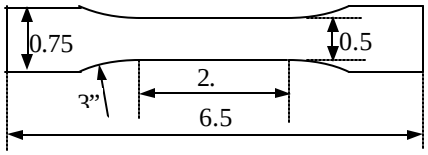

Figure 8.2 - Dimensions of the ASTM tensile test specimen

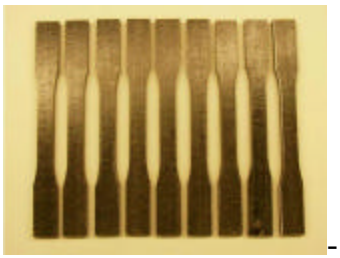

Figure 8.3 - Prepared tension test specimens of CCBs-based composite

Axial load was then applied in a displacement control mode at a rate of 0.02 in/min. The data for force, displacement, and strains were obtained through an external data acquisition system throughout the test. Twenty-seven (27) out of the 33 prepared specimens gave valid test results, as shown in Table 8.1(a) and Table 8.1(b).

Table 8.1(a) - Tensile test results for lengthwise samples

Sample #	Fly ash % %	Peak stress psi	Ultimate Stress psi	Modulus psi
LW-FRP5%a	5	53,815	24,422	4,545,354
LW-FRP5%b	5	52,103	52,103	4,082,343
LW-FRP5%d	5	49,372	48,159	3,219,459
LW-FRP5%e	5	50,722	50,790	4,700,544
LW-FRP5%f	5	48,061	48,061	5,453,951
LW-FRP5%g	5	50,554	44,669	3,558,817
LW-FRP5%h	5	53,148	53,148	2,903,620
LW-FRP5%I	5	50,490	47,398	3,106,376
Mean	5	51,033	46,094	3,946,308
Std Deviation	0	1,911	9,177	901,615
LW-FRP10%b	10	51,016	50,580	5,522,711
LW-FRP10%c	10	50,800	48,940	3,763,290
LW-FRP10%e	10	52,600	51,930	3,438,761
LW-FRP10%f	10	50,280	22,940	4,071,533
LW-FRP10%g	10	53,300	52,690	4,307,271
LW-FRP10%h	10	53,940	53,230	4,033,840
LW-FRP10%I	10	53,440	53,410	3,644,741
LW-FRP10%j	10	56,080	55,780	3,216,449
Mean	10	52,682	48,688	3,999,825
Std Deviation	0	1,934	10,599	710,182

Table 8.1(b) - Tensile test results for crosswise samples

Sample #	Fly ash % %	Peak stress psi	Ultimate Stress psi	Modulus psi
CW-FRP5%a	5	8,857	8,857	1,819,291
CW-FRP5%c	5	8,714	8,714	1,580,560
CW-FRP5%d	5	8,644	8,644	607,650
CW-FRP5%e	5	8,877	8,877	806,809
CW-FRP5%g	5	8,091	8,091	1,315,607
Mean	5	8,637	8,637	1,225,983
Std Deviation	0	320	320	510,836
CW-FRP10%a	10	8,822	8,822	1,184,697
CW-FRP10%b	10	9,987	9,971	1,323,280
CW-FRP10%c	10	9,227	9,227	1,128,970
CW-FRP10%d	10	9,649	9,649	1,353,490
CW-FRP10%e	10	7,907	7,894	1,105,286
CW-FRP10%f	10	7,908	7,908	1,309,077
Mean	10	8,917	8,912	1,234,133
Std Deviation	0	875	874	107,624

Test results revealed that the differences in engineering properties for 5% fly ash panel and 10% fly ash panel were statistically insignificant for lengthwise and crosswise samples. When loaded along the pultrusion direction, 5% fly ash panel had 3,946,308 psi elastic modulus and 48,094 psi failure strength, whereas 10% panel had 3,999,825 psi and 48,688 psi, respectively. For transversely loaded samples, elastic modulus and failure strength for 5% fly ash panel were 1,225,983 psi and 8,637 psi, respectively. For 10% fly ash panel similar values were 1,234,133 psi and 8,912 psi, respectively.

The material has much higher elastic modulus and strength in the pultrusion direction than in the transverse direction. This is an advantage from design point of view because the outer-shell material is mainly subjected to tensile and compressive stresses along the pultrusion direction.

Off-axis in-plane tensile properties:

An engineered composite pole may be subjected to off-axis loading conditions because of the combined effect of bending and torsional loads. In-plane off-axis tensile tests were conducted on the flat panels in accordance with the ASTM D 638-97 standard. The objective of the off-axis tests was to investigate elastic and inelastic stress-strain behavior up to the ultimate failure point.

Specimens were first cut from original pultruded plates using a power saw by purposely orienting the roving fiber at different off-axis angles of 0^o, 15^o, 30^o, 45^o, 60^o,

75°, and 90°. The raw specimens were then trimmed and ground precisely to desired dimensions using a grinding machine. Five to six specimens were prepared for each orientation angle and seventy-four (74) total samples were tested.

Based on the test results, the effect of roving fiber orientation on the outer-shell tensile material properties was evaluated. Most of the samples showed a relatively smooth stress-strain curve before the material started to yield, beyond which the curve showed a serrated stress-strain curve as illustrated in Figure 8.4. This behavior points to the development of micro-cracks and debonding of fiberglass from the matrix. In addition, since roving fiber does not provide much strength for high angle off-axis loading, randomly oriented continuous strand mat and randomly distributed voids tend to govern overall behavior of the material once debonding of fiber and matrix initiates. The scatter in the data increases with larger angles between 45° and 90°. This supports the previous conclusion about the role of continuous strand mat and the defects in the matrix.

Figure 8.5 shows the tensile stress-strain results for all off-axis angles. In the case of 0° specimens, the material shows a near-linear stress-strain response except at high strain values close to failure. The non-linear stress-strain behavior is more evident in other off-axis tension specimens for all orientations. Non-linear behavior is observed for 15° specimens at a relatively high applied strain. However, it starts at very low strain magnitudes especially for the 30°, 45°, 60°, 75°, and 90° specimens. In the case of the 0° and 15° specimens, a non-linear response is more pronounced after about 0.3% axial strain magnitude.

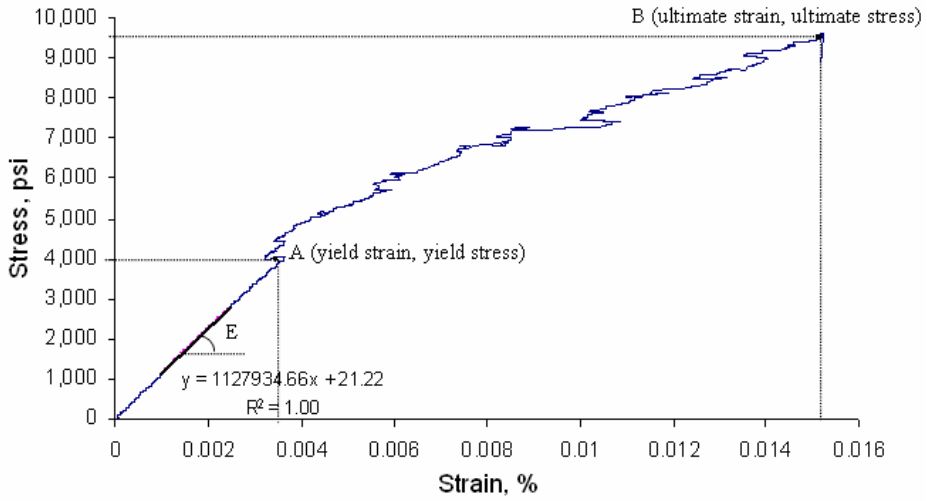

Figure 8.4 - Typical stress-strain curve of a CCBs-based tensile sample

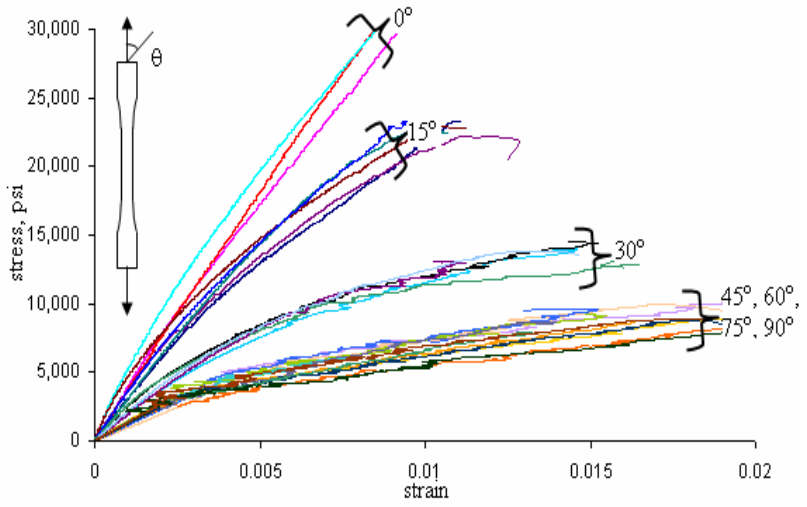

Figure 8.5 - Tensile stress-strain curves for all off-axis angles

For comparison purposes, five parameters were calculated for all off-axis specimens: elastic modulus, yield stress, yield strain, ultimate strain, and ultimate stress as illustrated in Figure 8.6. The elastic modulus was defined as the slope of the linear fit for the experimental stress-strain data between 1000 and 3000 με, according to the ASTM standard. The yield point was located at the starting point (point A) of the serrated stress-strain curve. The material was assumed to start to yield (debonding of fiber and matrix) when stress-strain curve starts to show waviness. The highest stress and its corresponding strain (point B) were defined as ultimate stress and ultimate strain. Following the above approach, the five parameters were carefully checked and calculated for all off-axis tensile samples, as listed in Table 8.2. Several samples were discarded due to experimental error and unexpected breakage (exceeded the strain gage range).

Table 8.3 lists the mean values and standard deviation for each off-axis angle sample tested. The ratio between the average elastic modulus of 90^o (3.9 million psi) specimens and that of the 0^o (1.3 million psi) specimens is about one third (34%). The ratio between the average yield stress and ultimate stress of 90^o (2,213 psi and 8,397 psi) specimens and those of the 0^o specimens (41,777 psi and 49,211 psi) are about 5.3% and 17%, respectively.

Table 8.2 - Off-axis tensile test results

Off-axis Degree	Sample #	E, psi	Yield stress (psi)	Yield strain, %	Ultimate stress, psi	Ultimate strain, %	Width, in	Thickness, in
0	A	3,880,203	46,049	1.004	53,334	1.361	0.235	0.43
	B	4,001,891	46,523	1.105	54,475	1.700	0.235	0.431
	C	3,766,954	37,996	1.047	42,412	1.613	0.234	0.427
	e	4,166,582	36,539	1.104	46,624	1.484	0.234	0.428
15	a	2,926,549	15,899	0.768	23,330	1.670	0.235	0.416
	b	3,153,222	19,318	0.855	22,155	1.706	0.234	0.416
	c	3,097,135	19,554	0.789	22,867	1.626	0.236	0.415
	d	3,153,515	20,348	0.779	22,720	1.580	0.235	0.416
	e	3,257,234	18,978	0.718	23,286	1.538	0.235	0.424
30	a	1,768,026	8,510	0.571	13,993	1.460	0.238	0.474
	b	2,076,044	9,220	0.573	14,416	1.500	0.238	0.465
	c	2,140,364	8,965	0.678	12,850	1.606	0.238	0.465
	d	1,823,503	9,327	0.568	12,935	1.083	0.238	0.468
	e	1,973,197	9,238	0.575	13,847	1.338	0.238	0.467
45	a	1,156,066	4,588	0.390	9,773	1.298	0.236	0.485
	b	1,142,136	4,250	0.370	10,295	1.575	0.236	0.473
	c	1,023,840	4,545	0.433	9,991	1.418	0.234	0.474
	d	1,092,564	4,436	0.365	9,608	1.520	0.236	0.477
	e	1,125,488	5,076	0.462	10,616	1.056	0.235	0.48
60	a	1,314,705	2,834	0.210	8,877	1.509	0.2385	0.485
	b	1,244,818	3,814	0.333	8,977	1.938	0.239	0.485
	c	1,252,664	3,280	0.293	6,087	1.790	0.238	0.487
	e	1,269,953	3,181	0.268	8,602	1.638	0.239	0.483
75	a	1,245,107	2,580	0.228	8,503	2.038	0.237	0.428
	b	1,270,264	2,205	0.173	8,682	1.463	0.237	0.427
	c	1,336,805	1,564	0.113	7,311	1.360	0.236	0.421
	d	1,240,447	2,369	0.185	8,835	1.835	0.2365	0.424
	e	1,435,684	2,359	0.170	7,892	1.313	0.237	0.425
90	a	1,344,910	2,100	0.164	9,088	2.088	0.238	0.506
	b	1,343,784	1,742	0.124	7,450	2.080	0.238	0.511
	d	1,288,413	2,657	0.205	8,856	1.860	0.238	0.501
	e	1,440,432	2,354	0.190	8,194	1.690	0.2375	0.497

Table 8.3 - Mean value and standard deviation of off-axis tensile tests

Off-axis Degree		E, psi	Yield stress (psi)	Yield strain, %	Ultimate stress, psi	Ultimate strain, %	Width, in	Thickness, in
0	Mean	3,953,908	41,777	1.065	49,211	1.539	0.235	0.429
	Std. Dev.	171,189	5,244	0.049	5,705	0.149	5.00E-04	0.002
15	Mean	3,117,531	18,819	0.781	22,872	1.624	0.235	0.417
	Std. Dev.	121,425	1,709	0.049	479	0.068	7.00E-04	0.004
30	Mean	1,956,227	9,052	0.593	13,608	1.397	0.238	0.468
	Std. Dev.	159,363	332	0.048	687	0.200	0	0.004
45	Mean	1,108,019	4,579	0.404	10,057	1.373	0.235	0.478
	Std. Dev.	52,685	307	0.042	405	0.207	9.00E-04	0.005
60	Mean	1,270,535	3,277	0.276	8,136	1.719	0.239	0.485
	Std. Dev.	31,263	406	0.051	1,375	0.186	5.00E-04	0.002
75	Mean	1,305,661	2,215	0.174	8,245	1.602	0.237	0.425
	Std. Dev.	82,232	388	0.041	633	0.319	4.00E-04	0.003
90	Mean	1,354,385	2,213	0.171	8,397	1.930	0.238	0.503
	Std. Dev.	63,136	388	0.035	736	0.191	4.00E-04	0.006

The repeated off-axis tensile tests clearly show the effect of the orientation of roving fiber on the tensile loading properties of the composite material. Figure 8.6 shows the variations of average tensile elastic modulus and its corresponding 95% confidence intervals for different off-axis angles. It is clear that the elastic modulus of the material decreases dramatically from about 4 million psi to about 1.2 million psi for off-axis angles ranging from 0^o to 45^o, after which the effect of roving fiber orientation is not pronounced.

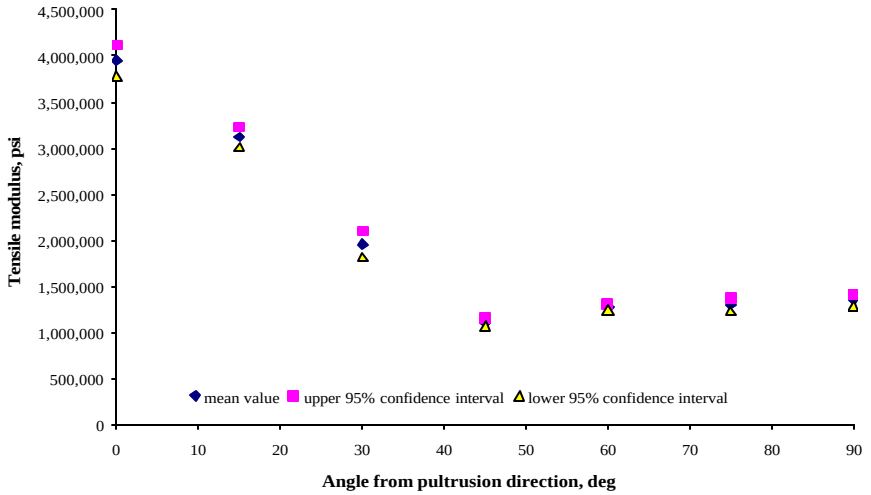

Figure 8.6 - Variation of average elastic modulus with off-axis angle

Figure 8.7 shows the average yield stress and ultimate failure stress. The average yield stress decreases sharply from 42 ksi to 4.3 ksi when roving fiber orientation varies from 0 to 45 degrees. The ultimate failure strength also drops rapidly from 49 ksi to 10 ksi within 45-degree change of the roving fiber orientation. When the off-axis angle is greater than 45 degrees, the material yield strength and failure strength are not governed by the roving fiber orientation. Results show that the yield stress and ultimate stress are almost constant (3.5 ksi and 8 ksi, respectively) for any off-axis angle greater than 45 degrees. This indicates that, when loaded at high off-axis angles, continuous strand mat is the main reinforcement providing strength for the material.

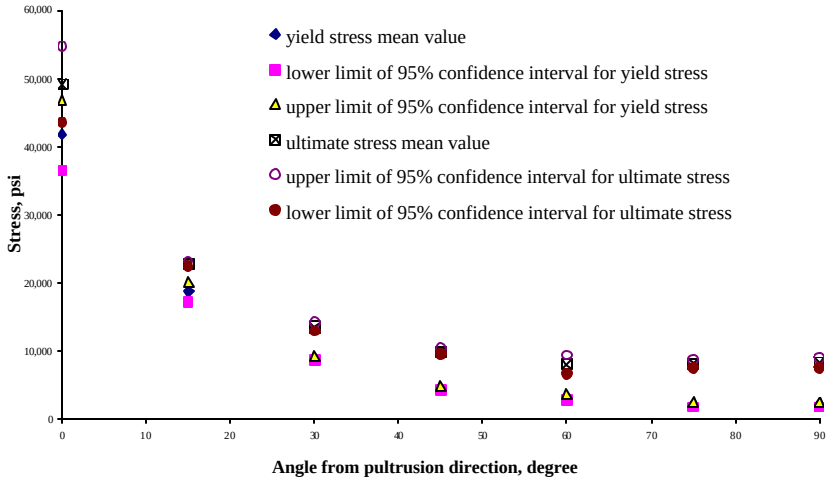

Figure 8.7 - Variation of average yield stress and ultimate tensile stress vs. off-axis angle

Figure 8.8 illustrates the average yield strain and ultimate failure strain of the material at different off-axis angles. Similar to the trends for the yield stress, yield strain of the material decreases from 1% to 0.3% with an increase in the off-axis angle from 0 to 60 degrees. The ultimate failure strain, as shown in Figure 8.8, is not affected greatly by the roving fiber orientation. These values are between 1.2% and 2.1%. It is interesting to note (from Figure 8.8) that a 1.5% axial strain can be used as the critical strain in the maximum strain type failure criterion regardless of the orientation of the roving reinforcement.

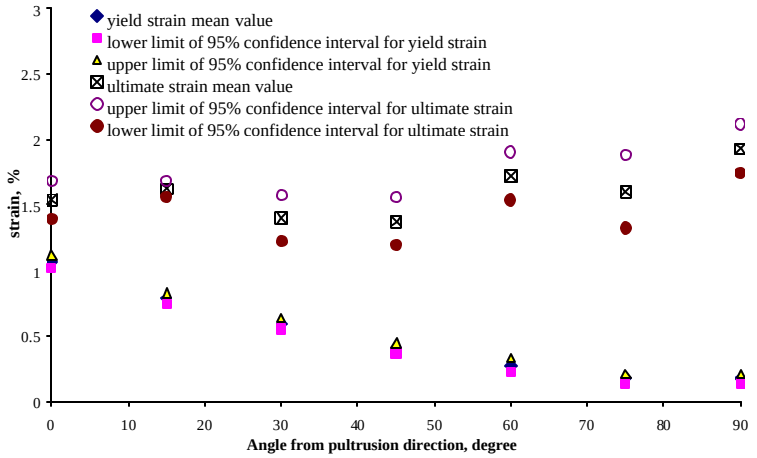

Figure 8.8 - Variation of average yield strain and ultimate strain of tension tests with off-axis angle

Experimental and theoretical results comparison:

A comparison is made here between the average experimental elastic modulus and the theoretically predicted elastic modulus using micro-mechanics analysis and macro-mechanics analysis as discussed in Chapters 6 and 7. Since the CSM lamina can be considered as a transversely isotropic material, its in-plane engineering properties can be assumed isotropic. Therefore, it should not affect the global engineering properties of the CCBs-filled composite laminate in the off-axis test. The change in loading directions on the composite laminate can be considered as change in unidirectional fiber orientation in the roving lamina, which governs material engineering properties of the composite laminate. In the laboratory off-axis tensile test, the roving fiber orientation was changed from zero degree (longitudinal) to 90 degree (transverse to fiber orientation) in steps of 15 degrees. To compare the experimental results with the theoretical prediction results, the composite laminate engineering properties predicted using the classical plate theory (as discussed in Chapter 7) were calculated by increasing the roving fiber orientation ? in equation (7.9) and (7.10) from 0 degree to 90 degree in steps of 15 degrees.

Table 8.4 lists the elastic modulus of the composite laminate measured in off-axis tensile tests in the laboratory and predicted using micro/macro-mechanics analysis. It is clear that, even though the predicted elastic modulus are generally a little higher than

those from laboratory results, there is a good match between both in terms of the effect of roving fiber orientation on the variation of the laminate elastic modulus, as shown in (Figure 8.9). The predicted results are slightly higher than laboratory results because the tested material contains some micro-voids and cracks.

Table 8.4 - Comparison of measured E and predicted E values.

Fiber orientation, degree	Measured E, psi	Predicted E, psi
0	3,953,908	3,976,000
15	3,117,531	3,257,000
30	1,956,227	2,069,000
45	1,108,019	1,310,000
60	1,270,535	1,474,000
75	1,305,661	1,604,000
90	1,354,385	1,676,000

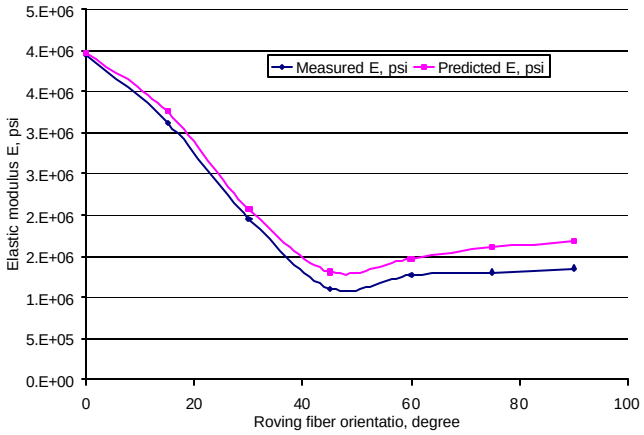

Figure 8.9 - Comparison of measured and predicted E values for different roving fiber orientation

8.3. Axial and off-axis compressive stiffness and strength

It is important that compressive strength and stiffness properties are considered in the utility pole design. Due to unbalanced pulling forces on a cross-arm, the composite utility pole may also be subjected to torsional moments. As the result of the combined effects of compression and torsion, major compressive stresses at certain locations of the outer-shell may orient along an off-axis (longitudinal) direction. Thus, it is important to evaluate the engineering properties of the composite material under compression for different off-axis loading conditions.

In this section, in-plane off-axis compression tests were designed and conducted on the pultruded flat panels following procedures outlined in ASTM D 695-96. Using the MTS system described earlier, the standard suggests using a dog-bone shape specimen, (Figure 8.13).

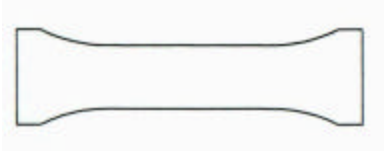

Figure 8.13 - Compression test specimen

Similar to the samples in the off-axis tensile tests, the off-axis compression test specimens were first cut from original pultruded plates using a power saw at different off-axis angles (0^o, 15^o, 30^o, 45^o, 60^o, 75^o, and 90^o). Six specimens were prepared for each angle. With two fly ash loading levels (5% and 10% fly ash), eighty-four (84) samples in total were prepared (Figure 8.14).

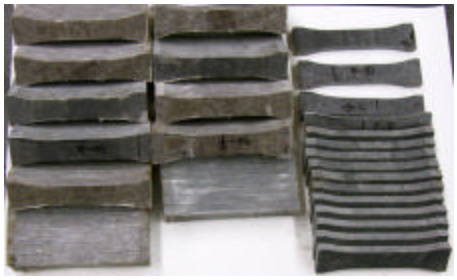

Figure 8.14 - Prepared compression test specimen of CCBs-based composite

To prevent the sample from failing in the buckling mode, a support jig was fabricated as required by ASTM and used to support the sample laterally (Figure 8.15). Variation of the distance between two designated points on the specimen is automatically measured by an extensometer of the MTS machine. To calibrate the system, several polycarbonate samples were prepared and tested.

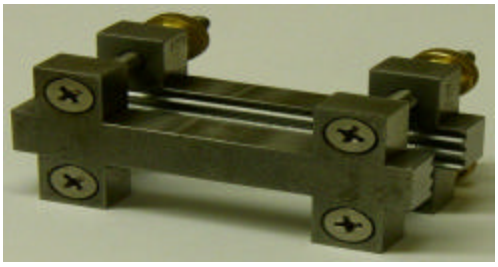

Figure 8.15 - Test sample support jig

The axis of the sample was aligned with the centerline of the loading nose. The axial load was applied in a displacement control mode with a rate of 0.02 in/min as recommended by the ASTM standard. All tests were repeated six times and loaded to failure. Most of the samples failed in brittle mode. For comparison purposes, elastic modulus, failure strain, and failure strength were calculated for all off-axis compression

Table 8.5 and Table 8.6 list the test results for 5% fly ash and 10% fly ash samples, respectively. The average value and the standard deviation for these parameters are listed in Table 8.7. Test results show that the average elastic modulus of the composite in transverse direction are 57% and 47% of the corresponding values in the longitudinal direction. Similarly, the average failure strength of 90^o specimens are 28% and 25% of the 0^o values for 5% and 10% fly ash loading levels.

The off-axis compression tests show the effect of the orientation of roving fiber on compressive strength. As shown in Figure 8.17, the average elastic modulus of the material decreases rapidly from about 1.5 to 1.6 million psi to about 700,000 to 900,000 psi for off-axis angles ranging from 0^o to 45^o, beyond which the effect of roving fiber orientation is not evident. Following a similar trend, the failure strength also drops quickly from 67 ksi to 20 ksi within 45^o change of roving fiber orientation (Figure 8.18). When the off-axis angle is greater than 45^o, the material yield strength and failure strength are not governed by the roving fiber orientation. Figure 8.19 shows that the failure strain for both types of composites range from 3% to 4%. This value could be used in a strain-controlled failure criterion. Compression test results for both types of composites do not show significant effects of fly ash loading level on material engineering properties. Only Figure 8.18 shows slightly enhanced material strength with the increase in fly ash loading level.

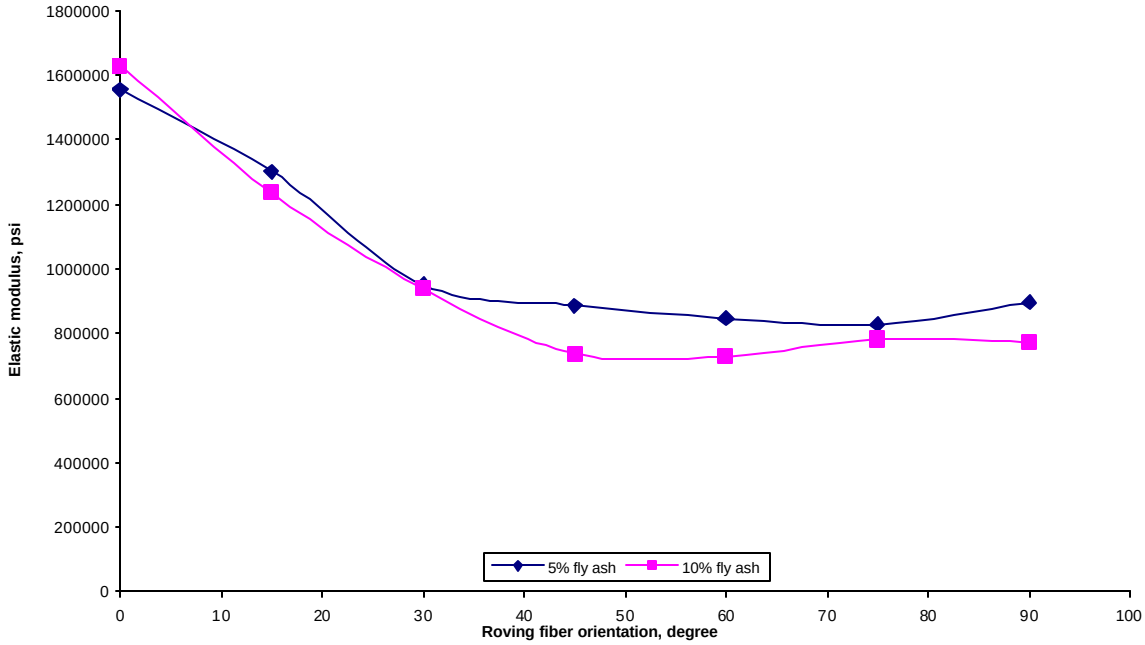

Figure 8.17 - Variation of elastic modulus with roving fiber orientation

Table 8.5 - Off-axis compression test results for 5%-fly-ash samples

Degree	Sample #	Width, in	Thickness, in	Length, in	E, psi	Failure strength, psi	Failure strain, in/in
	Polycarbonate	0.502	0.372	1.163	257,521	11,130	0.074466
	1	0.403	0.243	0.900	1,626,774	69,223	0.049167
	2	0.475	0.240	0.892	1,527,598	73,902	0.058128
	3	0.480	0.239	0.894	1,525,820	68,341	0.053949
	4	0.483	0.239	0.895	1,607,528	61,026	0.049542
	5	0.472	0.240	0.894	1,535,613	66,932	0.056275
0	6	0.485	0.240	0.900	1,505,694	61,249	0.048422
	1	0.403	0.240	0.989	1,273,595	35,422	0.032770
	2	0.407	0.240	0.989	1,328,941	28,824	0.025756
	3	0.402	0.242	0.990	1,398,680	33,130	0.028802
	4	0.481	0.242	0.890	1,230,307	37,098	0.037201
15	5	0.403	0.241	0.991	1,374,566	31,991	0.029546
	1	0.460	0.240	0.990	1,014,051	23,730	0.034838
	2	0.469	0.241	0.886	911,153	23,798	0.037223
	3	0.475	0.242	0.886	1,000,468	23,344	0.032449
	4	0.474	0.242	0.888	920,624	21,725	0.031730
30	5	0.474	0.241	0.890	906,209	23,005	0.032000
	1	0.423	0.242	0.995	854,229	18,677	0.026697
	2	0.418	0.238	0.992	881,733	19,008	0.027716
	3	0.415	0.240	0.992	827,547	21,492	0.028478
	4	0.414	0.240	0.994	843,445	18,154	0.025825
	5	0.412	0.240	0.994	918,552	20,435	0.025737
	6	0.386	0.242	0.997	940,751	18,927	0.023462
45	7	0.405	0.240	0.997	944,311	21,644	0.030883
	1	0.489	0.239	0.900	816,667	20,026	0.027444
	2	0.420	0.239	1.040	913,861	17,819	0.027683
	3	0.417	0.239	1.010	804,348	19,814	0.029485
	4	0.404	0.239	0.998	809,690	19,700	0.030198
	5	0.419	0.238	1.030	850,597	19,867	0.026291
	6	0.427	0.239	1.050	900,385	18,931	0.026200
60	7	0.411	0.239	0.994	841,459	17,029	0.031922
75	1	0.488	0.240	0.900	847,179	19,756	0.032133
	2	0.488	0.241	0.891	828,672	21,167	0.036341
	3	0.487	0.238	0.893	837,349	19,907	0.029933

	4	0.483	0.240	0.900	794,588	20,036	0.032556
	5	0.418	0.240	1.020	954,241	20,551	0.027873
	1	0.415	0.240	0.993	936,512	18,799	0.029008
	2	0.480	0.239	0.900	881,376	18,786	0.024167
	3	0.487	0.239	0.900	919,577	18,806	0.029089
	4	0.484	0.239	0.900	864,954	19,675	0.027489
	5	0.403	0.238	0.997	917,678	19,075	0.029168
90	6	0.403	0.238	0.996	891,770	19,237	0.024629

Table 8.6 - Off-axis compression test results for 10% fly ash samples

Degree	Sample #	width, in	Thickness, in	Length, in	E, psi	Failure strength, psi	Failure strain, in/in
	1	0.506	0.242	0.996	1,609,274	64,354	0.023845
	2	0.512	0.240	0.992	1,599,263	60,684	0.045983
	3	0.530	0.240	0.990	1,589,242	63,820	0.045556
	4	0.509	0.242	0.997	1,678,561	67,342	0.045469
	5	0.517	0.243	1.040	1,641,033	52,597	0.039490
0	6	0.530	0.242	0.995	1,661,834	59,871	0.040693
	1	0.526	0.240	0.991	1,268,611	42,514	0.039627
	2	0.514	0.241	0.985	1,190,021	33,859	0.039746
	3	0.530	0.241	1.000	1,223,991	33,593	0.037070
	4	0.529	0.240	0.955	1,236,346	38,453	0.035246
	5	0.506	0.242	0.987	1,226,199	31,082	0.034924
15	6	0.531	0.241	0.983	1,265,596	37,143	0.035168
	1	0.519	0.242	0.992	928,960	26,704	0.034990
	2	0.528	0.241	0.996	919,195	26,924	0.036102
	3	0.512	0.240	0.987	751,513	21,433	0.037649
	4	0.527	0.241	0.997	974,580	25,187	0.033039
	5	0.513	0.240	0.995	971,482	24,998	0.035678
30	6	0.530	0.240	0.995	897,860	27,795	0.033337
	1	0.513	0.242	0.996	721,881	21,250	0.040382
	2	0.530	0.241	0.995	745,076	22,926	0.033387
	3	0.513	0.241	0.995	801,868	20,520	0.033518
	4	0.530	0.240	0.991	726,225	23,401	0.037185
	5	0.513	0.240	0.994	746,666	22,092	0.037254
45	6	0.530	0.241	1.000	754,328	23,102	0.038050

	1	0.520	0.240	1.000	743,712	21,192	0.039580
	2	0.532	0.240	1.060	759,542	20,323	0.038698
	3	0.513	0.242	0.995	722,385	20,902	0.038302
	4	0.530	0.240	1.050	651,491	18,089	0.039238
	5	0.507	0.241	0.986	746,145	22,628	0.036765
60	6	0.535	0.241	0.978	748,864	21,743	0.035123
	1	0.524	0.243	0.993	773,026	23,199	0.035982
	2	0.505	0.243	1.075	786,633	19,184	0.032298
	3	0.530	0.242	0.997	793,511	22,576	0.033009
	4	0.512	0.240	0.988	708,114	17,263	0.032368
	5	0.510	0.240	0.988	791,058	21,574	0.037246
75	6	0.530	0.242	0.990	767,392	20,890	0.029828
	1	0.530	0.240	0.988	776,713	23,806	0.034939
	2	0.514	0.241	0.992	790,439	18,970	0.028377
	3	0.529	0.241	0.990	781,856	23,335	0.017263
	4	0.513	0.242	0.990	710,859	16,406	0.031879
	5	0.513	0.241	0.995	762,794	21,099	0.031337
90	6	0.530	0.240	1.000	764,196	20,185	0.029300

Table 8.7 - Mean and standard deviation values for the off-axis compression test results

5% fly ash loading level						
Orientation, degree	Avg E, psi	St dev	Avg Failure Strength	St dev	Avg Failure Strain	St dev
0	1,554,838	49,638	66,779	4,957	0.05258	0.00411
15	1,301,852	63,083	33,334	3,682	0.03013	0.00411
30	950,501	52,292	23,120	843	0.03365	0.00235
45	887,224	47,788	19,762	1,415	0.02697	0.00236
60	848,144	43,753	19,027	1,172	0.02846	0.00214
75	826,947	22,859	20,217	644	0.03019	0.00378
90	896,097	29,157	18,938	461	0.02735	0.00212
10% fly ash loading level						
Orientation, degree	Avg E, psi	St dev	Avg Failure strength	St dev	Avg Failure strain	St dev
0	1,629,868	36,135	61,445	5,103	0.04017	0.00846
15	1,235,127	29,289	36,107	4,105	0.03696	0.00224
30	938,416	95,226	25,507	2,264	0.03513	0.00174
45	738,835	14,025	22,554	876	0.03663	0.00272
60	728,690	39,721	20,813	1,547	0.03795	0.00170
75	782,324	11,505	21,485	1,564	0.03346	0.00271
90	771,390	9,372	22,106	1,742	0.02885	0.00612

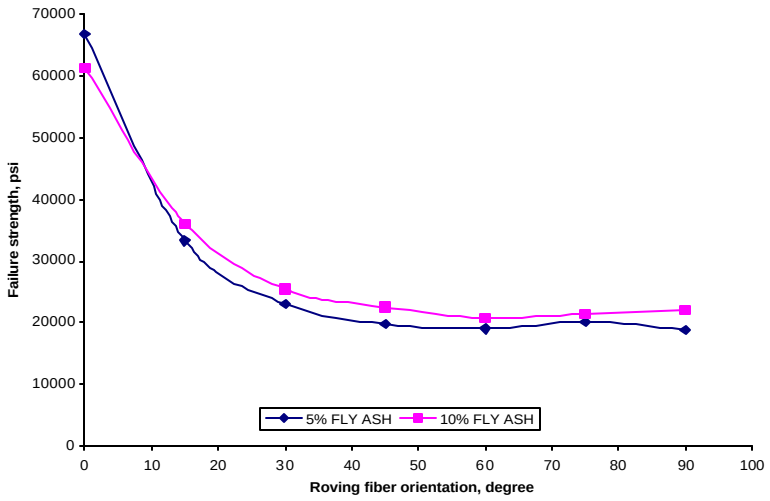

Figure 8.18 - Variation of failure strength with roving fiber orientation

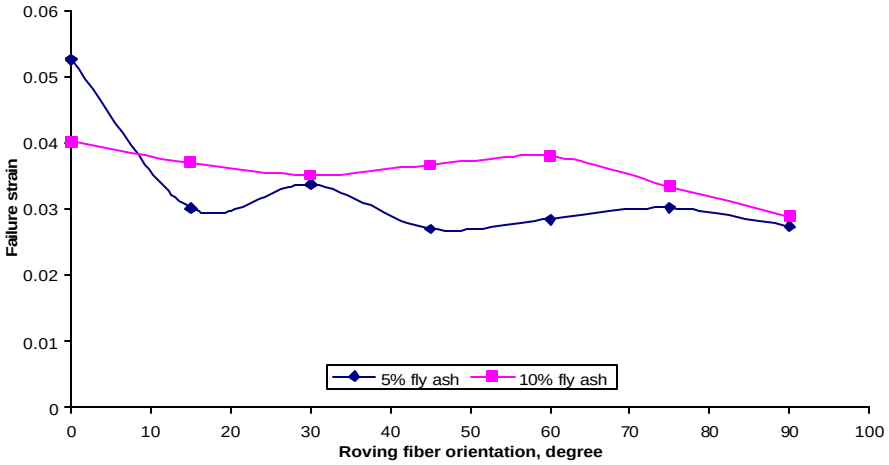

Figure 8.19 - Variation of failure strain with roving fiber orientation

8.4. Flexural bending test

In this section, four-point flexural bending tests were conducted on the flat panel following procedures outlined in ASTM D 790-97. Testing apparatus included a two-point loading nose and a support, as shown in Figure 8.20.

Figure 8.20 - Four-point flexural bending test of composite panel

The cylindrical surface of the loading nose and support avoided localized failure due to stress concentration directly under/above the nose/supports. The span between the two supports and two loading noses are 6 inches and 2 inches, respectively. The span-to-depth ratio of the samples is 25.2, which is larger than the value of 16 required by ASTM standards. This ensures that the failure occurs in the outer fibers of the specimen and is due to the pure bending moment.

The MTS testing machine shown in Figure 8.21 was used for testing. It is equipped with a precise displacement gage, which was used to measure the mid-span deflection of the sample. For calibration purposes, one A572-type steel bar of rectangular cross-section (10 in. long, 1 in. wide, and 0.5 in. thick) was tested. The flexural modulus of the steel bar was found to be about 26.3 million psi, which agrees

well with the published value of 29 million psi. With 9% error, the accuracy of the 4-point bending testing system was considered acceptable.

Test specimens (8 inch long and 1 inch wide) were cut from the original pultruded panel using the power saw. Two types of samples were prepared: lengthwise (LW) samples and crosswise (CW) samples. Seven samples were prepared for each type at the two fly ash loading levels of 5% and 10%. Twenty-eight (28) samples were prepared in total. All the specimens were loaded incrementally at the rate of 1.2 mm/min. However, the failure strength of all samples could not be determined from the experiment due to large mid-span deflection and limited measuring range of the gage. Table 8.8 lists the test results, which basically agree with the tensile test results.

Table 8.8 - Four-point bending test results of pultruded composite panel

Sample #	Fly ash %	Elastic Modulus
	%	psi
LW-FRP5%a	5	3,646,245
LW-FRP5%b	5	3,823,654
LW-FRP5%c	5	3,613,749
LW-FRP5%d	5	3,499,096
LW-FRP5%e	5	3,745,629
LW-FRP5%f	5	3,500,496
LW-FRP5%g	5	3,647,544
Mean		3,639,488
Std Deviation		119,013
LW-FRP10%a	10	3,562,602
LW-FRP10%b	10	3,746,426
LW-FRP10%c	10	3,247,904
LW-FRP10%d	10	3,571,955
LW-FRP10%e	10	3,913,335
LW-FRP10%f	10	3,571,098
LW-FRP10%g	10	3,309,447
Mean		3,560,395
Std Deviation		230,959

Sample #	Fly ash %	Elastic Modulus
	%	psi
CW-FRP5%a	5	1,732,888
CW-FRP5%b	5	1,573,149
CW-FRP5%c	5	1,516,297
CW-FRP5%d	5	1,674,976
CW-FRP5%e	5	1,611,599
CW-FRP5% f	5	1,594,967
CW-FRP5%g	5	1,657,295
Mean		1,623,024
Std Deviation		71,577
CW-FRP10%a	10	1,613,088
CW-FRP10%b	10	1,535,932
CW-FRP10%c	10	1,684,685
CW-FRP10%d	10	1,497,244
CW-FRP10%e	10	1,636,468
CW-FRP10%f	10	1,564,237
CW-FRP10%g	10	1,669,761
Mean		1,588,609
Std Deviation		69,046

Engineering properties for the 5% and the 10% fly ash panels were found to be statistically the same for both lengthwise samples and crosswise samples. When loaded along the pultrusion direction, the 5% fly ash panel yielded 3,639,488 psi elastic modulus and the 10% panel provided 3,560,395 psi. When the samples were loaded transversely,

the elastic module of the 5% fly ash samples and the 10% fly ash samples were 1,623,024 psi and 1,588,609 psi, respectively. As compared with the theoretical prediction of the flexural bending stiffness of the manufactured material (Ex = 3.462 million psi, Ey = 2.015 million psi), the experimental results in the longitudinal direction are fairly accurate, about 20% error is observed in the transverse direction.

8.5. Water absorption and UV resistance

The CCBs-filled composite materials were also characterized for their water absorption, dielectric constant, and UV resistance by Ashland Chemicals, Inc.

Water absorption: Composite materials containing 5%-fly-ash and 10%-fly-ash were evaluated for their water absorption capability. Table 8.9 lists the test results, and it was found that, after 24 hours, the composite containing 5% fly ash absorbed 0.278% water, whereas the sample with 10% fly ash absorbed 0.2% of water. Adding CCBs in the composite reduces water absorption.

Ultra-Violet radiation: Effects of ultraviolet radiation present in sun light on the performance of the manufactured composite utility pole is of concern. Ultraviolet radiation that reaches the earth's surface comprises about 6% of the total solar radiant flux and has wavelengths between 290 nm and 400 nm. Radiation below approximately 290 nm is effectively eliminated by stratospheric ozone. The remainder of the solar radiation is composed of visible (52%) and infrared (42%) radiations. Since most polymers have bond dissociation energies on the order of 290 nm to 400 nm wavelengths in the ultraviolet region, they are greatly affected by exposure to this portion of the solar spectrum.

Table 8.9 - Water absorption test results

		Initial Weight	Weight after 24 hrs	WATER ABSORPTION
SAMPLE	TEST #	BEFORE (g)	AFTER (g)	GAIN (%)
5% fly ash FRC	1	20.6795	20.7343	0.265
	2	20.8538	20.9096	0.268
	3	20.6386	20.7010	0.302
	MEAN	20.7240	20.7816	0.278
	STD. DEV.			0.021
		DRY WEIGHT	24 HRS. WEIGHT	WATER ABSORPTION
SAMPLE	TEST #	BEFORE (g)	AFTER (g)	GAIN (%)
10% Fly ash FRC	1	21.2487	21.2954	0.220
	2	21.2251	21.2674	0.199
	3	21.0391	21.0773	0.182
	MEAN	21.1710	21.2134	0.200
	STD. DEV.			0.019
1 gram = 0.0022046 pound				

Chemical changes induced by UV exposure are the result of a complex set of processes involving the combined effect of UV and oxygen. Bond dissociation is initiated by the absorption of UV radiation, resulting in chain scission and/or cross linking; subsequent reactions with oxygen along with the UV radiation result in the formation of surface flaws on the material, which can serve as stress concentrators and initiate fracture at stress levels much lower than those for unexposed specimens. The effect of ultraviolet radiation is also compounded by the action of temperature, moisture, wind-borne abrasives, freeze-thaw and other environmental components.

The outdoor test results (real time) are influenced by fluctuations in temperature, moisture, and UV irradiance. The intensity of UV irradiance changes with the test location, the season in which the testing is carried out, and year to year fluctuations due to climate variations. Test results from different exposure sites and different time periods are therefore seldom comparable. To obtain more reliable and comparable results, accelerated laboratory UV resistance testing was conducted in this study by exposing the samples to UV radiation from a variety of UV light sources, which were screened with a special filter to remove the light wavelengths that fall outside of the solar spectral range of interest.

In this test, two samples (5% fly ash and 10% fly ash composite) were exposed for 500 hours with a xenon arc lamp in Atlas Ci65 Weather-O-meter (Figure 8.22) using CAM #47. The CAM #47 has the following cycle: 18 hours of light with 18 minutes of water spray every 2 hours; and then 6 hours of darkness. A borosilicate outer and a borosilicate inner filter were used to filter the xenon arc lamp. This filter combination yields the irradiance ranges (W/m^2) as listed in Table 8.10.

Table 8.10 - Irradiance ranges of UV resistance test

Irradiance Ranges W/m^2					
Wattage	**250-300nm**	**300-400nm**	**400-800nm**	**340nm**	**420nm**
5000	0.1	37	352	0.30	0.81

Test results showed that both samples did not show any apparent material degradation. No surface flaws were observed after exposing the material to UV for 500 hours.

CHAPTER 9: FAILURE ANALYSIS

9.1. Introduction

To perform failure analysis on the manufactured composite material, this chapter first discusses various failure criteria. Since more than thirty (30) failure criteria have been reported in the literature for laminated composites, this chapter surveys only the major existing failure criteria and develops the one that fits the laboratory test results of the manufactured CCBs-filled FRC outer-shell material.

9.2. Failure criteria

Failure criteria have been developed for homogeneous isotropic materials, and inferences from those also have been extended for laminated fiber-reinforced composites that are non-homogeneous and anisotropic. This chapter surveyed major failure criteria with the purpose of identifying the most suitable one for CCBs-filled FRC material. The survey is not complete, and it was primarily focused on those criteria that may be most applicable to laminate fiber-reinforced composite based on laboratory test result.

Lamina failure criteria: The existing lamina failure criteria can be grouped as non-interactive and interactive. Non-interactive failure criteria (maximum stress, maximum strain, etc.) do not consider the interaction effect of different stress component on lamina failure and are usually applicable to brittle isotropic materials where maximum tensile, shear, or compressive stresses alone dictate failure. For composite materials, however, a biaxial state of stress is found to influence failure and hence there is a need for failure theories which consider the interaction of stresses. The interactive failure criteria are represented by Tsai-Wu (1971), Tsai-Hill (1950), etc. They are mostly quadratic polynomial equations, and are called criteria and not theories because they do not attempt to mechanistically explain failure but rather are a fitted curve for experimental data.

In the following sections, the major non-interactive and interactive criteria are discussed. A common strength ratio 'R' is defined as follows:

R = 1, failure occurs.

R > 1, failure does not occur.

R < 1, failure has already occurred.

This ratio is applicable to all common failure criteria and can be used in many ways to aid design. The strength ratio concept is similar to safety factor.

The non-interactive type failure criteria are typically represented by maximum stress criterion (Barbero, 1999), maximum strain criterion (Waddoups, 1968), and Hashin criterion (1980).

Maximum stress criterion:

This criterion predicts failure of a lamina when at least one of the stresses in material coordinates (s_1, s_2, s_6, s_4, s_5) exceeds the corresponding experimental value of strength. The criterion states that failure occurs if any of the following is true:

$R_1 = F_{1t}/s_1$ if $s_1 > 0$

$R_1 = -F_{1c}/s_1$ if $s_1 < 0$

$R_2 = F_{2t}/s_2$ if $s_2 > 0$

$R_2 = -F_{2c}/s_2$ if $s_2 < 0$

$R_4 = F_4/\ abs(s_4)$

$R_5 = F_5/\ abs(s_5)$

$R_6 = F_6/\ abs(s_6)$ Equation 4 - (9.1)

If any of the above ratios equals or exceeds unity, failure is said to have occurred in that lamina. There are five independent modes of failure, one associated with each stress s_1, s_2, s_4, s_5, and s_6. Figure 9.1 illustrates this criterion in $s_2 - s_6$ stress space.

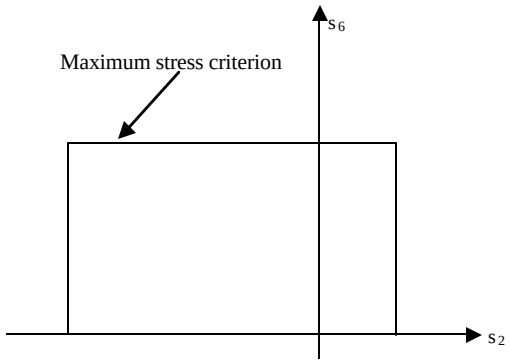

Figure 9.1 - The maximum stress criterion in s_2 - s_6 stress space

However, there are some limitations in this criterion. Tsai (1968) studied the failure of a unidirectional reinforced composite subjected to uniaxial load at an angle 0^o to the fibers. He found that the theoretical strength variation did not agree well with the experimental strength variation. For the analysis of a E-Glass Epoxy composite subjected to uniaxial loading at an angle 0^o, the theoretical strength variation did not adequately represent the experimental strength variation. In addition, the experimental data from biaxial strength tests (Hull, 1996) showed that there were interactive effects, which produced failure when two or more stress components are close to their limits. Hence, there is a need for a biaxial strength criterion.

Maximum strain criterion:

This criterion (Waddoups, 1968) is widely accepted in the industry today. With similar strength ratio as defined in previous the criterion, it can be described as

$R_1 = e_{1t}/e_1$ if $e_1 > 0$

$R_1 = -e_{1c}/e_1$ if $e_1 > 0$

$R_2 = e_{2t}/e_2$ if $e_2 > 0$

$R_2 = -e_{2c}/e_2$ if $e_2 > 0$

$R_4 = ?_{4u}/\ abs(e_4)$

$R_5 = ?_{5u}/\ abs(e_5)$

$R_6 = ?_{6u}/\ abs(e_6)$ Equation (9.2)

where e_{1t}, e_{1c}, e_{1t}, e_{1c}, $?_{4u}$, $?_{5u}$, and $?_{6u}$ are failure strains. As in the previous section, if any of the above ratios equals or exceeds unity, failure is said to have

occurred in that lamina. To illustrate the difference between maximum stress and maximum strain criteria, the maximum stress criterion is represented in the $e_1 - e_2$ diagram assuming the material behavior is linear up to failure (Figure 9.2).

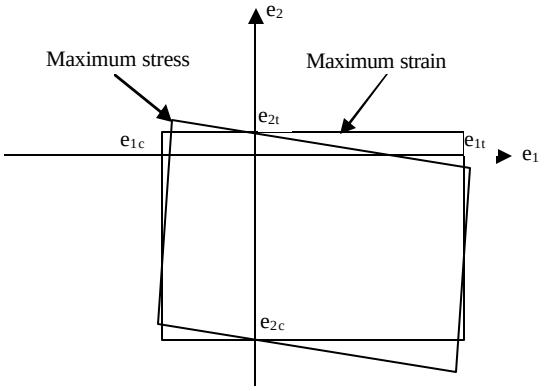

Figure 9.2 – Failure envelopes in strain space e_1-e_2

Hashin Criterion:

Hashin (1980) also modeled the various failure modes of a composite separately. A general failure criterion should be piecewise smooth, each piece modeling a distinct failure mode. In plane stress:

Fiber failure modes:

$$\text{Tensile failure: } \left(\frac{\sigma_1}{X_t}\right)^2 + \left(\frac{\sigma_{12}}{S}\right)^2 = 1$$

$$\text{Compressive failure: } \left(\frac{\sigma_1}{X_c}\right)^2 = 1 \qquad \text{Equation (9.3)}$$

Matrix failure modes:

$$\text{Tensile failure: } \left(\frac{\sigma_2}{Y_t}\right)^2 + \left(\frac{\sigma_{12}}{S}\right)^2 = 1$$

$$\text{Compressive failure: } \left(\frac{\sigma_2}{2X_{23}}\right)^2 + \left[\left(\frac{Y_c}{2X_{23}}\right)^2 - 1\right]\frac{\sigma_2}{Y_c} + \left(\frac{\sigma_{12}}{S}\right)^2 = 1 \qquad \text{Equation (9.4)}$$

where, 1 is the fiber direction, 2 and 3 are the transverse directions. X_{23} is the transverse shear strength, and S is the shear strength.

The non-interactive failure criteria separate the failure modes into fiber modes, represented by the fiber-direction strengths, and matrix modes, represented by the transverse strengths. However, neither of these criteria considers the interaction among stress components. That is, they look at failure based on one stress (or strain) at a time, ignoring the interaction between two stress components. This approach is not conservative when two stress (or strain) components are close to their ultimate values and both stresses compound to cause the same type of failure (e.g., matrix cracking).

The interactive type failure criteria developed for orthotropic plies of unidirectional composites were introduced by various theoreticians over past twenty 20 years. Goldenblat and Kopnov (1965) proposed a very general failure criterion in terms of stress components:

$$[F_i \sigma_i]^a + [F_{ij} \sigma_i \sigma_j]^b + [F_{ijk} \sigma_i \sigma_j \sigma_k]^g + \ldots = 1 \qquad \text{Equation (9.5)}$$

This type of failure criterion was derived based on curve fitting considerations. There is no theoretical or physical basis for such criterion. The criteria that fall into this category include Tsai-Hill criterion (1950), Tsai-Wu criterion (1971), etc.

Tsai-Hill criterion: This criterion is similar to the von Misses criterion for plasticity of metals adopted for orthotropic materials (Tsai, 1965). The following equation was proposed to fit the experimental data

$$\left(\frac{\sigma_1^f}{F_1}\right)^2 - \frac{\sigma_1^f \sigma_2^f}{F_1^2} + \left(\frac{\sigma_2^f}{F_2}\right)^2 + \left(\frac{\sigma_6^f}{F_6}\right)^2 + \left(\frac{\sigma_4^f}{F_4}\right)^2 + \left(\frac{\sigma_5^f}{F_5}\right)^2 = 1 \qquad \text{Equation (9.6)}$$

where the superscript *f* is used to indicate any state of stress (σ_1^f, σ_2^f, σ_4^f, σ_5^f,, σ_6^f) at failure.

All the failure states of stress obtained by combinations of those five stress components generate a closed surface (the failure envelope) that separates the no-failure region from the failure region. When only two stress components are different from zero, the failure envelope generated by (9.6) is an ellipse. In order to have a useful failure criteria, Equation (9.6) was rewritten using the strength ratio *R*. Replacing the stress components on the failure envelope σ_i^f by $R\sigma_i$, the condition for failure (9.6) becomes

$$\left[\left(\frac{\sigma_1}{F_1}\right)^2 - \frac{\sigma_1 \sigma_2}{F_1^2} + \left(\frac{\sigma_2}{F_2}\right)^2 + \left(\frac{\sigma_6}{F_6}\right)^2 + \left(\frac{\sigma_4}{F_4}\right)^2 + \left(\frac{\sigma_5}{F_5}\right)^2\right] R^2 = 1$$

or

$$R = 1 \Big/ \sqrt{\left(\frac{\sigma_1}{F_1}\right)^2 - \frac{\sigma_1 \sigma_2}{F_1^2} + \left(\frac{\sigma_2}{F_2}\right)^2 + \left(\frac{\sigma_6}{F_6}\right)^2 + \left(\frac{\sigma_4}{F_4}\right)^2 + \left(\frac{\sigma_5}{F_5}\right)^2} \qquad \text{Equation (9.7)}$$

where σ_i are the components of stress computed for an applied reference load. As explained earlier, the value of *R* can be interpreted as a safety factor if $R > 1$. Otherwise, $R < 1$ indicates failure, and R can be used to compute the failure load.

A disadvantage of the Tsai-Hill criterion is that the mode of failure is no longer identified as it was in the case of maximum stress or strain criteria. Furthermore, Tsai-Hill criterion does not take into account different behavior in tension and compression, which is very important for CCBs-based polymer matrix composite utility pole.

Tsai-Wu criterion:

The Tsai-Wu criterion was developed to overcome some of the limitations of the Tsai-Hill criterion. This criterion uses a complete quadratic expression to draw a failure envelope that attempts to fit the experimental data (Tsai, Wu, 1971). The criterion is written as

$$\begin{aligned} &f_1 \sigma_1^f + f_2 \sigma_2^f + f_{11} (\sigma_1^f)^2 + f_{22} (\sigma_2^f)^2 \\ &+ 2 f_{12} (\sigma_1^f \sigma_2^f)^2 + f_{66} (\sigma_6^f)^2 + f_{44} (\sigma_4^f)^2 + f_{55} (\sigma_5^f)^2 = 1 \end{aligned} \qquad \text{Equation (9.10)}$$

where $f_1 = \frac{1}{F_{1t}} - \frac{1}{F_{1c}}$

$f_2 = \frac{1}{F_{2t}} - \frac{1}{F_{2c}}$

$f_{11} = \frac{1}{F_{1t}F_{1c}}$

$f_{22} = \frac{1}{F_{2t}F_{2c}}$

$f_{66} = \frac{1}{F_6F_6}$

$f_{55} = \frac{1}{F_5F_5}$

$f_{44} = \frac{1}{F_4F_4}$

In (9.10), s_i^f are the components of stress at any point on the failure envelope. That is, any such state of stress corresponds to failure of the material. In the definition of the coefficients f_i and f_{ij}, the compressive strength values are defined as positive values, and the Tsai-Wu criterion accounts for different behavior in tension and compression. The interaction between the two normal stresses is accounted for with an independent coefficient f_{12} that must be measured independently of the remaining strength properties. Since a biaxial test is needed for measurement of the interaction coefficient, and experimental data are not easily measured, an approximation of the interaction coefficient can be obtained by

$$f_{12} = -\frac{1}{2F_{1t}F_{1t}} \qquad \text{Equation (9.11)}$$

Once an equation that fits the experimental data has been defined, the Tsai-Wu criterion is rewritten in a way that is convenient for design. The concept adopted in this failure criterion is considered practical by the author, and was implemented with the available laboratory test data.

Laminate failure analysis:

The approaches to predict the laminate failure and strength can be categorized into two types: the ply by ply approach and the total laminate approach. The laminate in the first approach is assumed to be consisted of various bonded layers, which are considered to be homogeneous and orthotropic. With given loading condition and boundary condition on the laminate, classical plate theory is used to calculate the stresses and strains in each layer (lamina). These stresses and strains are transformed to the layer principal axes before the failure criterion is applied to each lamina. In the second approach, the classical plate theory is not needed because the failure criterion is applied directly to the entire laminate, which is assumed homogeneous, but anisotropic. This approach requires the strength characterization of laminate under consideration, whereas in the first

approach the strength characterization is carried out on a layer and then the strength of any laminate under any stress state is predicted.

Ply-by-ply approach: This methodology is the most classical approach. It consists of using one of the layer criteria described in the previous sections to predict the first ply failure (FPF) load, at which the first layer failure occurs. Since the transverse strength F_{2t} of the laminate is usually much lower than the tensile strength F_{1t}, the FPF load is usually associated with matrix cracking. Then each layer with matrix cracking is degraded or discounted and the load is increased until a fiber failure occurs, called fiber failure (FF) load.

In this approach, the first ply (or layer) to fail while the load is increased can be found by using any of the failure criteria described in previous sections. The computation of stresses before the first ply fails can be done by the classical plate theory procedure. Since the stress distribution is piecewise linear throughout the thickness of a laminate, the maximum value of a component of stress is found either on the top or bottom of a layer. Instead of looking for maximum value (top or bottom) for each particular load case, both the top and bottom values are checked for every layer. To check if a laminate will fail under a prescribed set of loads, the stresses for that prescribed load are computed through classical plate theory. Once the stresses are known at top and bottom surfaces of each ply, a failure criterion can be used at those points to compute the strength ratio. If the strength values used in the failure criteria are ultimate values, the resulting strength ratio is the safety factor. Then the minimum value of strength ratio of all those computed at top and bottom of all layers represents the safety factor of the laminate. If it is less than one, or less than the desired safety factor, redesign must be done. Also, if the strength ratio is too large, it indicates that the laminate is over designed and savings can be realized by redesign.

The procedure just outlined can be used to detect the load at which the first layer (or ply) will fail. In this case, a set of reference loads is specified, which could be the actual load or a unit load. Then an analysis is conducted to determine the strength ratio. The FPF load, which is the set of loads that causes the first ply (or layer) to fail, is obtained by multiplying the reference set of loads by the strength ratio.

For most polymer based composite materials, FPF usually involves some type of matrix degradation, like matrix cracks or micro-cracks. The stiffness of a layer is reduced significantly by matrix cracks, mainly in the transverse direction. But matrix cracks do not affect much the longitudinal stiffness E_1 because the fibers remain intact. Since the extent of stiffness reduction in a degraded layer is unknown and difficult to measure, an empirical degradation factor f_d is used to reduce the stiffness of a degraded layer except the longitudinal stiffness. The stiffness of a degraded layer then is

$$E_1 = E_1^0$$
$$E_2 = f_d\, E_2^0$$
$$G_{12} = f_d\, G_{12}^0$$
$$G_{23} = f_d\, G_{23}^0$$
$$?_{12} = f_d\, ?_{12}^0 \qquad \text{Equation (9.12)}$$

where the superscript ()° indicates the original, intact, or un-degraded property, and f_d is the degradation factor.

When a layer fails, there is a stress redistribution under applied load. Most of the stress carried by a failing layer must be transferred to the remaining intact layers. To find the load at which the next layer fails, the properties of the first failed layer can be degraded according to (9.12); then the laminate can be reanalyzed to find all the stresses and strength ratios (Figure 9.3). Following the above procedure, the minimum of all the strength ratios computed at the top and bottom of all layers gives the second-ply failure load. This incremental analysis is repeated until all the layers are degraded. Then a final computation with all the layers degraded according to (9.12) provides the load at which a layer fails in the fiber direction, which is called FF load.

$$\overline{Q}_{11} = Q_{11}\cos^4? + Q_{22}\sin^4? + 2(Q_{12} + 2Q_{66})\sin^2? \cos^2?$$

$$\overline{Q}_{12} = (Q_{11} + Q_{22} - 4Q_{66})\cos^2? \sin^2? + Q_{12}(\sin^4? + \cos^4?)$$

$$\overline{Q}_{22} = Q_{11}\sin^4? + Q_{22}\cos^4? + 2(Q_{12} + 2Q_{66})\sin^2? \cos^2?$$

$$\overline{Q}_{16} = (Q_{11} - Q_{12} - 2Q_{66})\cos^3? \sin? + (Q_{22} - Q_{12} - 2Q_{66})\cos? \sin^3?$$

$$\overline{Q}_{26} = (Q_{11} - Q_{12} - 2Q_{66})\cos? \sin^3? + (Q_{22} - Q_{12} - 2Q_{66})\cos^3? \sin?$$

$$\overline{Q}_{66} = (Q_{11} + Q_{22} - 2Q_{12} - 2Q_{66})\cos?^2\sin^2? + Q_{66}(\cos^4? + \sin^4?)$$

This approach has been well-accepted by academia and industry. However, since this approach requires the engineering properties of the single lamina as the input, its applicability is somehow limited by or contingent upon laboratory test of lamina, which in most cases is hard to implement. Most FRCs are manufactured in the forms of a laminate (combination of lamina). In this study, the CCBs-filled FRC material was pultruded as a laminate, and consequently laboratory testing of roving layer and continuous strand mat layer is not possible. Therefore, even though the ply-by-ply failure analysis is sound theoretically, an alternate approach, the total laminate approach, is pursued for failure analysis of the CCBs-filled FRC materials.

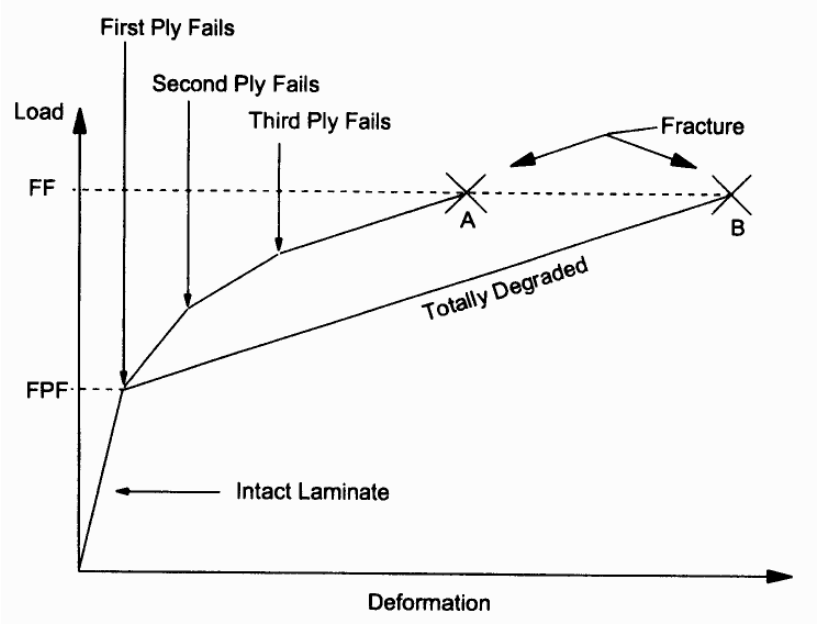

Figure 9.3 - FPF and FF load in ply-by-ply failure analysis (Barbero, 1999)

Total-laminate-approach: As discussed previously, there are two major events during loading of a laminate that can be used as indication of strength: matrix cracking and fiber failure (FF), with the latter always viewed as the collapse load of the laminate. Matrix cracking usually occurs at a lower load level, and it does not lead to collapse if the laminate is properly designed. If the transverse deformation of each layer is constrained by another layer having fibers perpendicular to the first one, the reduction in strength in one layer due to matrix micro-cracking is compensated by a load transfer into the fibers of the perpendicular layer. This hypothesis is considered reasonable for CCBs-filled FRC material, which was manufactured using pultrusion process. As discussed in earlier chapters, the CCBs-filled FRC material consists of multiple roving layers and CSM layers, which overlay one another alternatively. These layers are compacted and perfectly bonded with each other by the cured matrix (resin) while they are pulled through the heating die. The reinforcement in the CSM layer is distributed randomly, and provides lateral confinement to the roving layer. Based on these considerations, the CCBs-filled FRC laminate can be analyzed together, and the total-laminate-approach provides an alternative to the methodology for analyzing failure criterion for such material, as presented in following section.

Suggested failure criterion: Based on the discussions in earlier sections, the total-laminate approach is proposed in this study to develop a quadratic failure criterion for CCBs-filled FRC material, the main concept of which basically stems from Tsai theory (1980).

The total-laminate approach assumes that the following hold:

- All laminas have a complementary layer, which has perpendicular fiber that provide confinement. The laminate does not need to be balanced, but matrix micro-cracking in any layer should be constrained by perpendicular fibers.

- Layers with various fiber orientations are interspersed as much as possible to avoid clusters of layers with the same orientation where a matrix crack can grow.
- The strains in the fiber are those of the layer *(E_1, E_2)*. This assumption is satisfied in the fiber direction, but it is only approximate in the transverse direction.

With above assumptions, the pultruded laminate of the CCBs-filled FRC material can be treated as a whole layer. The quadratic criterion is chosen in this study because it is simple, versatile and analytic. Established rules on transformation, invariance and symmetry as discussed in Chapter 6 and 7 are applicable. It includes interaction among the stress or strain components analogous to the Von- Mises criterion for isotropic materials.

Failure criteria are very important in the design and sizing of composite laminates. They should provide a convenient framework or model for mathematical operations. The framework should remain the same for different definitions of failures, such as the ultimate strength, the proportional limit, yielding, endurance limit, or a working stress based on design or reliability considerations. In this study, the criteria are not intended to explain the mechanisms of failure of the CCBs-filled FRC material.

The generalized quadratic interaction failure criterion can be written as

$$f_{ij}s_i s_j + f_i s_i = 1 \qquad \text{Equation (9.13)}$$

Above equation can be expanded for the case of two-dimensional state of stress, or i, j = 1, 2, 6.

$$f_{11}(s_1)^2 + f_{22}(s_2)^2 + f_{66}(s_6)^2 + 2f_{12}s_1s_2 + 2f_{16}s_1s_6 + \\ + 2f_{26}s_2s_6 + f_1s_1 + f_2s_2 + f_6s_6 = 1 \qquad \text{Equation (9.14)}$$

Since the CCBs-filled composite laminate is orthotropic, the strength should be unaffected by the direction or sign of the shear stress component. If shear stress sign is reversed, the strength should remain the same. Sign reversal for the normal stress components, say from tensile to compressive, is expected to have a significant effect on the strength of the composite. Thus, all terms in Equation (9.14) that contain linear or first-degree shear stress should be deleted from the equation. There are three such terms:

$$f_{16}s_1s_6,\ f_{26}s_2s_6, \text{ and } f_6s_6 \qquad \text{Equation (9.15)}$$

Since the stress components are in general not zero, the only way to ensure that the terms above vanish is for;

$$f_{16} = f_{26} = f_6 = 0 \qquad \text{Equation (9.16)}$$

With the removal of the three terms, Equation (9.14) can be simplified as

$$f_{11}(s_1)^2 + f_{22}(s_2)^2 + f_{66}(s_6)^2 + 2f_{12}s_1s_2 + f_1s_1 + f_2s_2 = 1 \qquad \text{Equation (9.17)}$$

There are four quadratic strength parameters analogous to the four independent components of modulus. There are two linear strength parameters as a result of the difference in tensile and compressive strengths. Of the six material constants or strength parameters, five can be determined by performing simple tests.

(1). Longitudinal tensile and compressive tests

Let s_{1t} = longitudinal tensile strength

s_{1c} = longitudinal compressive strength

These strengths are measured by uniaxial tests. Substituting the measured strength into Equation (9.17),

If $s_1 = s_{1t}$,

$$f_{11}(s_{1t})^2 + f_1 s_{1t} = 1 \qquad \text{Equation (9.18)}$$

If $s_1 = -s_{1c}$,

$$f_{11}(s_{1t})^2 - f_1 s_{1t} = 1 \qquad \text{Equation (9.19)}$$

Solving the two equations for two unknowns, we have

$$f_{11} = \frac{1}{s_{1t} s_{1c}} \qquad \text{Equation (9.20)}$$

$$f_1 = \frac{1}{s_{1t}} - \frac{1}{s_{1c}} \qquad \text{Equation (9.21)}$$

(2). Transverse tensile and compressive tests

Let s_{2t} = transverse tensile strength

s_{1c} = transverse compressive strength

Following same approach as for the longitudinal tests and by reason of symmetry, we have,

If $s_2 = s_{2t}$,

$$f_{22}(s_{2t})^2 + f_2 s_{2t} = 1 \qquad \text{Equation (9.22)}$$

If $s_2 = -s_{2c}$,

$$f_{22}(s_{2t})^2 - f_2 s_{2t} = 1 \qquad \text{Equation (9.23)}$$

Solving the two equations for two unknowns, we have

$$f_{22} = \frac{1}{s_{2t} s_{2c}} \qquad \text{Equation (9.24)}$$

$$f_2 = \frac{1}{s_{2t}} - \frac{1}{s_{2c}} \qquad \text{Equation (9.25)}$$

(3). Longitudinal shear test

Let t_{12} = longitudinal shear strength

Substituting this value into she shear stress in Equation 9.17, we have

$$f_6 = \frac{1}{t_{12}^2} \qquad \text{Equation (9.26)}$$

The one remaining term f_{13} is related to the interaction between the two normal stress components. The only way that this coefficient can be measured is for both normal stress components to be nonzero; this requires a combined stress or biaxial test. This experimental task unfortunately is not as easy to perform as the simple uniaxial or shear test.

Although the exact value for the interaction term is indeterminate at this time, there are upper and lower bounds imposed on this value based on a geometric consideration. Since the failure criterion represents a closed curve in the plane of the

normal stress components (the curve has to be closed in order to avoid infinite strength), the discriminant below has to satisfy the following condition,

$$f_{11}f_{22} - f_{12}^{\ 2} > 0 \qquad \text{Equation (9.27)}$$

For convenience, a dimensionless interaction term is introduced here,

$$f_{12}^{\ *} = \frac{f_{12}}{\sqrt{f_{11}f_{22}}} \qquad \text{Equation (9.28)}$$

$$f_1^{\ *} = \frac{f_1}{\sqrt{f_{11}}} = \frac{s_{1c} - s_{1t}}{\sqrt{s_{1c}s_{1t}}} \qquad \text{Equation (9.29)}$$

$$f_2^{\ *} = \frac{f_2}{\sqrt{f_{22}}} = \frac{s_{2c} - s_{2t}}{\sqrt{s_{2c}s_{2t}}} \qquad \text{Equation (9.30)}$$

Also, variable replacements are defined below,

$$\begin{aligned} x &= \sqrt{f_{11}}s_1 \\ y &= \sqrt{f_{22}}s_2 \\ z &= \sqrt{f_{66}}s_6 \end{aligned} \qquad \text{Equation (9.31)}$$

By replacing the above dimensionless parameters and the new variables, the Equation (9.17) can be rearranged as

$$x^2 + 2f_{12}^{\ *}xy + y^2 + z^2 + f_1^{\ *}x + f_2^{\ *}y = 1 \qquad \text{Equation (9.32)}$$

The Equation (9.32) represents a family of ellipses. In the equation, the parameter $f_{12}^{\ *}$ will govern the slenderness and the inclination of the major axis. In place of the biaxial stress test to determine the sixth strength parameter, it can be assumed that the orthotropic failure criterion in Equation (9.17) is a generalization of the Von Mises criterion. In this case, $f_{12}^{\ *}$ = -0.5.

The above discussion lays a theoretical basis for developing failure criterion for CCBs-filled FRC material using the laboratory test data. As mentioned in Chapter 8, off-axis tensile test and off-axis test were conducted on the pultruded FRC material. Even though in-plane direct shear test was not performed, the material shear strength can be derived from off-axis tensile and compression tests without losing accuracy.

Based on laboratory tests, the material strengths for 10% fly ash sample under various loading condition are summarized below in Table 9.1.

Table 9.1 - Measured strength results for CCBs-filled FRC laminate

longitudinal tensile s_{1t}, psi	49,211
longitudinal compressive s_{1c}, psi	61,445
transverse tensile s_{2t}, psi	8,397
transverse compressive s_{2c}, psi	22,106
Sxx when off-axis angle is 15 degree	22,872
longitudinal shear t_{12}, psi	5,718

From Equation (9.20), (9.21), (9.24), (9.25), and (9.26), we can calculate the following

$$f_{11} = \frac{1}{s_{1t} s_{1c}} = 3.30713\text{E-}10 \text{ psi}^{-2}$$

$$f_1 = \frac{1}{s_{1t}} - \frac{1}{s_{1c}} = 4.04594\text{E-}06 \text{ psi}^{-2}$$

$$f_{22} = \frac{1}{s_{2t} s_{2c}} = 5.38723\text{E-}09 \text{ psi}^{-2}$$

$$f_2 = \frac{1}{s_{2t}} - \frac{1}{s_{2c}} = 7.38536\text{E-}05 \text{ psi}^{-1}$$

$$f_6 = \frac{1}{t_{12}^2} = 3.05852\text{E-}08 \text{ psi}^{-2}$$

Substituting above parameters into Equation (9.17), we have

$$\frac{(s_1)^2}{3{,}023{,}769{,}895} + \frac{(s_2)^2}{185{,}624{,}082} + \frac{(s_6)^2}{32{,}695{,}524} - \frac{2 s_1 s_2}{1{,}498{,}378{,}471} + \frac{s_1}{247{,}161} + \frac{s_2}{13{,}540} = 1 \qquad \text{Equation (9.33)}$$

Equation (9.33) can serve as the failure criterion for the CCBs-filled FRC material, which was derived using quadratic equations and laboratory test results.

9.3. Summary

In this chapter, efforts were made to review existing failure criteria. After comparing the advantages and disadvantages of the selected criteria, this chapter evaluated the two laminate analysis approaches. Based on the available laboratory test data and characteristics of the CCBs-filled FRC material, this chapter has proposed the total-laminate-approach for developing an appropriate material failure criterion. A quadratic interactive failure criterion was developed based on material characteristics and laboratory test results of CCBs-filled FRC outer shell material.

CHAPTER 10: PERFORMANCE TESTING OF THE MODEL POLES

10.1. Introduction

One full size model composite pole was tested in cantilever mode to evaluate its engineering performance when subjected to flexural loading. In addition, to determine the equivalent compressive elastic modulus, a one-foot section of the model pole was tested in a MTS facility in the uniaxial compression mode.

10.2. Cantilever bending test of the model composite pole

As discussed in the dimensional analysis (section 3.5) of the composite utility pole, the smaller model utility pole was manufactured to simulate engineering behavior of a full size (35 ft long) composite pole. To evaluate the engineering performance of the full size class-4 composite pole indirectly, the manufactured smaller model pole was tested in the cantilever mode. The testing apparatus and test results are discussed below.

Fixtures: The tested model composite pole was 20-ft long with an outer-diameter of 4.89 in. and outer-shell thickness of 0.1875 in. Such a model composite pole was tested horizontally as a cantilever in the bending mode using facilities at Trinity Marine Products in Paducah, KY. The testing apparatus included a steel frame to clamp one end of the pole, an overhead crane for loading, a load measuring device, a graduated scale for displacement measurement, and a level. The steel frame for holding the model pole was built against steel girder and floor framework of the building, as shown in Figure 10.1. The model pole was clamped rigidly over a 2-ft length at one end. The other end of the pole was lifted up gradually with the overhead crane in displacement-controlled mode, as shown in Figure 10.2. Load and top deflection of the pole were measured with a load-measuring device and a graduated scale installed vertically along the end of the pole, respectively. Load and top deflection of the model pole were recorded in 3-in top deflection increments. Figure 10.3 shows the deflected composite model pole prior to the failure. Figure 10.4 shows the cracked section of the model composite pole after the pole failed.

Figure 10.1 - The steel frame used to clamp the model pole

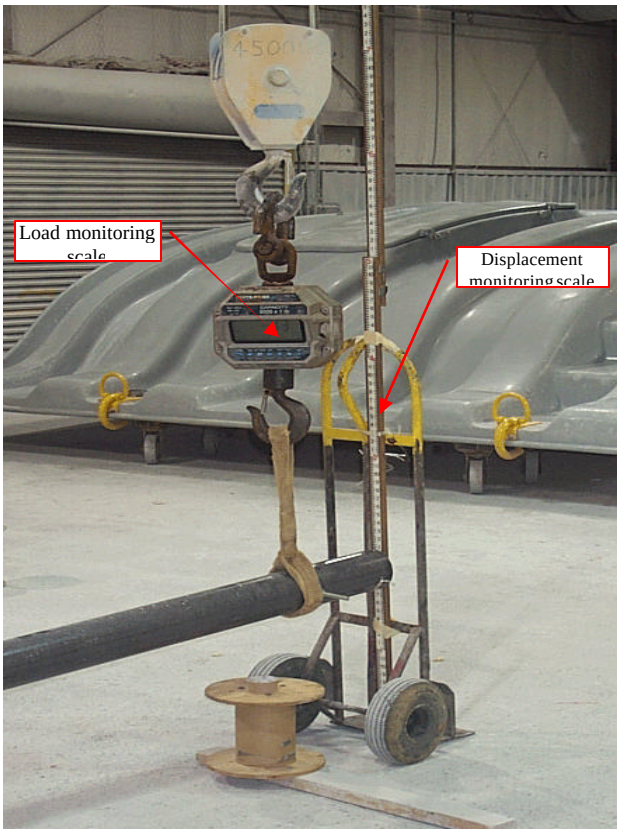

Figure 10.2 - Loading device and deflection measuring setup

Figure 10.3 - Cantilever bending test of 20-ft long model composite utility pole

Figure 10.4 - Cantilever bending test after material failure

Test results and discussion:

The model composite pole was loaded in deflection-controlled mode and the corresponding load was recorded for every 3-inch incremental top deflection. Table 10.1 lists the test results and the average equivalent material flexural stiffness. As shown in Figure 10.5, the applied load increases almost linearly with the increase in top deflection until failure. The pole failed at final load of 520 lb and final top deflection of 59 inches. Using a mechanics of material approach (Figure 10.6), the pole's equivalent flexural bending stiffness and strength were calculated. It was found that the pole has an equivalent elastic modulus of 2.3 to 2.4 million psi (Figure 10.7) and strength of about 30,000 psi.

Table 10.1 - Test result of cantilever bending test on composite model pole

Raw deflection	**Raw load**	**Zeroed deflection**	**Adjusted load**	**Equivalent E**
in.	lb	in.	lb	psi
17.00	-75	0.00	0	
19.00	-58	2.00	17	2,373,888
21.00	-44	4.00	31	2,164,428
23.00	-25	6.00	50	2,327,342
24.63	-13	7.63	62	2,270,875
26.25	0	9.25	75	2,264,441
28.13	15	11.13	90	2,259,352
29.88	32	12.88	107	2,321,015
32.00	49	15.00	124	2,308,723
34.00	65	17.00	140	2,299,961
35.88	82	18.88	157	2,323,026
38.25	102	21.25	177	2,326,246
39.88	115	22.88	190	2,319,711
42.00	133	25.00	208	2,323,618
44.00	153	27.00	228	2,358,373
46.00	170	29.00	245	2,359,443
47.88	185	30.88	260	2,351,840
51.00	207	34.00	282	2,316,389
52.75	228	35.75	303	2,367,053
55.25	249	38.25	324	2,365,674
57.25	266	40.25	341	2,366,082
58.75	284	41.75	359	2,401,482
60.88	301	43.88	376	2,393,382
62.20	320	45.20	395	2,440,619
64.63	336	47.63	411	2,410,173
66.63	358	49.63	433	2,436,850
68.75	374	51.75	449	2,423,134
70.75	394	53.75	469	2,436,889
73.88	422	56.88	497	2,440,486
76.25	443	59.25	518	2,441,647

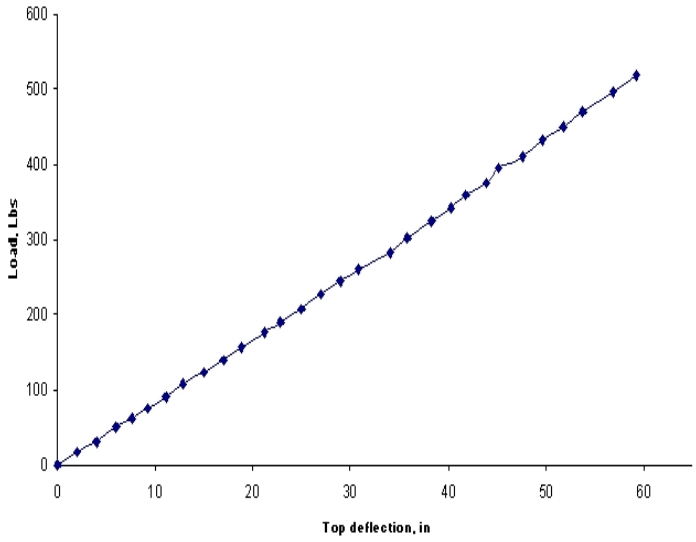

Figure 10.5 - Load vs. deflection at the top of the model pole

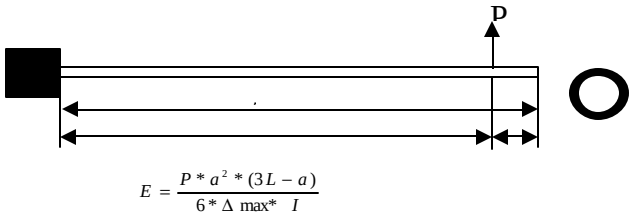

Figure 10.6 - Estimation of equivalent E of composite model pole

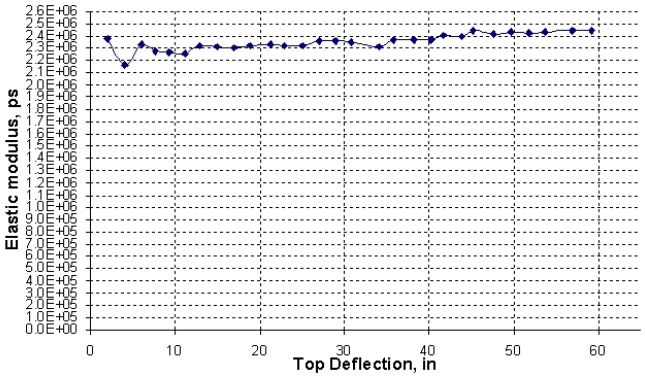

Figure 10.7 - Variation of equivalent elastic modulus with top deflection of the model pole

To verify the applicability of the classical beam theory on the manufactured model composite pole, the flexural bending curvature measured in the lab testing was compared with the theoretical bending curvature assuming an elastic modulus of 2.3 million psi for the outer-shell material, as shown in Figure 10.8. The experimental bending curvature agrees well with the theoretical curve when the pole is subjected 500 lb of transverse pulling force.

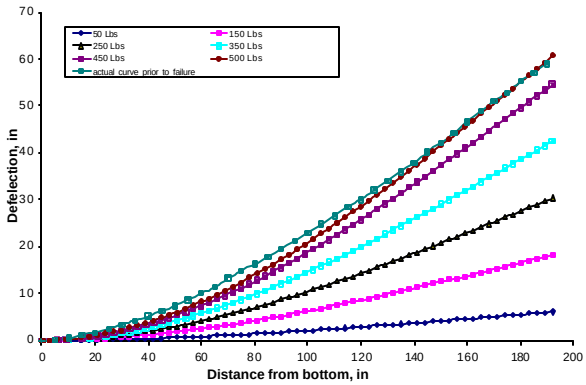

Figure 10.8 - Comparison of theoretical and experimental bending curvature

As discussed in the dimensional analysis (Section 3.5), a 20 ft long model pole with 5-inch outer diameter, 0.25-inch shell thickness, and 382.02 lb horizontal load will simulate a full size 35-ft long hollow composite pole (11.5 in. outer diameter and 0.38 in. shell thickness), which is 3% stronger and 63% lighter than the class-4 wooden pole. Therefore, the performance of the model pole when the applied load is 382 lb will simulate that of the full size pole or wooden pole. The laboratory test result reveals that the model pole deflected 44 inch when the applied transverse load was 380 lb. This result is close to the maximum allowable deflection (42.2) of a class-4 wooden pole. Therefore, even with the average equivalent flexural modulus of 2.3 million psi, the model composite pole or the full size composite pole will be comparable to a class-4 wooden pole. This conclusion may also be interpreted as though the composite pole actually failed at a 36% higher load level than required by ANSI requirement.

Even though test results show that the model composite pole has comparable flexural stiffness as wooden pole, the author believes that the actual flexural stiffness of the composite pole is higher because the steel frame utilized in the test was not rigid enough, and some displacements of the frame were observed in the experiment. Thus the authors believe that the test data are conservative and underestimate the material stiffness and strength. In addition, it was found that the manufactured model pole has several grooves in the longitudinal direction on its inside surface, which might also initiate premature failure of the composite structure.

10.3. Uniaxial compression test on 12-inch long model pole

Uniaxial compressive strength for the outer-shell material of the model pole was determined on a one-ft long section of the model composite pole. The ASTM aluminum standard sample was used to calibrate the test system. Figure 10.9 shows the stress-strain curve for the tested sample. It was found that the outer-shell material had an elastic modulus of 2.94 million psi, which is about 28% higher than the equivalent flexural stiffness obtained from the full size cantilever bending test. Even though the flexural modulus is in general lower than the compressive elastic modulus, this test result still serves as a proof that the full-size flexural bending test underestimated the actual material stiffness.

In the uniaxial compressive test of the one-ft long model pole, the sample could not be failed due to limited measuring range of the load cell of the MTS. However, at the highest load the sample started to crack with noticeable noise. Thus it was estimated that the composite model pole has about 36 ksi uniaxial compressive strength. 10.4. Field demonstration of model utility pole

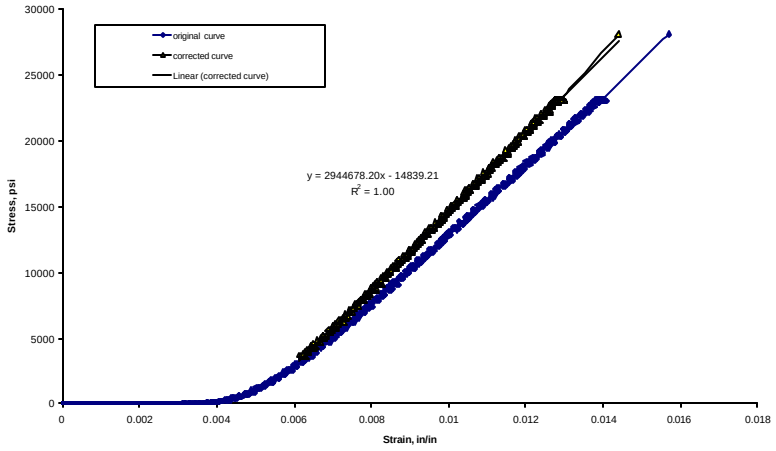

Figure 10.9 - Stress-strain curve for 12-inch long model pole in uniaxial compression

In this study, a resin-rich veil layer was added to the outer side of the manufactured composite shell material to improve the product's resistance to ultraviolet (UV) degradation. In addition, UV inhibitors were added to the resin. To test the effectiveness of the resin-rich veil layer in resisting UV degradation, field testing was conducted by installing two sample poles in Fall 2002 at the Illinois Coal Development Park for observations and weathering, as shown in Figure 10.9. After three and half years exposure to direct solar light, environment moisture, natural temperature, visual observation of the demonstrated model poles do not reveal any material degradation due to UV exposure and moisture. The same poles in Spring 2006 are shown in Figure 10.10.

Figure 10.9 - Model composite poles installed outdoor at Illinois Coal Development Park (Fall 2002**)**

Figure 10.10 : Poles on March 10, 2006 (after weathering fro 42 months)

CHAPTER 11: INDUSTRIAL COOPERATION AND ECONOMIC EVALUATION

11.1 Introduction

This project was a cooperative effort between the University, industry and government. Industrial cooperation was provided by Ashland Chemicals, Inc (polymer expertise), Columbus, OH and Trinity Industries (pole manufacturer and marketer), Paducah, KY. All commercialization activities were led by industrial cooperators. Major customers such as Ameren CIPS, Kentucky Utilities, Springfield City Light and Power, Detroit Edison, and Cinergy were contacted during the study.

11.2 Economic Evaluation

Investment, market, and fabrication cost analyses were performed by Trinity Industries, Inc. The following estimates have been provided by them.

- Capital Investment - $575,000 (2003 dollars)
- Fabrication cost of class 4 35 ft pole - $385 (2003 dollars)
- Production rate of full capacity – 800 poles/month
- Selling price per pole - $482 (2003 dollars)
- Payback period – 4.1 years
- Cost of Capital – 12%

Trinity Industries, Inc considered this project multiple times for funding until as late as Fall 2005 but did not approve capital funds for the project. There is general agreement that this is a good project and should be pursued. However, the project did not achieve high enough priority for capital funding.

CHAPTER 12: SUMMARY AND CONCLUSIONS

12.1. Summary

The goal of this study was to establish technical and economic feasibility of developing and fabricating CCBs-based composite utility poles to replace similar wooden poles. This summary presents an overview of all the work completed to date on the project.

- CCBs-filled polymer composite materials that are suitable for engineered utility poles were developed. These materials may contain about 18% high LOI, as-received FBC fly ash from SIU power plant. The strength and stiffness engineering properties and weathering properties of these filled materials are superior to polymer alone.
- Studies for determining if larger amounts of appropriately graded fly ash may be added to develop composites for utility poles fabrication were performed. The results indicate that if fly ash less than 75 microns is utilized instead of as-received fly ash, up to 30% fly ash may be added to yield composites suitable for utility pole fabrication.
- A cylindrical fiber reinforced utility pole was proposed. The proposed pole design consists of a very stiff outer shell without ultra-lightweight inner core material. Each 35 ft pole may use about 40 to 50 lb of CCBs based on 10% fly ash loading level.
- Theoretical structural analysis was conducted on the FRC utility pole to relate the various dimensional parameters of the composite pole with the structural bending stiffness of the wooden pole. With the developed formulas, preliminary composite pole designs were identified by keeping the structural bending stiffness the same for the composite pole and wooden pole.
- The FRC utility pole design was optimized using multi-objective optimization techniques. When the composite pole is hollow, the optimal design is a cylindrical composite pole with 0.175 in shell thickness and 16 inch outer diameter composite pole, which will be 55% stronger and 85% lighter than a wooden pole if its outer-shell is made of 5 layers of lamina (3 CSM layer of 0.025 in and 2 roving lamina of 0.05 in). When the pole is filled up with lightweight inner-core material, the optimal design is a cylindrical composite pole with 0.3 in shell thickness and 12.5 inch outer diameter, which will be 37% stronger and 2% lighter than a wooden pole if its outer-shell is made of 7 layers of lamina (4 CSM layer of 0.06 in and 2 roving lamina of 0.03 in)
- The commercial production process was demonstrated in a facility in Pennsylvania to produce 200-feet of about 5-inch diameter and 3/16 inch wall thickness pipe containing 5% and 10% FBC fly ash for engineering performance studies.
- Micro/macro-mechanics analyses were conducted on the pultruded FRC outer-shell material. For micro-mechanics analysis, existing models were used for the

prediction of stiffness and strengths for the roving and continuous strand mat layers. With the predicted lamina engineering properties, a macro-mechanic analysis was conducted on the whole laminate using classical plate theory, from which the laminate engineering properties were computed. The predicted laminate engineering properties are in good agreement with the experimental values.

- The pultruded FRC outer-shell materials were characterized using various ASTM test methods, including axial tension, axial compression, off-axis tension, off-axial compression, flexural bending, water absorption, dielectric constant, and UV protection. For off-axis tensile and compressive test results, a comparison was made between the experimental values and the predicted laminate stiffness values.
- Engineering performance studies were performed on the fabricated model pole, including ultra-violet degradation, water absorption, strength-deformation properties in tension, compression, and flexure, and full-size cantilever testing.
- Two 10-foot poles were installed 30-months ago at the Illinois Coal Development Park for weathering studies. To date, no effects of UV degradation have been observed by Ashland staff and the poles look like they are brand new.
- The results of these studies indicate that commercial production of CCBs-based utility poles is technically, and environmentally feasible and should be pursued to meet market needs in the Midwest.
- The commercial production of CCBs-based utility poles is economically feasible as developed by industrial partners. The estimated payback period for investment is about 4 years.

12.2. Conclusion

Based on the research and laboratory tests conducted during the project period, the following conclusions can be made:

- It is possible to engineer a CCBs-based composite pole that will meet or exceed ANSI standards.
- A cylindrical shape rather than a conical shape pole with glass fiber-reinforced thin outer-shell without inner core material is considered as a preferred design for an engineered composite pole.
- Fly ash polymers based material, appropriate for manufacturing composite utility poles, can be developed.
- Studies indicate that it is possible to develop 70 to 75 pcf glass-fiber reinforced outer shell material, which can provide a tensile strength of 30,000 to 45,000 psi with an elastic modulus ranging from 2 to 4 million psi.
- Laboratory testing of fly ash-polymer-based outer shell reveals that fly ash as filler in polymer does have a positive effect on the outer shell material stiffness and strength. The maximum percentage of as-received fly ash should not exceed 15%. However, for graded fly ash, the maximum amount of fly ash may be increased to 30%.

- Post-curing at high temperature (150 ^{o}F to 180 ^{o}F) for 8 to 24 hours has a beneficial effect on the strength and stiffness of the fly ash filled composite material.
- Test results of the inner core material show that, with a combination of chemical and mechanical systems, a mix with a reduced density of about 30 pcf and containing over 50% fly ash is achievable. Adding inner-core material however significantly increases the pole weight, resin cost, and labor cost.
- The pultrusion process appears to be the choice for fabricating the composite utility pole commercially.

12.3. Recommendations for future work

Research performed to date has significant potential to develop composite utility poles and other similar products. It should be pursued further to develop the manufacturing process with demonstration in a pilot scale facility. Also a fundamental research study on fly ash-filled polymers cross-linking and curing reactions is considered important. Emphasis should be placed on cross-linking organic phases with inorganic phases of fly ash. To market this technology, a pilot scale demonstration of the developed fabrication process and marketing of manufactured poles should be pursued.

REFERENCES

Plowman, C. and N. B. Shaw, (1984), "Use of Pulverized Fuel Ash as a Filler in Plastics," AshTech'84 - Conference Proceedings, London, England: Central Electricity Generating Board, pp.663-670.

Reddy, J. N., (1997), Mechanics of Laminated Composite Plates: Theory and Analysis, CRC Press, Boca Raton, FL.

Rebiz, K.S. (1995), "Time Temperature Properties of Polymer Concrete Using Recycled PET", Cement and Concrete Composites, Vol. 17, No. 2, p. 119-124.

Rebeiz, K. S. (1996) "Strength and Durability Properties of Polyester Concrete Using PET and Fly Ash Wastes", Advanced performance materials, Vol. 3, No. 2, p. 205-214.

Rebeiz, K. S., J. W. Rosett, A. P. Craft, (1996), "Strength Properties of Polyester Mortar Using PET and Fly Ash Wastes", J Energy Engineering. Vol. 122, No. 1 p. 10-20.

Saroja, D. M., V. Murugesan, K. Rengaraj and P. Anand, (1998), "Utilization of Fly Ash as Filler for Unsaturated Polyester Resin", Journal of Applied Polymer Science. Vol. 69, No.7, p. 1385-1391

Shakespeare composite structure ™, (2003), products specifications for Composite Transmission and Distribution Tuff-Poles®, http://www.skp-cs.com

Srivastava, V.K. and P.S. Shembekar, (1990), "Tensile and Fracture Properties of Epoxy Resin Filled with Fly Ash Particles", Vol. 25, No. 8, p. 3513-3516.

Tang, HC, T Nguyen, T-J Chuang, J Chin, J Lesko, Wu HF, (2000), "Fatigue model for fiber-reinforced polymeric composites", J Mater Civil Engr, 12(2):97 - 104.

Tsai, S. W., and E. M. Wu, (1971) "A general theory of strength for anisotropic materials", J. Composite Materials, 5, 58 – 80.

Tsai, S. W., (1965), Strength Characteristics of Composite Materials, NASA CR-224.

Tsai, S. W., and E. M. Wu, (1971), "A general theory of strength for anisotropic materials", J. Composite Materials, 5, 58—80.

Tsai, S. W. & Hahn, H. T., (1980), Introduction to Composite Materials, Technomic, Stamford, CT.

Tsai, S. W., and Hahn, H. T., (1967), Introduction to Composite Materials, Teehnomic, Lancaster, PA (1980).Nielsen, L. E., Mechanical properties of particulate-filled systems, J. Composite Materials, I. 100.119.

Turvey, G. J., (1998), "Torsion tests on pultruded GRP sheet", Compos Sci. Technol; 58:1343 - 51.

Varughese, K T and B K Chaturvedi, (1996), "Fly Ash as Fine Aggregate in Polyester Based Polymer Concrete", Cement and Concrete Composites, Vol. 18, No. 2, p. 105-108.

Wang Y, Zureick A. (1994), "Characterization of the longitudinal tensile behavior of pultruded I-shape structural members using coupon specimens", Compos Struct; 29:463 - 72.

Walrath, D.E. and D.F. Adams, (1983) "The Iosipescu Shear Test as Applied to Composite Materials", *Experimental Mechanics*, 23, 105-110

Whitney, J. M, (1967) "Elastic Moduli of Unidirectional Composites with Anisotropic Filaments." *J. Comp. Materials*, Vol. 1, pp. 188.

Waddoups, M. E., (1968) "Characterization and Design of Composite Materials Workshop", 254 - 308, S. W. Tsai, J. C. Halpin, and N. J. Pagano, eds., Technomic, Bristol, PA.

Wypych, George, (1999), Handbook of Fillers, 2nd Ed. ChemTec Publishing, pp 321.

Yamada, S. E.; and C. T. Sun, (1978), "Analysis of Laminate Strength and Its Distribution", *J. Compos. Mater.*, vol. 12, pp. 275–284.

Yu, Z, (1987), "Evaluation of Underground Supports Made of Wood and Other materials," Masters Thesis, Virginia Polytechnic Institute and State University.

Zureick A, Scott D., (1997), "Short-term behavior and design of fiber-reinforced polymeric slender members under axial compression", J Compos Constr; 1(4):140 - 9.